



PENINSULA TECHNIKON  
FACULTY OF ENGINEERING

MTech Thesis

MATHEMATICAL MODELLING OF WELDING:  
SENSITIVITY OF RESIDUAL STRESSES AND  
THERMAL DILATATION ON WELDING  
PARAMETERS

OSCAR PHILANDER

CAPE TOWN 1998



CAPE PENINSULA  
UNIVERSITY OF TECHNOLOGY  
Library and Information Services  
Dewey No ..... 671.52 PH1

CAPE PENINSULA  
UNIVERSITY OF TECHNOLOGY



9001518

CAPE PENINSULA UNIVERSITY OF TECHNOLOGY  
LIBRARY AND INFORMATION SERVICES  
BELLVILLE CAMPUS

TEL: (021) 959-6210

FAX: (021) 959-6109

Renewals may be made telephonically.

This book must be returned on/before the last date shown.

Please note that fines are levied on overdue books

18 MAR 2010

18 MAR 2010

15 OCT 2013

14 NOV 2013

26 NOV 2013

29 OCT 2015

11 NOV 2015

NOV 06 2015

**MATHEMATICAL MODELLING OF WELDING:**

**Sensitivity of residual stresses and thermal dilatations on welding parameters.**

By

**Oscar Philander**

**MDIPME, BTECH (Peninsula Technikon, South Africa)**

**Submitted towards the degree of Master of Technology  
(Mechanical Engineering)**

**Supervisors:**

**Internal: G.J. Oliver, MSc.**

**External: J. Ronda, MSc.Eng., MSc.Math., PhD., Dr.Sc**

**Peninsula Technikon  
Department of Mechanical Engineering  
Centre for *Research in Applied Technology* (CRATech)  
CAPE TOWN**

**1998**



## SUMMARY

---

In South Africa, the determination of residual stress distribution and undesirable metallurgical phase fractions that are formed in components during welding are been dealt with in a destructive or semi-destructive manner. This dissertation is an attempt at enhancing the acquisition of residual components found in welded structures. It shows how *finite element methods* can be used to obtain these results.

TIG welding is modeled as a thermo-mechano-metallurgical (TMM) problem. The mathematical and finite element models for welding described in this study is based on the work performed by Ronda and Oliver. These models has not yet fully been incorporated into any of the existing computational tools and therefor, a commercial computational software program, SYSWELD 2, was employed to perform the welding simulations. The Leblond material models are incorporated into this software program, and the model that is used for this study is described in this text.

Computational simulations were performed to study the effects that the sensitivity of welding parameters would have on the resulting shape and size of Heat Affected Zones, depth and width of penetration, temperature fields, metallurgical solid phase fractions, as well as residual stress distribution and deformation. The results of these simulations were compared to laboratory experiments.

## ACKNOWLEDGEMENTS

---

I wish to thank Dr. Jacek Ronda (Dr.Sc) for the supervision of this work and for creating the kind of environment that made this type of study possible. Dr. Ronda was responsible for the acquisition of the best computer hardware and software available at the time for the simulations of welding procedures. He also played the leading role in the construction and acquisition of state of the art welding equipment for the welding laboratory that is now situated in the Department of Mechanical Engineering at the Peninsula Technikon. This welding research laboratory enabled me to perform very useful experiments for the verification of simulated results. I cannot thank you enough for your assistance.

I would like to thank my internal supervisor, Mr. Graeme John Oliver (MSc) for all the time and effort that he invested in me and for assisting me with the experimental work.

I would like to thank Dr. Nawaaz Mahomed for starting this type of post-graduate research program at the Department of Mechanical Engineering

I would like to thank the Foundation for Research and Development (FRD) and Peninsula Technikon for their financial assistance during this study. Thanks also to the staff members at Peninsula Technikon that assisted me with my work.

I would like to acknowledge the assistance of my friends and colleagues in the Centre for Research in Applied Technology: Mornay Riddels, Philemon Simelane, Mark Ludick, and Brian Hendricks.

Finally, I would like to thank David and Maureen Philander.



# CONTENTS

---

## CHAPTER 1

<b>INTRODUCTION</b>	<b>1</b>
1.1 Influence of Residual Stress on the Quality of Welded Components	1
1.2 Occurrence of Residual Stresses	1
1.3 Remarks on Computational Welding Mechanics	2
1.4 General capabilities of software used for the welding simulations	5

## CHAPTER 2

<b>MATHEMATICAL MODEL OF WELDING</b>	<b>6</b>
2.1 Abstract	6
2.2 Lagrangian Description of Body Motion	6
2.3 Constitutive Variables	6
2.4 Balance Laws for the Thermo-Mechanical Process	7
2.5 Finite Element Approximation of a Welding Process as a coupled thermo-mechanical Problem	9
2.6 Global Finite Element Equation for the fully coupled thermo-mechanical (TM) problem	12

## CHAPTER 3

<b>MATERIAL MODEL</b>	<b>13</b>
3.1 The Welding Mega-System	13
3.2 Coupled Thermo-Metallurgical Analysis	14
3.3 Stress-Strain Constitutive Equations	15

## CHAPTER 4

<b>WELDING PROCESS USED FOR THE SIMULATIONS</b>	<b>20</b>
4.1 Introduction	20
4.2 The Gas Tungsten Arc welding (GTAW) or Tungsten Inert Gas (TIG) welding process	20
4.3 Fundamentals of the Tig welding process	21

**CHAPTER 5****THERMAL AND MECHANICAL BOUNDARY CONDITIONS 22**

5.1 Model of the arc	22
5.2 Convection from a work piece	23
5.3 Radiation from a work piece	23
5.4 Thermal contact conduction	23
5.5 Mechanical boundary conditions	24

**CHAPTER 6****SIMULATION ASSUMPTIONS AND PROCEDURES 25**

6.1 Benchmark problem for welding	25
6.2 Computational Assumptions	26

**CHAPTER 7****NUMERICAL RESULTS 27**

7.1 Introduction	27
7.2 Influence of welding parameters on HAZ and penetration	27
7.2.1 Welding Current	27
7.2.2 Welding Speed	32
7.2.3 Pre-heating of parent materials	35
7.3 The effects of welding parameters on residual stress and deformation	37
7.3.1 Thermal Stresses During Welding	37
7.3.2 Stress Distribution in a Welded Plate	37
7.3.3 Thermal distortion caused by TIG Welding	50
7.3.4 Influence of heat input have on residual stress	55
7.3.5 Influence of welding speed on residual stress	56
7.3.6 Influence of clamping on residual stress	58

**CHAPTER 8****EXPERIMENTAL VERIFICATION OF NUMERICAL RESULTS 59**

8.1 Introduction	59
8.2 Welding experiments	59
8.2.1 Experiments for welding penetration	60
8.2.2 Measurement of residual stresses	61

**CHAPTER 9**



<b>CONCLUSIONS</b>	<b>63</b>
<b>CHAPTER 10</b>	
<b>NOTES</b>	<b>65</b>
<b>APPENDICES</b>	
<b>APPENDIX A</b>	<b>66</b>
<b>A1.</b> Thermo-metallurgical input file	66
<b>A2.</b> Fortran code for radiation flux	68
<b>A3.</b> Fortran code for thermal contact conductance flux	69
<b>A4.</b> Fortran code for the model of the Tig welding arc	69
<b>A5.</b> Metallurgical input file used in SYSWELD (Material 1)	70
<b>A6.</b> Metallurgical input file used in SYSWELD (Material 2)	70
<b>APPENDIX B</b>	<b>71</b>
<b>B1.</b> Thermal properties for Material 1	71
<b>B2.</b> Mechanical properties for Material 1	71
<b>B3.</b> Thermal properties for Material 2	76
<b>B4.</b> Mechanical properties for Material 2	76
<b>APPENDIX C</b>	<b>78</b>
Equations used in Stress-Strain Experimental Measurements	78
Strain Measurement	79

## LIST OF FIGURES

---

2.1 Lagrangian description of body motion	6
3.1 The Welding Mega-System	13
3.2 Translation of the yield surface	16
4.1 Cross-sectional view of a manual Tig welding torch	21
5.1 (a) Discretized mesh to show translation of the arc in the Y-direction (b) Shape of the arc used for the welding simulations	23
5.2 Discretized welded plates with clamping scheme	24
6.1 Discretized meshes used for the benchmark problem	25
7.2.1 Heat affected zones caused by variation of TIG welding current on 8mm, 13mm and 20mm plates.	28
7.2.3 Diagram showing the depth $h$ and width $b$ of the molten region caused by a welding process	29
7.2.4 Graphical representation of (a) the width of penetration versus welding current and (b) the depth of penetration versus welding current	29
7.2.2 Heat affected zones with corresponding penetration	30
7.2.5 Graphical representation of the temperature achieved at the end of the weld versus (a) the depth and (b) width of penetration.	31
7.2.6 Heat affected zones produced by various welding speeds	33
7.2.7 Penetration caused by various welding speeds	34
7.2.8 Temperature achieved upon completion of welding versus corresponding welding speed.	34
7.2.9 HAZ, martensetic fraction, penetration, and initial material fractions achieved due to welding plates with and without pre-heating.	36
7.3.1 Stress contour in X-X plane caused by the welding process	37



7.3.2 (a) Temperature along <i>SECTION O-O</i>	38
7.3.2 (b) Temperature along <i>SECTION S-S</i>	39
7.3.2 (c) Temperature along <i>SECTION C-C</i>	40
7.3.2 (d) Temperature along <i>SECTION A-A</i>	41
7.3.3 (a) S11 stress along <i>SECTION O-O</i>	42
7.3.3 (b) S11 stress along <i>SECTION S-S</i>	43
7.3.3 (c) S11 stress along <i>SECTION C-C</i>	44
7.3.3 (d) S11 stress along <i>SECTION A-A</i>	45
7.3.4 (a) Temperature along <i>SECTION R-R</i>	46
7.3.4 (b) S11 stress component along <i>SECTION R-R</i>	47
7.3.5 (a) Temperature through thickness of the plate at a point P, identified in Fig. 7.3.1	48
7.3.5 (b) S11 stress through the thickness of the plate at a point P, identified in Fig. 7.3.1	49
7.3.6 Welding distortions: (a) Transverse shrinkage, (b) Longitudinal shrinkage, (c) Angular change in butt weld	50
7.3.7 Displacement and distortion in the X-X direction	50
7.3.8 Various views of the deformation in the X-X direction, caused by the Tig welding process and shows longitudinal, transverse and angular distortion	51
7.3.9 Residual displacement and distortion in the X-X direction	51
7.3.10 (a) Displacements along <i>SECTION A-A</i>	52
7.3.10 (b) Displacements along <i>SECTION C-C</i>	53
7.3.10 (c) Displacements along <i>SECTION O-O</i>	54
7.3.11 Influence of welding current on stress	55
7.3.12 Maximum values of compressive stress from Fig. 7.3.13 versus welding current	56

7.3.13 Stress contours caused by different welding speeds.	
(a) 2.5mm/s	
(b) 5mm/s	
(c) 7.5mm/s	57
7.3.14 Stress contours for various clamping schemes	58
8.1 Test rig used for welding experiments	59
8.2 TIG torch moving along the welding line	
(a) TIG torch somewhat at the beginning	
(b) TIG torch in the middle of the plate	60
8.3 Penetration and HAZ regions for	
(a) experiment 1	
(b) experiment 2	61
8.4 Photo showing the position of the strain gauge on the plate as well as the strain measuring device	61
8.5 Photo showing the Hole Drilling Technique	62
8.6 Residual stress component $S_{xx}$ evaluated for TIG data of run 2 of Table 7.1	62



**LIST OF TABLES**

---

5.1 Heat source efficiencies	23
6.1 Chemical compositions of the two materials	25
7.1 Welding variables used for simulations conducted with Material 2	29
7.2 Prediction depth and width of penetration versus welding current	31
7.3 (a) Correlation between depth and of penetration and temperature	32
7.3 (b) Correlation between width of penetration and temperature	32
7.4 Welding operating parameters used in sensitivity analysis of welding speed for Material 2	34
7.5 Prediction of welding speed versus corresponding temperature	35
7.6 Correlation of welding current versus absolute stress values	56
8.1 Welding operational parameters used inwelding experiments	60
8.2 Comparison of experimental and numerical results	60

## CHAPTER 1

### INTRODUCTION

---

#### 1.1 Influence of Residual Stresses on the Quality of Welded Components

Welded joints are often the weakest and most common location for the formation of excessively large regions of residual stresses and in some cases, local fracturing. These occurrences may shorten the service life of a welded component and usually happens when the welding procedure that was chosen for the weld was not correctly designed or executed. Residual stress states are of great importance to designers of welded components. These stresses are generated in a component during welding due to thermal energy and they are difficult to relieve. The relief or redistribution of residual stresses is expensive and in some cases incomplete. Residual stresses are those that are present in a material in the absence of any external mechanical loading. Residual stresses and consequent distortions are inseparable phenomena. The residual stresses arising from any welding process have two significant consequences on the resulting welded component: they give rise to distortion, which in turn result in dimensional non-conformance; they potentially reduce the service life of the welded component. Fractures that occur in the bead and regions surrounding it, are usually caused by the formation of undesirable metallurgical phases like bainite or martensite. The martensitic phase, which is hard and brittle, is prone to failure during cyclic loading.

The prediction of residual stresses and these undesirable phases caused by a welding process, and hence the performance of the welded structure under loading conditions, is a formidable task. This is due to the highly transient nature of the heat transfer during the welding process and the associated metallurgical changes. In this thesis, a formulation of the mathematical model of a welding process will be performed to assist in the prediction of these residual stresses and phases. Computational welding simulations will also be performed to show the welding industry the advantages of this type of work.

#### 1.2 Occurrence of Residual Stresses

Residual stresses also referred to as internal stresses, inherent stresses, reaction stresses, and locked-in stresses are those stresses that continue to exist in a material when all external loads have been removed. Termed thermal stresses are residual stresses that occur in a body that was subjected to a non-linear temperature change. These residual stresses have a significant effect on the service life of a joint and they are representing datum stresses over which the service load stresses are subsequently superimposed. If the applied stress and residual stress are of opposite nature like tensile and compressive ones, then a part of the service load goes to reduce the residual stress before the combined stress can again rise to some likely failure value. Such residual stresses are thus beneficial to the strength of the component, and significantly higher fatigue strengths can be achieved.



If, however, the residual stresses are of the same nature as the applied stresses, i.e. both tensile or both compressive, then a smaller service load could result in a failure than in the case for the zero initial stresses. The strength and fatigue life of the component in this case is reduced.

For this reason the deduction can be made that the magnitude and the sign (+ or -) of residual stresses present in a welded component is of great importance when considering fatigue. Residual stresses in metal structures occur due to many reasons during various manufacturing operations. They occur in many structural elements, including plate, bar, and sections, and can be formed during rolling, casting or forging. They occur during forming and shaping of metal parts by such processes as shearing, bending, machining, and grinding.

Processes of heat treatment, applied at various stages during the manufacturing of a component, can also produce the residual stresses or release existing ones. An example of stress-relieving is annealing, when heat treatment reduce residual stresses, and in contrast to this is quenching.

Because a bead and a parent material are heated locally by the welding heat source, the temperature distribution in these bodies is not uniform and changes as welding progresses. Along with this, the welded component undergoes shrinkage and expansion during welding. It can thus be seen that in all welded components some amount of residual stresses will be present upon the completion of welding, either on a microscopic or macroscopic scale.

The level of residual stress, that is found in any welded component, depends on a number of factors such as: heat input determined by current and voltage, the electric arc speed, environmental conditions, and pre- and post- heat treatments. Only a few of these welding variables have a significant effect on formation of resulting residual stresses. Later in this thesis, the effect that these variables have on each other will be examined.

### **1.3 Remarks on Computational Welding Mechanics**

Transient thermal residual stresses and deformations caused by welding have been recognized and studied since the 1930's[21]. Because the analysis of the subject requires complex computations involving the transient phenomena of plastic deformation, most studies in the past were primarily empirical and/or limited to the analysis of simple cases. Welding is in fact a very complex thermo-metallurgical-mechanical problem and involves four disciplines: thermodynamics, materials science, continuum mechanics and production engineering. A mathematical model of welding requires specific assumptions and experimental verification related to metallurgical and fracture toughness tests of welded joints.

Initially, experimental procedures were used to determine changes in welded structures during welding. Simple mathematical models of welding were proposed by Vinokurov [37] and Okerblom [22] to determine residual stresses. The phenomenon of heat transfer



in the welded component was firstly studied as a steady state heat transfer process and solved by Rosenthal [33] by applying Fourier's analysis. The current strategy for the modeling of welding was refined in the 1970's and 1980's with works by Hibbit and Marcal [12], Ueda and Yamakawa [36], Friedmann [7] and Masubuchi [20], and Anderson [1].

The simplified model of welding was formulated by various researchers for:

- The two dimensional problem in plane strain or axi-symmetric conditions,
- Elastic-plastic materials with temperature dependant properties,
- Lagrangian description of motion,
- The heat flux transferred from the arc to the body modeled as a prescribed heat flux,
- Thermal stresses evaluated below some bounding temperatures.

The first significant attempt to use computers in analysis of thermal stresses, occurring during welding, was done by Tall [21] in 1961. He developed a simple program for assessment of thermal stresses in a bead deposited on the top of welded plate. In 1968 Mashubuchi, Simmons and Monroe [21] developed a simple FORTRAN program based on Tall's analysis of one-dimensional welding model. Since 1970, computational analyses of residual stresses and distortion in welded components have become more common. Investigators developed computer based techniques for analysis of transient stresses, thermal stresses, and distortion in various components. The finite element method was widely used to study the stresses caused by a welding process under very complex boundary conditions. These results were however inconclusive, because the metallurgical structures and their changes were not considered. Since the 1980's research has been done on these aspects of welding mechanics. Investigators have succeeded in the coupling of the thermal and metallurgical phenomena occurring during welding. The evolution of thermal and metallurgical material characteristics due to welding can then be used to calculate thermal stresses, residual stresses and distortions. Investigators are now looking at combining the thermal, metallurgical and mechanical aspects of a welding process.

In 1980, Masubuchi [20] published a book covering many subjects related to residual stresses and distortion in welded structures. In 1984, Goldak, Chakravarti and Bidy [8] developed a finite element model for welding heat sources. In 1986 Leblond, Mottet and Devaux [13] performed works in the mathematical modeling of plastic behaviour of materials during phase transformations. Denis, Gautier and Simon [4] in 1989 did a study of the mechanical behavior of steels during phase transformation. In 1991 Estrin [6] developed a constitutive model for high temperature usage. Multi-pass welding have been modeled by Rybicki [34] and Leung [18]. The model consists of the lumping together of several passes to reduce the cost of separate analysis. In several cases only the last pass



was analysed. In 1996, Ronda and Oliver [32] successfully performed the simulation of a 16 pass weld. In this analysis however, each pass was analyzed to determine the effect that the welding would have on the final welded component. Ronda, Marenholtz and Hamann studied the phenomenon of under-water welding [27]. In 1993 Ronda, Oliver and Meinert [31] performed work on the simulation of welding with phase transformations and in 1994 Oliver [23] studied the modeling of welding with various thermo-visco-plastic constitutive models for steels. The formulation of the mathematical and finite element models that will be used in this text, follows [23] [28], while the model for transformation plasticity will be based on the work performed by Bergheau and Leblond [3]. Ronda, Estrin and Oliver [30] compared results of two welding simulations applying the thermo-mechano-metallurgical (TMM) constitutive model, proposed by Ronda and Oliver, and the thermo-visco-plastic material model proposed by Estrin. They found that the average stress distribution for the TMM model is smaller than that for the Estrin model because the transformation induced plasticity causes additional dissipation of internal energy in the TMM constitutive model.

The successful use of numerical techniques in the field of welding mechanics has provided an effective means of identifying and solving complex welding problems. The modeling of welding requires understanding of the various phenomena related to the specific welding procedure that will be simulated. These aspects include the modeling of the *heat affected zone* (HAZ), the heat exchange between the HAZ and the environment, and the internal heat sources formed in the material due to solid-liquid and solid-solid phase transformations.

For the best understanding of welding and modeling of related phenomena the author chose to study the works by Ronda and Oliver [23], [28]. The complete formulation of these models will be shown in this thesis.

The material model refined in this text, determined by stress-strain constitutive relations and evolution equations for solid phases, is based on works by Bergheau and Leblond [3], [14], [15], [16] and [17].

The finite element model of welding, formulated by Ronda and Oliver [28], has not yet been fully incorporated into a completed numerical program, and for this reason, a commercial software: SYSTUS-SYSWELD 2 is used to simulate welding where the Leblond material model is implemented.

In the thesis numerical simulations are performed to study the sensitivity of residual stresses subject to variations of welding variables. In addition to this the shape and size of the resulting HAZ and deformations are considered. Welding parameters include, amongst others, the heat source produced by the electric arc, related to the current and voltage, the arc travel speed, initial temperature and clamping of joint. The results of these simulations are verified using semi non-destructive stress measurements.

The heat source is modeled here as a Gaussian distribution, and the finite element method will be used to perform the analysis. The general finite element package SYSTUS, but



specifically the module SYSWELD 2 is utilized for these welding simulations. SYSWELD 2 can determine residual stresses and strains resulting from welding or heat treatments (quenching, induction quenching and surface treatments).

#### 1.4 General capabilities of software used for the welding simulations

The program SYSWELD 2 uses the finite element method and accounts for metallurgical transformation effects on thermal and mechanical behavior of structures. The evaluation of material microstructure, temperature and residual stresses consists of two sequential stages.

Firstly, the temperature field and solid phase proportions are evaluated considering the coupling of thermal and metallurgical phenomena, latent heat and material properties dependent on metallurgical phases.

Phase proportions determine welded material as the solid phase mixture. Material characteristics of welded bodies are defined by applying so called mixture rule:

$$\text{material property of a mixture} = \sum_{\text{number of phases}} \text{phase property} \times \text{phase proportion} .$$

Residual stresses and distortions can be determined knowing the temperature field and phase proportions.

This part of thermo-mechano-metallurgical analysis is identical with the classical thermo-plastic analysis and includes effects due to metallurgical transformations. Mechanical properties are dependent on phases and metallurgical transformations. This involves both volume variations and transformation plasticity. The model for transformation plasticity used in SYSWELD 2, has been developed by Leblond in [14], [15], [16] and [17].

The SYSTUS and SYSWELD 2 programs are very sophisticated computational tools. They are employed to simulate welding with considering of boundary conditions expressed in terms of radiation, convection and conduction, which determine effects of interaction of heat sources with environment, and mechanical, chemical and thermal phenomena occurring in a welded body.

The correlation between numerical and experimental results is validated by comparison of CCT diagrams: one introduced with material data for welded materials and the second one produced by the system after completing numerical calculations.

The numerical simulation of welding helps in understanding of interaction of coupled thermo-mechano-metallurgical phenomena involving solid phase transformations driven by thermal or mechanical or both energies. The parametric sensitivity analysis of residual stresses and distortions subject to welding parameters contributes to the assessment of the welding quality.



## CHAPTER 2

## MATHEMATICAL MODEL OF WELDING

## 2.1 Abstract

The welding process is formulated as the coupled thermo-mechanical problem with solid phase transitions and interactions with environment.

## 2.2 Lagrangian Description of Body Motion

The initial configuration of a body in the Lagrangian description of motion is the reference configuration and is usually used when boundary conditions are referred to the initial configuration. This motion can be seen in **Fig. 2.1**.

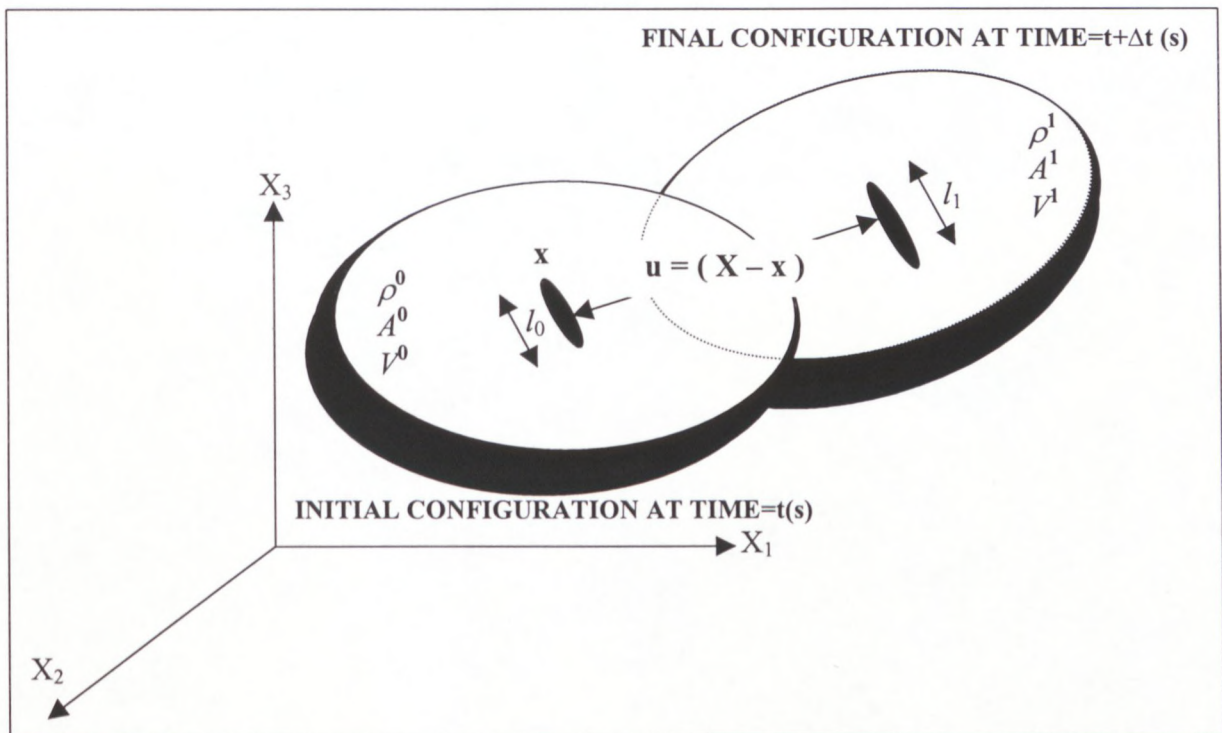


**Figure 2.1** Lagrangian Description of Body motion: the motion of a body particle from an initial time configuration ( $\mathbf{x}$  and  $t$ ) to a final time configuration at ( $\mathbf{X}$  and  $t+\Delta t$ )

The displacement  $\mathbf{u}(\mathbf{X}, t)$  and temperature  $\theta(\mathbf{X}, t)$  in a weld joint are unknown and the initial position of the particle  $\mathbf{X} = (X_1^0, X_2^0, X_3^0)$  and the time  $t$  are taken as independent variables. The vector joining the point  $\mathbf{X}$  and its actual position in the space  $\mathbf{x} = (X_1^1, X_2^1, X_3^1)$  is the displacement vector given by  $\mathbf{u} = \mathbf{X} - \mathbf{x}$ .

### 2.3 Constitutive Variables

The constitutive variables i.e., the stress and strain measures used in the Lagrangian formulation are the second Piola-Kirchoff stress tensor and the Green-Lagrange strain tensors [2]. The second Piola-Kirchoff stress tensor  $\hat{\mathbf{S}}$ , is given in terms of the Cauchy stress tensor  $\mathbf{T}$  by

$$\hat{\mathbf{S}} = \frac{\rho^0}{\rho^1} \mathbf{F}^{-1} \mathbf{T} \{\mathbf{F}^{-1}\}^T, \quad (2.3.1)$$

where,  $\rho^0$  and  $\rho^1$  are the initial and current densities.

The deformation gradient is given by

$$\mathbf{F} = \frac{\partial \mathbf{x}}{\partial \mathbf{X}}; \quad F_{iK} = x_{i,K} = \frac{\partial x_i}{\partial X_K}; \quad (2.3.2)$$

where  $\mathbf{x}$  and  $\mathbf{X} = \chi(\mathbf{x}, \mathbf{t})$  are the initial and current co-ordinates, respectively. The Green-Lagrange strain conjugate with the second Piola-Kirchoff stress is defined by:

$$\mathbf{L} = \frac{1}{2} (u_{I,J} + u_{J,I} + u_{K,I} u_{K,J}), \quad (2.3.3)$$

where the displacement gradient is defined as:

$$u_{I,J} = \frac{\partial u_I}{\partial X_J}. \quad (2.3.4)$$

The large indices I, J, K refer to the reference configuration. The ‘,’ is the notation for the derivative with respect to co-ordinates.

### 2.4 Balance Laws for the Thermo-Mechanical Process

The mathematical model of welding consists of two principles expressing thermal and mechanical equilibrium, i.e. the balance of internal energy and the balance of momentum. According to [23], [28], these principles have been derived to account for the coupling of thermal and mechanical effects in thermo-inelastic body. The equilibrium equation for a particle  $\mathbf{X} \subset \Omega$  is given by the following equation:

$$\left( \hat{S}_{KL} x_{i,L} \right)_{,K} - (b_i + r_i) \rho_0 = 0, \quad (2.4.1)$$

where  $\mathbf{x}$  is the current position of  $\mathbf{X}$  and  $b_i$  is the body force,  $r_i$  is the surface force, and  $\Omega$  is the body interior.

The equilibrium equation for a particle  $\mathbf{X} \subset \partial\Omega$  of a body is

$$\hat{S}_{KL} x_{i,L} N_K = T_i, \quad (2.4.2)$$

where  $N_K$  is the normal outward vector to the body surface  $\partial\Gamma$  and  $T_i$  is the nominal stress vector, and  $\partial\Omega$  is the body surface.

Assuming that the actual co-ordinate system  $\{\mathbf{X}_i\}$ , is collinear with the initial/reference co-ordinate system  $\{\mathbf{x}_i\}$ , these equations can be rewritten in the following form:

$$\left( \hat{S}_{KL} + \hat{S}_{KL} u_{I,L} \right)_{,K} - (b_i + r_i) \rho_0 = 0, \quad (2.4.3)$$

$$\left( \hat{S}_{KL} + \hat{S}_{KL} u_{I,L} \right) N_K = T_i.$$



From the balance of internal energy, a simple ‘heat equation’ [23], [28] for an inelastic conductor can be derived

$$\rho C_v \dot{\theta} + k_{IJ} \theta_{,JI} = f_{\theta}^B + f_{\theta}^S + \sum_J F_{\theta}^J, \quad (2.4.4)$$

### Heat fluxes and specific heat

Rate of heat generated due to dissipation of mechanical energy	$f_{\theta}^B = S_{IJ} \dot{L}_{IJ}$
Heat flux of arc and outfluxes due to convection and radiation.	$f_{\theta}^S = \text{ext} q_J N_J + R$
Concentrated heat fluxes:	$\sum_J F_{\theta}^J$
Specific heat:	$\rho C_v$
Temperature:	$\theta$

*It should be noted that the term determining heat generation due to mechanical dissipation of energy is not included in SYSWELD.*

Thermal conductivity  $\mathbf{k}$ , assumed to be the diagonal tensor, is defined by

$$k_{IJ} = \begin{bmatrix} k_{11} & 0 & 0 \\ 0 & k_{22} & 0 \\ 0 & 0 & k_{33} \end{bmatrix}.$$

Considering the simulation of droplet penetration during welding, the coefficients of conductivity are assumed to be anisotropic and the relations for these coefficients are given in [23]. However, for this analysis conductivity terms are constant because of material anisotropy.

Balance laws for momentum and internal energy can be expressed in the integral form and then approximated by Galerkin’s type Finite Element Method. A derivation of the functional forms of the balance laws consists of several steps described in [23], which lead to the following expressions:

$$\int_0 \hat{S}_{KL} u_{I,L} v_{I,K} dV + \int_0 (\hat{S}_{KI,K} + \hat{S}_{KL,K} u_{I,L}) v_I dV + \int_0 b_I v_I dV + \int_{\partial V_0} r_I v_I dP = 0 \quad (2.4.5)$$

$$\int k_{IJ} \theta_{,I} \vartheta_{,J} dV - \int c \dot{\theta} \vartheta dV + \int f_{\theta}^B \vartheta dV + \int_{\partial V} \hat{f}_{\theta}^S \vartheta dP + \sum_J F_{\theta}^J \vartheta|_J = 0, \quad (2.4.6)$$

with

$$\int_{\partial V} \hat{f}_{\theta}^S \vartheta dP = \int_{\partial V} f_{\theta}^S \vartheta dP + \int k_{IJ} \theta_{,I} \vartheta dP, \quad (2.4.7)$$

where  $V = \{v, \vartheta | v, \vartheta \in W_2^1\}$  is a space of weighting functions (or variations) which corresponds to the class of trial solutions  $S = \{u, \theta | u, \theta \in W_2^1\}$ , and  $W_2^1$  is the Sobolev space: once-differentiable and square integrable.

Stationarity conditions for the functionals defined by Eqs. (2.4.5) and (2.4.6) are expressed by the following variational equations:

$$\int_{V_0} \hat{S}_{KL} u_{I,L} \delta v_{I,K} dV + \int_{V_0} (\hat{S}_{KI,K} + \hat{S}_{KL,K} u_{I,L}) \delta v_I dV + \int_{V_0} b_I \delta v_I dV + \int_{\partial V_0} r_I \delta v_I dP = 0 \quad (2.4.8)$$

and

$$\int k_{IJ} \theta_{,I} \delta \vartheta_{,J} dV - \int c \dot{\theta} \delta \vartheta dV + \int f_{\theta}^B \delta \vartheta dV + \int_{\partial V} \hat{f}_{\theta}^S \delta \vartheta dP + \sum_J F_{\theta}^J v|_J = 0 \quad (2.4.9)$$

The generalised Gateaux derivative was applied in Equ. (2.4.9) because of discontinuity of thermal field on the surface of phase transformation, e.g. melting/solidification surface.

The generalised (weak) solution can be evaluated for  $\vartheta$  and  $v$ .

## 2.5 Finite Element Approximation of a Welding Process as a Coupled Thermo-Mechanical Problem.

The finite element method for the fully coupled thermo-mechanical problem is based on the Galerkin approximation of the two variational equations, i.e. the principle of virtual work Equ. (2.4.8) and the balance of internal energy Equ. (2.4.9). The discretization of the problem follows [23]. The equation of virtual work is solved by the Finite Element Method combined with linearization techniques for Finite Element Equations. Linearization is applied after the incremental decomposition of stress and strain tensors:

$$\mathbf{L}^{n+1} = \mathbf{L}^n + \mathbf{L}^0 \quad (2.5.1)$$

$$\hat{\mathbf{S}}^{n+1} = \hat{\mathbf{S}}^n + \hat{\mathbf{S}}^0, \quad (2.5.2)$$

where  $\{\mathbf{L}, \hat{\mathbf{S}}\}^{n+1}$  and  $\{\mathbf{L}, \hat{\mathbf{S}}\}^0$  correspond to the current and initial strain-stress states, and  $\mathbf{L}^0$  and  $\hat{\mathbf{S}}^0$  are increments of stress and strain. Following [23] and [28], increment of the Green-Lagrange strain  $\mathbf{L}^0$ , can further be decomposed into linear and non-linear parts defined by:

$$\mathbf{L}^0 = \mathbf{L} + \mathbf{L}_v, \quad (2.5.3)$$

$$\mathbf{L} = \frac{1}{2} (\Delta u_{I,J} + \Delta u_{J,I}) \text{ And,} \quad (2.5.4)$$

$$\mathbf{L}_v = \Delta u_{K,I} \Delta u_{K,J}. \quad (2.5.5)$$

The Finite Element equation for virtual work, shown in [2], for the total Lagrangian formulation is obtained from Equ. (2.4.8) and expressed for the time instant

$(n+1)$  by:

$$(\mathbf{K}_L^n + \mathbf{K}_{NL}^n) \Delta \mathbf{u}|_{(t)} = \mathbf{R}_u^{n+1} - \mathbf{F}^{n+1}|_{(t-1)}, \quad (2.5.6)$$

where,

$\mathbf{K}_L^n$  : linear strain stiffness matrix,

$\mathbf{K}_{NL}^n$  : non-linear strain (geometric or initial stress) stiffness matrix,



- $\Delta \mathbf{u}|_{(i)}$  : vector of increments of the nodal point displacements in iteration  $i$ ,
- $\mathbf{R}_u^{n+1}$  : vector of externally applied nodal point loads at time  $n + 1$ , and
- $\mathbf{F}^{n+1}|_{(i-1)}$  : Vector of nodal point forces equivalent to the element stresses at time  $(n + 1)$  and iteration  $(i - 1)$ .

This equation is linear in respect of  $\Delta \mathbf{u}|_{(i)}$ . Matrices in Equ. (2.5.6) are taken at four levels of solutions. These matrices are evaluated at two time steps,  $t$  and  $(t + \Delta t)$ , and for two iterations  $i$  and  $(i - 1)$ . The linear stiffness matrix is defined by:

$$\mathbf{K}_L^n = \int_{V_0} [\mathbf{B}_L^n]^T \hat{\mathbf{C}} \mathbf{B}_L^n dV, \quad (2.5.7)$$

The meaning of the matrices  $\mathbf{B}_L^n$  and  $\hat{\mathbf{C}}$  comes from the following expression:

$$\left( [\mathbf{B}_L^n]^T \Delta \mathbf{u}^T \right) \hat{\mathbf{C}} (\mathbf{B}_L^n \Delta \mathbf{u}) = \mathbf{L}^T : \hat{\mathbf{C}} : \mathbf{L} \quad (2.5.8)$$

The matrix  $\hat{\mathbf{C}}$ , is the *consistent or algorithmic tangent modulus* [23], [28], which may

be defined for a specific material model as  $\left[ \frac{\partial \hat{\mathbf{S}}}{\partial \mathbf{L}} \right]^n$  to the global stiffness matrix, and

$\mathbf{B}_L^n$  is the linear strain-displacement matrix. It should be noted, that in regions where elastic material behaviour is present, the consistent tangent modulus  $\hat{\mathbf{C}}$ , can be given by the components of the constant elastic tensor. For three-dimensional problems  $\hat{\mathbf{C}}$  can be expressed by

$$C_{ijrs} = \lambda \delta_{ij} \delta_{rs} + \mu (\delta_{ir} \delta_{js} + \delta_{is} \delta_{jr}), \quad (2.5.9)$$

where  $\lambda$  and  $\mu$  are the Lamé constants, bulk modulus and shear modulus which are defined by:

$$\lambda = \frac{E(\theta)\nu(\theta)}{[1 + \nu(\theta)][1 - 2\nu(\theta)]}, \quad \mu = \frac{E(\theta)}{2[1 + \nu(\theta)]}. \quad (2.5.10)$$

The Kronecker delta is

$$\delta_{ij} = \begin{cases} 0; & 1 \neq j \\ 1; & 1 = j \end{cases}$$

Young's modulus and Poisson's ratio for the TM problem are temperature dependent. The non-linear stiffness matrix is defined by:

$$\mathbf{K}_{NL}^n = \int_{V_0} [\mathbf{B}_{NL}^n]^T \hat{\mathbf{S}} \mathbf{B}_{NL}^n dV, \quad (2.5.11)$$

The sense of the non-linear strain-displacement matrix  $\mathbf{B}_{NL}^n$  comes from the expression

$$\left( [\mathbf{B}_{NL}^n]^T \Delta \mathbf{u}^T \right) \hat{\mathbf{S}} (\mathbf{B}_{NL}^n \Delta \mathbf{u}) = \hat{\mathbf{S}} : \mathbf{L}_v, \quad (2.5.12)$$

where  $\hat{\mathbf{S}}$  is the matrix representation of the second Piola-Kirchoff stress. The linear and non-linear stiffness matrices are not modified in the iteration process at the step  $(n + 1)$ . They are updated, when the iteration process is completed. The vector of externally applied loads at nodal points is given by

$$\mathbf{R}_u^{n+1} = \int_{\partial V_0} [\mathbf{H}_s]^T \mathbf{r}^{n+1} dP + \int_{\partial V} [\mathbf{H}]^T \mathbf{b}^{n+1} dV, \quad (2.5.13)$$

where  $\mathbf{H}_s$  is the surface interpolation matrix,  $\mathbf{H}$  is the volume interpolation matrix,  $\mathbf{r}^{n+1} = \{r_i\}$  is the nominal stress vector, and  $\mathbf{b}^{n+1} = \{b_i\}$  is vector of body forces. The vector of nodal point forces equivalent to the stresses at time  $(n + 1)$  and defined by the previous iteration  $(i - 1)$  is expressed in the form:

$$\mathbf{F}^{n+1}\Big|_{(i-1)} = \int_{V_0} \mathbf{B}_L^n \hat{\mathbf{S}}^{n+1}\Big|_{(i-1)} dV. \quad (2.5.14)$$

The Galerkin type Finite Element Method also approximates the variational equation for the balance of internal energy (Equ. (2.4.9)). The appropriate *Finite Element Equation* for the fully coupled thermo-mechanical problem is given by:

$$\mathbf{C}^n \dot{\theta}^{n+1}\Big|_{(i-1)} + (\mathbf{K}_k^n + \mathbf{K}_c^n + \mathbf{K}_r^n) \Delta\theta\Big|_{(i)} = \quad (2.5.15)$$

$$\mathbf{F}_{c(\theta)}^{n+1}\Big|_{(i-1)} + \mathbf{F}_{r(\theta)}^{n+1}\Big|_{(i-1)} + \mathbf{F}_{k(\theta)}^{n+1}\Big|_{(i-1)} - \mathbf{F}_{\Theta(\theta)}^{n+1}\Big|_{(i-1)}$$

where  $\mathbf{K}_k^n$  is the stiffness matrix corresponding to conduction,  $\mathbf{K}_c^n$  is the stiffness matrix related to convection, and  $\mathbf{K}_r^n$  is the stiffness matrix associated with radiation effects. The right hand side vectors are the thermal loads,  $\mathbf{F}_{c(\theta)}^{n+1}\Big|_{(i-1)}$ ,  $\mathbf{F}_{r(\theta)}^{n+1}\Big|_{(i-1)}$ , and  $\mathbf{F}_{k(\theta)}^{n+1}\Big|_{(i-1)}$  corresponding to thermal boundary conditions while,  $\mathbf{F}_{\Theta(\theta)}^{n+1}\Big|_{(i-1)}$  is the internal heat flux through the body surface. Terms of Equ. (2.5.15), are defined by:

$$\text{Heat capacity matrix} \quad : \quad \mathbf{C}^n = \int_{V_0} \mathbf{H}^T (\rho C_v)^n \mathbf{H} dV \quad (2.5.16)$$

$$\text{Conductivity matrix} \quad : \quad \mathbf{K}_k^n = \int_{V_0} \mathbf{B}^T \mathbf{k}^n \mathbf{B} dV \quad (2.5.17)$$

$$\text{Convection matrix} \quad : \quad \mathbf{K}_c^n = \int_{\partial V_0} \mathbf{H}^T h_c^n \mathbf{H} dP \quad (2.5.18)$$

$$\text{Radiation matrix} \quad : \quad \mathbf{K}_r^n = \int_{\partial V_0} \mathbf{H}^T \kappa \mathbf{H} dP \quad (2.5.19)$$

The RHS terms of Equ. (2.5.15) represent the thermal boundary conditions and internal heat fluxes. They are defined as the following vectors related to:

- convection boundary condition

$$\mathbf{F}_{c(\theta)}^{n+1}\Big|_{(i-1)} = \int_{\partial V_0} h_c^{n+1} \mathbf{H}_{s_c}^T \left[ \mathbf{H}_{s_c} \left( \theta_e^{n+1}\Big|_{(i-1)} - \theta^{n+1}\Big|_{(i-1)} \right) \right] dV \quad (2.5.20)$$

- radiation boundary conditions

$$\mathbf{F}_{r(\theta)}^{n+1}\Big|_{(i-1)} = \int_{\partial V_0} \kappa^{n+1} \mathbf{H}_{s_r}^T \left[ \mathbf{H}_{s_r} \left( \theta_r^{n+1}\Big|_{(i-1)} - \theta^{n+1}\Big|_{(i-1)} \right) \right] dP \quad (2.5.21)$$

- conductivity constitutive matrix

$$\mathbf{F}_{k(\theta)}^{n+1} = \int_V \mathbf{B}^T \left[ k^{n+1} \mathbf{B} \theta^{n+1}\Big|_{(i-1)} \right] dV \quad (2.5.22)$$

- heat fluxes in some nodal points

$$\mathbf{F}_{\Theta}^{n+1}\Big|_{(i-1)} = \mathbf{F}_{s_c}^{n+1}\Big|_{(i-1)} + \mathbf{F}_{s_r}^{n+1}\Big|_{(i-1)} \quad (2.5.23)$$

defined by

$$\mathbf{F}_{s_c}^{n+1}\Big|_{(i-1)} = \int_{\partial V_0} \mathbf{H}_{s_c} q_{s_c}^{n+1} dP \quad (\text{for convection}), \quad (2.5.24)$$

$$\mathbf{F}_{s_r}^{n+1}\Big|_{(i-1)} = \int_{\partial V_0} \mathbf{H}_{s_r} q_{s_r}^{n+1} dP \quad (\text{for radiation}). \quad (2.5.25)$$



## 2.6 Global Finite Element Equation for the fully coupled thermo-mechanical (TM) problem.

The combined Global Finite Element Equation for the fully coupled thermo-mechanical problem is expressed by

$$\begin{bmatrix} \mathbf{0} & \mathbf{0} \\ \mathbf{0} & \mathbf{C}^n \end{bmatrix} \begin{bmatrix} \mathbf{0} \\ \dot{\theta}^{n+1} \end{bmatrix}^{(i)} + \begin{bmatrix} \mathbf{K}_u^n & \mathbf{K}_{u\theta}^n \\ \mathbf{K}_{\theta u}^n & \mathbf{K}_\theta^n \end{bmatrix} \begin{bmatrix} \Delta \mathbf{u} \\ \Delta \theta \end{bmatrix}^{(i)} = \begin{bmatrix} \mathbf{R}_u^{n+1} \\ \mathbf{R}_\Theta^{n+1} \end{bmatrix} - \begin{bmatrix} \mathbf{F}_u^{n+1} \\ \mathbf{F}_\Theta^{n+1} \end{bmatrix}^{(i-1)}, \quad (2.6.1)$$

where  $\mathbf{K}_u^n$  is the stiffness corresponding to mechanical effects,  $\mathbf{K}_{u\theta}^n$  is the matrix related to the transformation of mechanical energy into thermal one, and matrix  $\mathbf{K}_{\theta u}^n$  transforms thermal energy into mechanical one. The thermal stiffness  $\mathbf{K}_\theta^n$  is the sum of  $\mathbf{K}_k^n$ ,  $\mathbf{K}_c^n$  and  $\mathbf{K}_r^n$ . The RHS vectors in Equ. (2.6.1) are defined by

$$\mathbf{F}_u^{n+1} \Big|_{(i-1)} = \mathbf{F}_u^{n+1} \Big|_{(i-1)}, \quad (2.6.2)$$

and

$$\mathbf{R}_\Theta^{n+1} = [\mathbf{F}_{\theta k} + \mathbf{F}_{\theta c} + \mathbf{F}_{\theta r}]^{n+1}. \quad (2.6.3)$$

## CHAPTER 3

## MATERIAL MODEL

## 3.1 The Welding Mega-System

The material model used in welding simulations accounts for heat flow, metallurgical phase transformations, classical plasticity and transformation plasticity. The scheme called Welding Mega-System (WMS) (Fig. 3.1) shows how various phenomena involved in welding interact with each other.

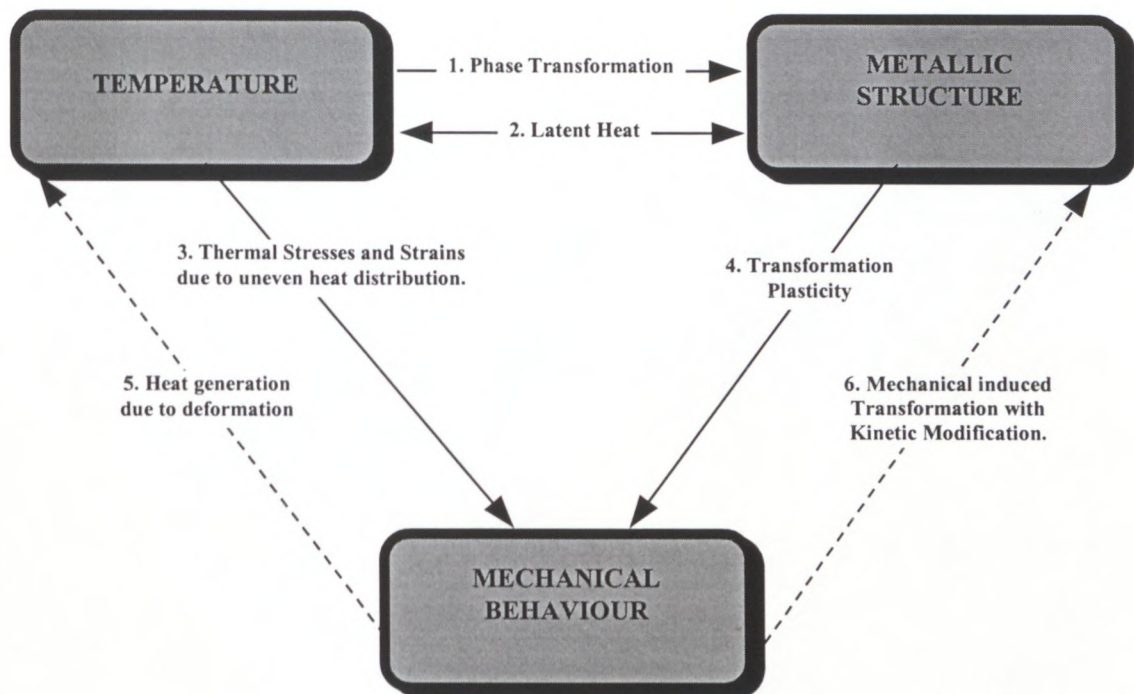


Figure 3.1 The Welding Mega-System

A welded body is a multiphase poly-crystalline alloy and is an assemblage of grains called a *mesodomain*. The mesodomain contains large number of *micro-regions* or dispersed particles. The micro-region is composed of a manifold of particles such as, e.g. crystals. A *phase* is a portion of a manifold of particles of an alloy whose properties and composition are homogeneous and which is physically different from other properties of an alloy.

A transformation of a daughter phase to a parent phase is directly related to the temperature history and internal stresses in a dispersed particle. In this analysis the Equilibrium Diagrams is used to determine when solid phase transformation occurs during heating. During cooling, the Continuous-Cooling-Transformation (CCT) diagram is used to determine phase transformations. It is assumed that the initial phase of the deposited material, i.e. bead, consists of austenite. This is justified because the bead is introduced into welded joint in its molten state. As the arc moves along the weld line, the bead solidifies and the austenite transforms to the various



daughter phases (pearlite, bainite, ferrite, martensite) as stipulated by the CCT-Diagram.

*It should be noted that the dotted lines in Fig. 3 indicates that these phenomena are not included in the model of welding implemented in FE programe SYSWELD used for simulation of welding*

### 3.2 Coupled Thermo-metallurgical Analysis

The modeling of the metallurgical transformations are dealt with in a purely phenomenological way [3]. The metallurgical model used in SYSWELD is used for this analysis. In metallurgical terms, a material is defined in terms of metallurgical phase fractions  $y_a$  (or percentages) of volume of the various phases (austenite, ferrite, pearlite, bainite, and martensite) in the volume of a mixture, where “a” represents the various phases and assumes values:  $a = 1, 2, 3, 4, 5$ . The metallurgical model used in this study follows the Johnson-Mehl-Avrami type of phase transformation kinetics and gives the current phase proportion  $y_a$  of phase  $a$  according to time  $t$  and temperature  $\theta$ . Following Bergheau and Leblond [3], when multiple transformation occurs in a material, Equ. (2.3.4) can be rewritten as

$$\left( \sum_{phases} y_a (\rho C_v)_a \right) \dot{\theta} + \left( \sum_{phases} y_a (k_{IJ})_a \right) \theta_{,JI} = f_{\theta}^B + f_{\theta}^S + \sum_J F_{\theta}^J - \sum_{phases} \dot{y}_a L_a, \quad (3.2.1)$$

where the specific heat and conductivity are dependent on the metallurgical phase fractions. The specific heat, following [3], is given in terms of the phase enthalpies  $H_a$ . For a given phase,  $a$ , it is given by

$$(\rho C_v)_a = \frac{\partial H_a}{\partial \theta}, \quad (3.2.2)$$

The last term on the RHS of Equ. (3.2.1) is related to the latent heat and in SYSWELD is included as the further volumetric heat source [3]. This is done because the temperature ranges of phase transformations are dependent on temperature rates and  $L_a$  is given by

$$L_a = H_1 - H_2 \quad (3.2.3)$$

The evolution of phase fractions  $\dot{y}_a$  in the Johnson-Mehl-Avrami model are defined by

$$\frac{dy_a}{dt} = n \frac{(y_{eq}(\theta) - y_a)}{Tau(\theta)} \left[ \ln \left( \frac{y_{eq}(\theta)}{(y_{eq}(\theta) - y_a)} \right) \right]^{(n-1)/n}. \quad (3.2.4)$$

This model is used for transformations during heating and cooling. The austenite proportion is given by  $y_i$ , and the equilibrium austenite proportion is given by  $y_{eq}$ , and can be read from the iron-carbon diagram,  $Tau(\theta)$  is a time constant which reproduces a retardation effect. During cooling, several transformations occur, depending on cooling rates

$$\dot{y}_a = -\frac{dy_a}{dt}. \quad (3.2.5)$$

Equ. (3.2.5) can be used for the calculations of phase fractions produced due to diffusional transformations during cooling.

The Koistinen-Marburger law is used to determine martensitic phase fraction produced during diffusion-less martensitic transformation, which is given by



$$y_m = 1 - \exp(-b[Ms - \theta]), \quad (3.2.6)$$

where  $y_m$  is the martensitic fraction,  $Ms$  is the temperature at the beginning of martensitic transformation,  $b$  is a coefficient, and  $\theta$  is the temperature.

### 3.3 Stress – Strain Constitutive Equations

*The effect of metallurgical transformations and multi-phase material structure on constitutive models of steels is considered in this section. The plasticity of steels can be ascribed to two occurrences [13]:*

- ◆ **Classical thermo-plasticity:** This is the phenomenon of permanent plastic deformation in materials arising from variations of stress above its yield limit as well as temperature.
- ◆ **Transformation plasticity:** This is the phenomenon of plastic flow in solids, which occurs in a softer phase due to mechanical interaction with a stiffer phase. This phenomenon has been studied by various researches (page 551 of [15]). It was found that the progression of a phase transformation occurring in a stressed metal induces a plastic deformation, even if the external stress and/or temperature remains constant.

The transformation plasticity deformation is produced by two mechanisms:

1. The **Greenwood-Johnson mechanism** [9] is observed when volume variations of two phases generate microscopic internal stresses. Such stresses are sufficient to produce plastic flow in a phase with the lower yield stress, even in the absence of any external stresses. If an external stress is superimposed, the internal one can be amplified or reduced. The resulting stress is producing a macroscopic strain determined by the direction of the applied stress.
2. The **Magee mechanism** [19] is associated with the martensitic transformation when a formation of martensitic plates in a preferred orientation affects the overall shape of the solid. Such structural transformation induces a displacement in a region undergoing transformation, and therefore a local strain variation.

Theoretical and experimental works [14] shown that the Magee mechanism can be neglected because the average value of Magee's term is infinitesimal, and therefore the TMM model of a welded body can be developed considering the Greenwood-Johnson mechanism solely.

The microscopic plastic deformation is affected by the plastic hardening that arises at least partly or often entirely due to the Greenwood-Johnson mechanism (page 573 of [17]). The concept of linear kinematic hardening, illustrated in **Fig. 3.2**, is utilized in the TMM analysis of welding.

In the Leblond model of TMM process, described in [15], [16], and [17], two phases are recognized: a softer phase, marked with the superscript 1, and a stiffer phase, marked with the superscript 2. The analysis is restricted to transformations occurring during cooling.



The total strain rate,  $\dot{L}^{total}$ , following (page 399 of [14]), can be decomposed additively into three terms and is given by

$$\dot{L}^{total} = \dot{L}^{el} + \dot{L}^{th} + \dot{L}^{pl}, \quad (3.3.1)$$

where  $\dot{L}^{el}$ ,  $\dot{L}^{th}$  and  $\dot{L}^{pl}$  are the elastic, thermal and plastic strain rates, respectively. The elastic strain rate can be evaluated from equations (page 46 of [23]) for classic elasticity

$$\dot{L}^{el[a]} = \frac{1}{\mu^{[a]}} \dot{S}_{ij}, \quad [a] = 1, \dots, 5 \quad (3.3.2)$$

where  $[a]$ , is taken for one of the phases,  $\mu^{[a]}$  is defined as the shear modulus of the specific phase and  $S_{ij}$  is the deviatoric macro-stress.

The total thermal strain rate for a material, which is a mixture of the five solid phases, can be evaluated (page 399 of [14], [23]) as the sum of individual phase thermal strains given by

$$\dot{L}^{th[a]} = \sum_{\text{phases}} y_a \alpha^{[a]} \dot{\theta}, \quad [a] = 1, \dots, 5 \quad (3.3.3)$$

where  $\alpha^{[a]}$  is the phase coefficient of thermal expansion. Following [14], [15] and [16], the plastic strain rate  $\dot{L}^{pl}$  could further be decomposed into three other terms given by

$$\dot{L}^{pl} = \dot{L}_{\sigma}^{cp} + \dot{L}_{\theta}^{cp} + \dot{L}^{tp}, \quad (3.3.4)$$

where the above contributions are represented by

$\dot{L}_{\sigma}^{cp}$ : classical plasticity proportional to a stress rate,

$\dot{L}_{\theta}^{cp}$ : classical plasticity proportional to a temperature rate,

$\dot{L}^{tp}$ : transformation plasticity.

General expressions for these components of the constitutive equation in (3.3.4) are given in [17].

The concept of kinematic hardening can be described in terms of a three-dimensional yield surface translation  $A_{ij}$ . The translation of the three-dimensional yield surface from an initial to a new configuration is shown in **Fig. 3.2**.

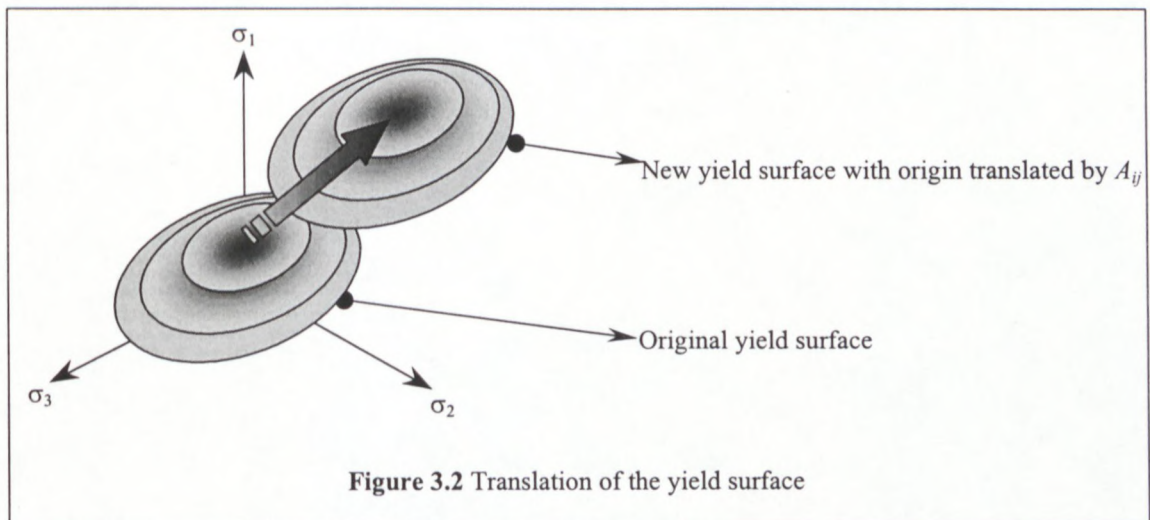


**Figure 3.2** Translation of the yield surface

For small external stresses, the deviators of the macroscopic stress  $S_{ij}^{[1]}$  and  $S_{ij}^{[2]}$  for phases 1 and 2 are almost equal and identical to the total macroscopic stress  $S_{ij}$ .  $S_{ij}$  is the average value of the microscopic stress deviator over the whole representative volume  $\mathbf{V}$ . This statement follows the hypothesis H5 on page 416 of [15].

Then the *equivalent stress* (page 579 of [17]), assuming the Huber-von Mises yield criterion, is defined by

$$\sigma^{eq} = \left[ \frac{3}{2} (S_{ij} - A_{ij})(S_{ij} - A_{ij}) \right]^{1/2}, \quad (3.3.5)$$

where the stress state and the tensor determining the translation of the yield surface center is given by

$$S_{ij} = (1 - y_a) S_{ij}^{[1]} + y_a S_{ij}^{[2]}, \quad (3.3.6)$$

$$A_{ij} = (1 - y_a) A_{ij}^{[1]} + y_a A_{ij}^{[2]}, \quad (3.3.7)$$

and  $y_a$  is the second phase volume fraction.

The translation tensor is related to plastic strain and can be splitted into two parts  $A^{[a]} = H^{[a]}(\theta) B^{[a]}$ ,

where  $H^{[a]}(\theta)$  is a temperature dependent material parameter and  $B^{[a]}$  is different in general from the plastic strain.

**The relation between the ultimate stress  $\sigma^Y$**  is defined by

$$\sigma^Y = (1-a)\sigma^{[1]Y} + a\sigma^{[2]Y}, \quad (3.3.8)$$

where  $\sigma^{[1]Y}$  and  $\sigma^{[2]Y}$  are the yield stresses for the individual phases, **and the maximum possible value of the equivalent stress  $\sigma^{eq}$  determine the two cases of the analysis following [17].**

**The first case when  $\sigma^{eq} < \sigma^Y$**

The evolution laws for the translation tensor  $B^{[a]}$  that also determines the evolution of  $A^{[a]}$  are

$$\dot{B}^{[1]} = \frac{1}{1 - y_a} (\dot{L}_\sigma^{cp} + \dot{L}_\theta^{cp} + \dot{L}^{tp}), \quad (3.3.9)$$

$$\dot{B}^{[2]} = -\frac{\dot{y}_a}{y_a} B^{[2]} + \phi \frac{\dot{y}_a}{y_a} B^{[1]}, \quad (3.3.10)$$

where  $\phi$  is called the memory coefficient in [17] and comprises between zero and one.

$\phi = 0$	no memory, full material recovery
$\phi = 1$	Complete memory, no recovery

The components of the plastic strain rates for this case are expressed as follows

$$\dot{L}^{tp} = -\frac{3\Delta\varepsilon^{th[1 \rightarrow 2]}}{\sigma^{[1]Y}} (S - A^{[1]}) h\left(\frac{\sigma^{eq}}{\sigma^Y}\right) (\ln y_a) \dot{y}_a, \quad (3.3.11)$$



$$\dot{L}_{\sigma}^{cp} = \frac{3(1-y_a)}{2\sigma^{[1]y}} \frac{g(y_a)}{E^{[a]}(\theta)} (S - A^{[1]}) \dot{\sigma}_s^{eq}, \quad (3.3.12)$$

$$\dot{L}_{\theta}^{cp} = \frac{3(\alpha^{[1]} - \alpha^{[2]})}{\sigma^{[1]y}} y_a \ln y_a (S - A^{[1]}) \dot{\theta}, \quad (3.3.13)$$

where

definition of the term	Formula
volume dilatation produced by phase 1 and 2 due to the temperature variation	$\Delta \varepsilon^{th[1 \rightarrow 2]} = L^{th[2]} - L^{th[1]} = \frac{1}{3} \frac{(\Delta v)^{[1 \rightarrow 2]}}{v}$
time derivative of $\sigma^{eq}$ obtained by considering $A^{[1]}$ as a constant (page 580 of [16])	$\dot{\sigma}_s^{eq} = \frac{3}{2\sigma^{eq}} (S_{ij} - A_{ij}^{[1]}) \dot{S}_{ij}$
	$\sigma^{eq} = \left[ \frac{3}{2} (S_{ij} - A_{ij}^{[1]}) (S_{ij} - A_{ij}^{[1]}) \right]^{1/2}$
Young's modulus	$E^{[a]}(\theta)$
functions deduced from numerical and theoretical test given on page 430 of [15].	$g(y_a), f(y_a), h(\sigma^{eq}/\sigma^Y)$

The argument  $\sigma^Y$  in the  $h$  function can be evaluated from the non-linear mixture rule given by Equ. (3.3.10) [16].

$$h\left(\frac{\sigma^{eq}}{\sigma^Y}\right) = \begin{cases} 1 & \text{if } \frac{\sigma^{eq}}{\sigma^Y} \leq \frac{1}{2} \\ 1 + 3.5 \left( \frac{\sigma^{eq}}{\sigma^Y} - \frac{1}{2} \right) & \text{if } \frac{\sigma^{eq}}{\sigma^Y} \geq \frac{1}{2} \end{cases} \quad (3.3.14)$$

The non-linear effect starts at  $\sigma^{eq} / \sigma^Y = \frac{1}{2}$ , which has been shown experimentally as a reasonable value [16]. The coefficient 3.5 in Equ.(3.3.14)<sub>2</sub> has been deduced from numerical simulations in [16].

It should be noted, that the transformation plasticity phenomenon is ‘‘cut off’’ when a phase fraction is less or equal to 3%. The evaluation based on Equ. (3.3.11). overestimates the value of  $\dot{L}^{tp}$  when the phase fraction is very small [16].

### **The second case when $\sigma^{eq} = \sigma^Y$**

The evolution laws for the yield surface translation is now given by

$$\dot{B}^{[1]} = \dot{E}^{pl}, \quad (3.3.15)$$

$$\dot{B}^{[2]} = \dot{E}^{pl} - \frac{\dot{a}}{a} B^{[2]} + \phi \frac{\dot{a}}{a} B^{[1]}. \quad (3.3.16)$$

The constitutive Equ. (3.3.4). reduces to:

$$\dot{L}^{pl} = \frac{3}{2} \frac{\dot{\varepsilon}^{eq}}{\sigma^{eq}} (S_{ij} - A_{ij}), \quad (3.3.17)$$

where the equivalent strain is given by

$$\varepsilon^{eq} = \left( \frac{3}{2} \dot{L}_{ij}^{pl} \dot{L}_{ij}^{pl} \right)^{1/2}. \quad (3.3.18)$$

The advantages of the Leblond model for the TMM processes in comparison with others proposed in [14] are the following:

- description of phase plastic deformations due to volume variations and external loads,
- an explicit set of constitutive equations for transformation plasticity related to the thermo-mechanical characteristics of a solid,
- transformation plasticity model for a solid with the kinematic strain hardening and the material memory effect.
- development of the finite element code for the TMM process that is incorporated into the SYSWELD program.



## CHAPTER 4

### DESCRIPTION OF TIG WELDING PROCESS

---

#### 4.1 Introduction

When selecting a joining process, a basic knowledge of the various processes and their relationships to variables such as joint design, base metal properties, equipment cost, and the type of operating process (manual or automatic) is required. For increased economy, many manufacturing industries are using automatic welding procedures with robotics, mechanical indexing, and positioning systems [21]. The success of any automated welding depends on the weldability of welded materials and utilised equipment.

Welding processes that use an electric arc are the mostly used in manufacturing industries. The arc may be established between an electrode and the base plates, as in shielded metal arc welding (SMAW) and gas tungsten arc welding (GTAW). The arc may also occur within the welding heat source, as in plasma arc welding (PAW). Furthermore, an inert gas, granulated flux, or gaseous slag products of a consumable electrode is used to protect the arc and molten metal against hydrogen penetration and oxidation.

The gas tungsten arc welding (GTAW), which is also known as the tungsten inert gas (TIG) welding process, is considered in this study because of the following features of weldment:

- no slag inclusions eliminates post weld cleaning,
- no weld spatter,
- the arc and weld pool are visible during welding which enables collection of data for numerical simulation,
- applicability for welding of ferrous and non-ferrous materials,
- it has the ability to join materials with refractory oxides (aluminium and magnesium) as well as reactive metals, which because of their affinity for oxygen and nitrogen can become embrittled if exposed to air in the molten state.

#### 4.2 Tungsten Inert Gas (TIG) welding process.

The TIG welding method is also called the Gas Tungsten Arc Welding (GTAW). TIG welding is a process in which the heat is produced between a non-consumable electrode and the work metal. The electrode, weld pool, arc and adjacent heated areas of the workpiece are protected from atmospheric contamination by a gaseous shield. A stream of gas (usually inert gas) or a mixture of gasses produces this shield which provides full protection against air can contamination of a weld pool.

The arc and weld pool are visible during the welding process. The filler wire is not transferred across the arc, thus eliminating weld spatter. Because the electrode is non consumable, welding of thin parts can be made by fusion of the base metal without



the addition of filler metal. However, a filler metal may be used depending on requirements established for a particular weld joint.

TIG welding can be applied in the manual, semi-automatic, machine or automatic methods and is applicable in all positions of welding. We are mainly focusing on the automatic welding process because of constant speed of welding and automated supply of filler metal. Metals that are TIG weldable include: carbon and alloy steels, heat resistant alloys, copper alloys, nickel alloys, titanium alloys, and zirconium alloys. TIG welding is also applicable to a wide range of base metal thickness. Because of the intense concentration of heat produced by the arc, high welding speeds can be obtained.

### 4.3 Fundamentals of the TIG process

The TIG welding process uses the heat produced by the arc and the non-consumable electrode (tungsten or tungsten alloy) and the workpiece. The weld bath situated in the centre of the heat-affected zone (HAZ) are inhibited from the atmosphere by an inert gas supplied by the TIG welding torch. The arc brings the workpiece and filler metal to the molten state. Welded parts are joined during solidification of welding bath.

**Fig. 4.1** shows a cross-sectional view of a manual TIG welding torch. **Fig. 4.1(a)** shows the flow of shielding gas and cooling water, while **Fig. 4.1(b)**, shows the electrical circuit.

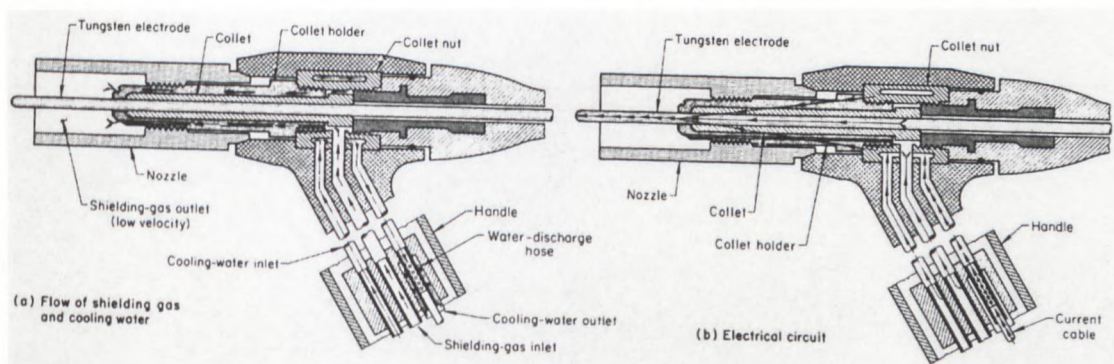


**Figure 4.1** Cross-sectional view of a manual TIG welding torch. (a) flow of shielding gas; (b) flow of cooling water

The electric arc is produced by the passage of current through the ionised inert shielding gas. The ionised atoms lose electrons and are left with a positive charge. The positive gas ions flow from the positive to the negative pole of the arc. The electrons flow from the negative to the positive pole. The power expended in arc is the product of the current passing through the arc and the voltage drop across the arc.



## CHAPTER 5

## THERMAL AND MECHANICAL BOUNDARY CONDITIONS

## 5.1 Model of the arc

The welding arc for the TIG process is modeled as a travelling heat flux defined by  $q$

$$q_{TIG} = \frac{Q}{v}, \quad (5.1.1)$$

where  $v$  is the surface of a weld pool,  $Q$  is the heat input given in terms of the welding current, welding voltage and efficiency for the process, and is given by

$$Q = \wp IV \quad (5.1.2)$$

with  $\wp$  being the process efficiency,  $V$  and  $I$  the welding current and the welding voltage respectively. The efficiencies of various welding processes can be seen in **Table 5.1**.

WELDING PROCESS	EFFICIENCY
Gas Tungsten Arc	0.20 – 0.50
Shielded Metal Arc	0.65 – 0.85
Gas Metal Arc	0.65 – 0.85
Submerged Arc	0.80 – 0.99
Electroslag	0.55 – 0.82
Gas	0.25 – 0.80
Electron Beam	0.80 – 0.95
Laser Beam	0.005 – 0.70

Table 5.1 Heat source efficiencies

The exponential function that follows the law of decay is used to model heat flux

$$q_{TIG} = P e^{-r^2}, \quad (5.1.3)$$

with  $P$  being the volumetric heat source that determines the magnitude and shape of the arc and is given by

$$P = \frac{\wp IV 4\sqrt{3}}{\pi\sqrt{\pi} r_m b c}, \quad (5.1.4)$$

where  $r_m$  is a distribution radius (mm),  $b$  and  $c$  are variables of the process (mm). The volumetric heat source  $P$  is measured in  $\text{W}/\text{mm}^3$ .

The translation of arc  $r$  is given by

$$r = \frac{3\left(\sqrt{(x-x_o)^2 + (y-y_o)^2 + (z-z_o)^2} - r_m\right)}{r_m^2 b^2 c^2}, \quad (5.1.5)$$

**Fig. 5.1** shows a finite element mesh of welded joint and the projection of an electric arc on the plate surface when the arc is moving in  $y$ -direction.

$y_0$  is given by

$$y_0 = v_c \cdot t \quad (5.1.6)$$

where  $v_c$  represents a speed of a weld travel and  $s$  is time.

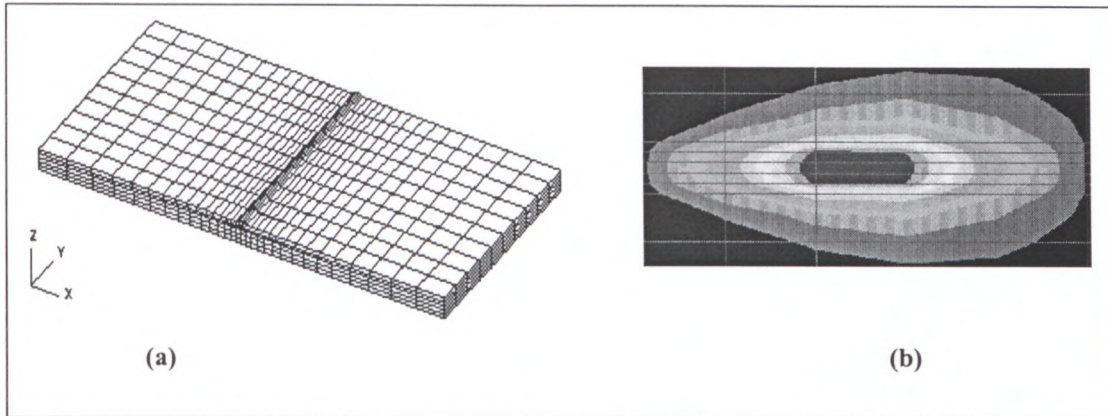


**Figure 5.1** (a) Discretized mesh to show translation of the arc in the Y-direction. (b) Shape of the arc to be used for the simulations.

## 5.2 Convection from a work piece

Thermal convection from the work piece was given by empirical relations [13] in terms of dimensionless constants. The flux due to thermal convection is given by

$$q_c = -h_c(\theta_s - \theta_e) \quad (5.2.1)$$

where the negative (-) sign implies that the flow of heat is out of the body,  $\theta_e$  is the known environmental temperature,  $\theta_s$  is the unknown surface temperature of the body, and  $h_c$  is the convection heat transfer coefficient that is calculated using the dimensionless constants, which are the Nusselt ( $Nu_f$ ), Grashof ( $Gr_f$ ), Prandtl ( $Pr_f$ ), and Rayleigh ( $Ra_f$ ) numbers.

## 5.3 Radiation from a work piece

The radiation coefficient [13] was given by

$$h_r = \sigma_s \varepsilon (\theta_s^4 - \theta_{sink}^4) \quad (5.3.1)$$

where  $\sigma_s$  is the Stefan Boltzmann constant,  $\varepsilon$  is the emmissivity of the particular material,  $\theta_s$  is the temperature of the surface undergoing radiation heat transfer, and  $\theta_{sink}$  is the temperature of the large enclosure where the welding is taking place. The heat flux due to radiation heat transfer is given by

$$q_r = -h_r(\theta_s - \theta_{sink}) \quad (5.3.2)$$

## 5.4 Thermal contact conduction

It is assumed that welded plates are located on a workbench. This effect causes a heat sink. Thermal contact relations are used to estimate the heat flux caused by the thermal contact conduction heat transfer [13]. This flux is given by

$$q_{cc} = -h_{cc}(\theta_s - \theta_{bench}) \quad (5.4.1)$$



where  $h_{cc}$  is the thermal contact conduction coefficient,  $\theta_s$  is the unknown temperature of the bottom surface of the plates, and  $\theta_{bench}$  is the temperature of the workbench.

### 5.5 Mechanical boundary conditions

The mechanical boundary conditions are simulating a simple clamping of plate sides and are shown in **Fig. 5.2**. This can be done by simply tack welding plates to the workbench. The clamped nodes in various benchmark problems considered in this paper can have one, two or three degrees of freedom ( $UX=0$ ,  $UX=UY=0$ ,  $UX=UY=UZ=0$ ).

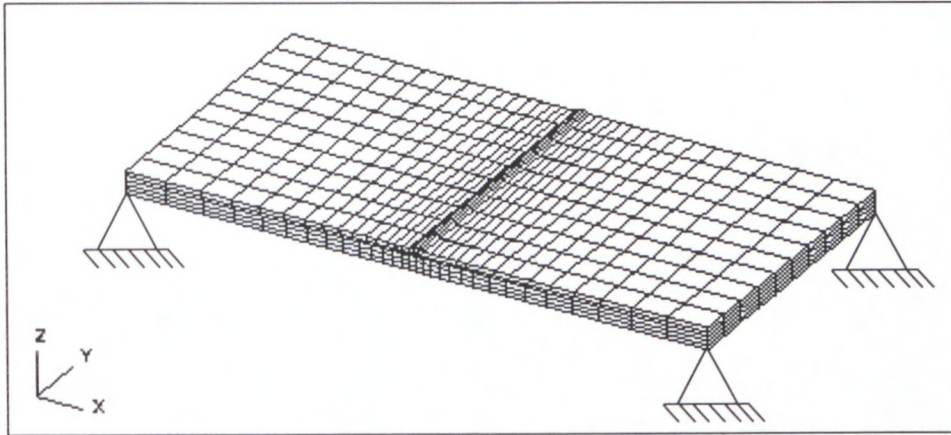


**Figure 5.2** Discretized welded plates with clamping scheme

The thermal boundary conditions into or out of the body are incorporated in SYSWELD 2 using simplified FORTRAN codes. These codes are shown in **APPENDIX A**.

## CHAPTER 6

## SIMULATION ASSUMPTIONS AND PROCEDURES

## 6.1 Bench Mark Problem

The bench mark problem that was considered for this study, is that of the welding of steel plates of varying thickness. The dimensions of the plates were 100mm by 100mm by 8mm, 13mm and 20mm. The electric arc welding process used for this study was the Gas Tungsten Arc (GTAW/Tig) welding process. Two materials were used in these simulations, and they will simply be called **Material 1** and **2**. The chemical compositions of these materials can be found in **Table 6.1**. The required material properties such as density, conductivity, Young's Modulus, Poisson's Ratio, Yield Stress, etc. is given in **APPENDIX A** and **B**. The metallurgical data can also be seen here.

	C	Mn	Si	S	P	Al	Mo	B
<b>Material 1</b>	0.18	1.39	0.37	0.011	0.022	0.052	-	-
<b>Material 2</b>	0.12 / 0.21	0.45 / 0.7	0.20 / 0.35	0.035	-	-	0.50 / 0.65	0.001 / 0.005

**Table 6.1** Chemical compositions of the two materials.

For ease of calculation, it was assumed that the base plates and bead were of the same material. The thickness of the consumable electrodes (either **Material 1** or **2**) were 2.5mm. The study encompasses the effects that welding current, weld travel speed, and pre-heating temperature have on the shape and size of the resulting HAZ region as well as the residual stress and deformation caused by the Tig welding process. The sides of the plates were firmly clamped to a workbench and this caused a heat sink effect. Thermal convection and radiation occurs from the top surface of the plates and bead. The arc moves across the volume of the bead so to simulate the effect of bead droplets. Since the forming temperature of the bead is so high, it was assumed that the initial phase of the bead material was be austenite. During cooling this phase will then transform to the other metallurgical phases (bainite, martensite, etc.). The finite element meshes for the three configurations can be seen in **Fig. 6.1**.

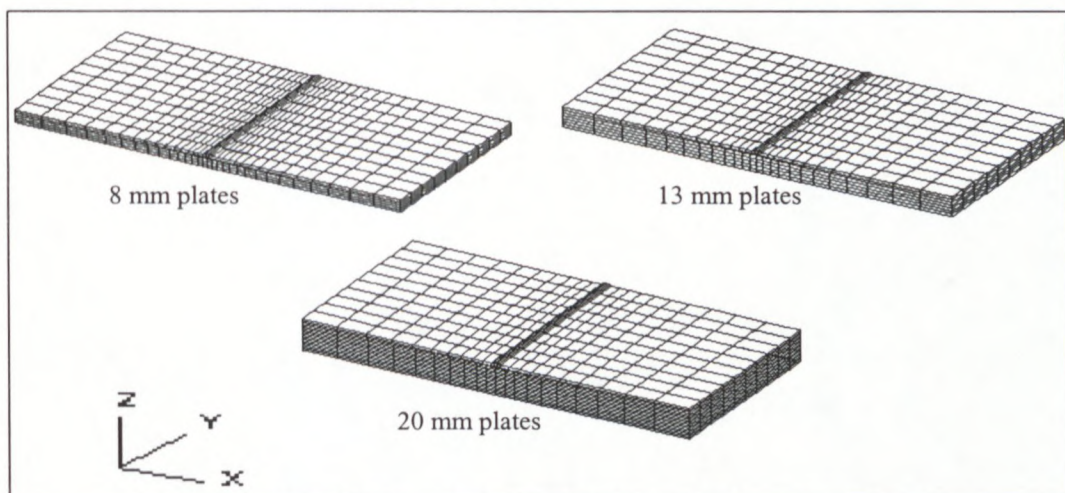


**Figure 6.1** Discretized meshes to be used for the bench mark problem



In all three cases 8 noded brick elements were used to discretize the base plates, while a combination of 8 and 6 noded three-dimensional elements were used to discretize the bead. The meshes were regular, with the highest element densities along the weld line, and increasing uniformly away from the weld line in the x-direction, but constant in the direction where the welding arc is going to be applied.

## 6.2 Computation Assumptions

The main purpose of the welding simulations was to assess global deformation, and stresses in the longitudinal welding direction. Welding computations were carried out in 4 successive steps

- non-linear thermo-metallurgical computation,
- mechanical computation of the steady state,
- transient thermo-metallurgical computation of the cooling of the welded structure,
- mechanical computation of the steady state of the cooling of the welded structure.

The metallurgical phase transformations are “built” into SYSWELD+2, and this makes it possible to calculate thermal and metallurgical histories that are set up in the plates due to the welding process. For the mechanical computations, the effect of metallurgy is taken into account through the volume variations induced by the metallurgical transformations, the behavior law of each metallurgical phase, as well as the transformation plasticity effect. Transformation temperatures during heating will be extracted from the Equilibrium Diagram, while the Continuous Cooling Transformation (CCT) Diagram will be used to extract transformation temperatures during cooling.

The thermal boundary conditions into or out of the body were implemented into SYSWELD+2 using simplified FORTRAN codes (**APPENDICES A.2, A.3 and A.4**). Along with this, FORTRAN codes can also be used to implement various user defined heat fluxes and can be used to define additional metallurgical phase transformations.

Due to the highly transient and non-linear nature of the thermo-metallurgical analysis of the welding process, one of two methods may be used to solve the finite element equations. These methods are known as matrix update or quasi-Newton methods. The methods that were used are the Newton-Raphson and the BFGS (*Broyden-Fletcher-Goldfarb-Shanno*) methods. It was found that the BFGS method was in fact more effective for the solving of the finite element equations. After the linear equations were obtained from the BFGS method, an iterative solving scheme was used to solve these equations. A typical input file used in SYSWELD 2, is given in **APPENDIX A.1**.



## CHAPTER 7

### NUMERICAL RESULTS

---

#### 7.1 Introduction

Many of the operating parameters of TIG welding have a direct effect on the shape and size of resulting Heat Affected Zones. They also have an effect on the resulting residual stress, strain and thermal distortion. During the actual welding only a few of these variables actually change to suit different welding conditions. For this reason it is of great importance that the welding engineer has the ability to identify these parameters as well as the effects they might have on the resulting welded structure. Once this has been achieved, the engineer may proceed to set up a properly planned and controlled application of the welding process.

The welding heat input, directly related to the welding current and voltage, and the arc travel speed are two of these welding parameters. It has been proven that even a slight change of these variables may have a significant effect on the result of welding. Other welding parameters: pre-heating, clamping of welding joints, and grooves also contributing in the quality of welding.

#### 7.2 Influence of welding parameters on HAZ and penetration.

##### 7.2.1 Welding Current

The rate of electrode melting, the depth and width of penetration, and the amount of base metal that is melted during the welding process are related to welding current. If the welding current is too high for the particular welding speed, the depth of penetration is too big and produces an excessively large HAZ and the weld may be melted through the weld joint. In the first case, **Material 1** (see *Table 6.1*) is used in simulations of square butt-welds in carbon steel plates of thickness: 8mm, 13mm, and 20mm. The plates were squares of 100mm by 100mm. The welding voltage and speed remains constant at 22 Volts and 5mm/s respectively, while the welding current varied from 120 to 310 Amperes. The results of these simulations are shown in **Fig. 7.2.1**. An increase in the welding current causes an increase in size of the resulting HAZ.



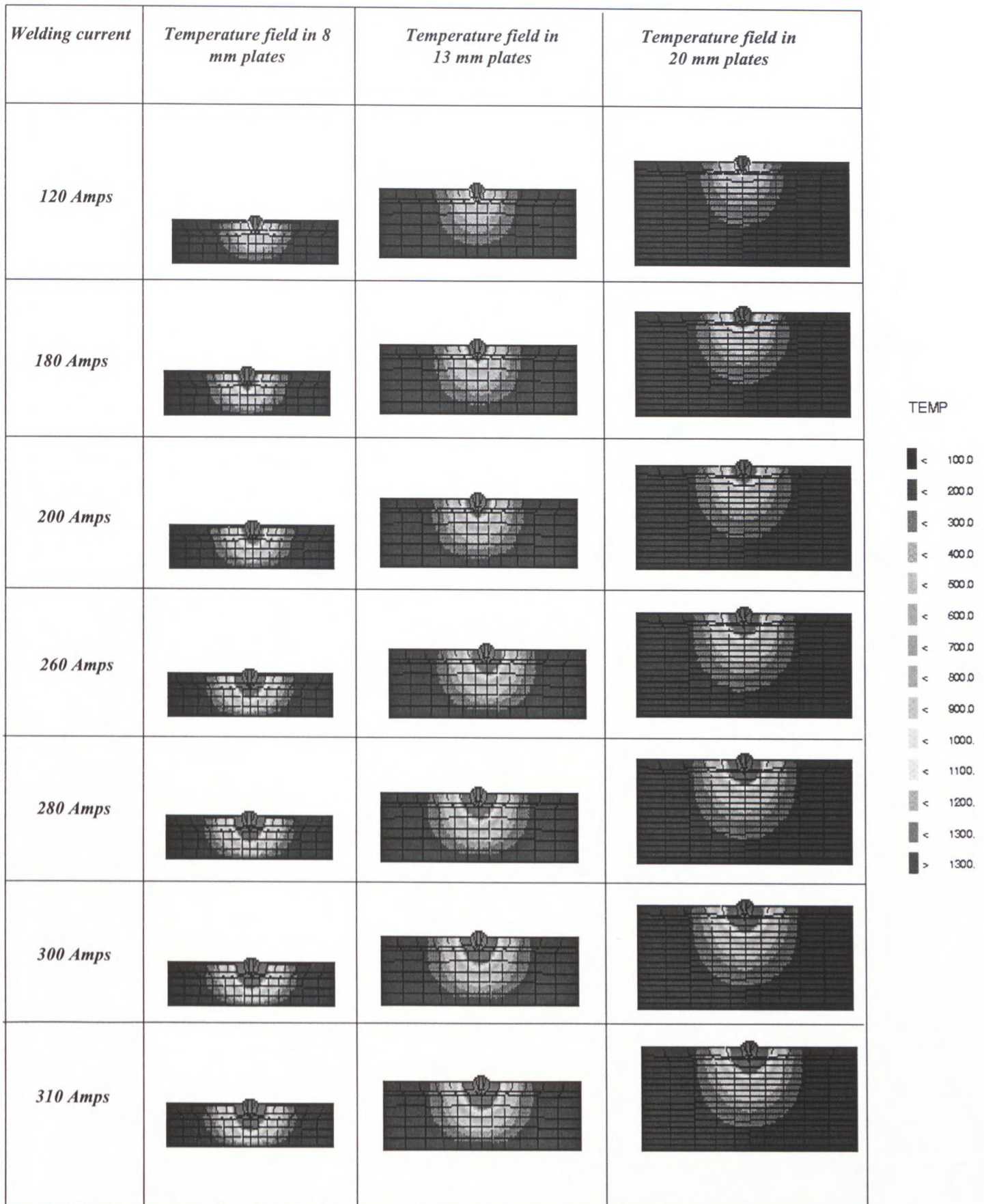
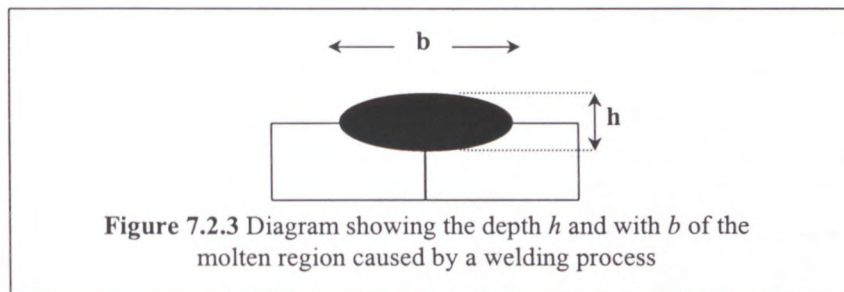


Figure 7.2.1 Heat affected zones caused by variation of TIG welding current on 8mm, 13mm and 20mm plates.



The Equilibrium Diagram shows that the austenitic phase for **Material 1** (referring to **Table 6.1** on page 27) reaches the molten state at temperature  $\pm 1550\text{ C}^0$ . This temperature was achieved for each case of welding current in **Fig. 7.2.1**, and is depicted by the red area. These results are used in metallurgical analysis to determine the amount of liquid austenite (molten material) that was present in a bead and parent plates upon the completion of welding. **Fig. 7.2.2**, shows penetration and HAZ for various currents. These results can be interpreted as the amount of penetration or fusion that is achieved at the end of welding. The austinization is given in terms of fractions from 0 to 1. When the welding current is increased the fraction of liquid austenite or "penetration" is also increased.

Another sensitivity analysis of depth  $h$  and width  $b$  of the resulting molten region subject to variation of welding current is performed using **Material 2** (referring to **Table 6.1** on page 27). **Fig. 7.2.3** illustrates the molten region caused by TIG welding. The welding variables for these simulations can be found in **Table 7.1**.



<i>RUN</i>	<i>WELDING CURRENT</i>	<i>WELDING VOLTAGE</i>	<i>WELDING SPEED</i>
1	120 Amps	24 Volts	5 mm/s
2	150 Amps	24 Volts	5 mm/s
3	180 Amps	24 Volts	5 mm/s

**Table 7.1** Welding variables used for simulations conducted with Material 2

Results of these simulations are shown in **Fig. 7.2.4 (a)** and **(b)** where depth and width of a molten region versus welding current is drawn.

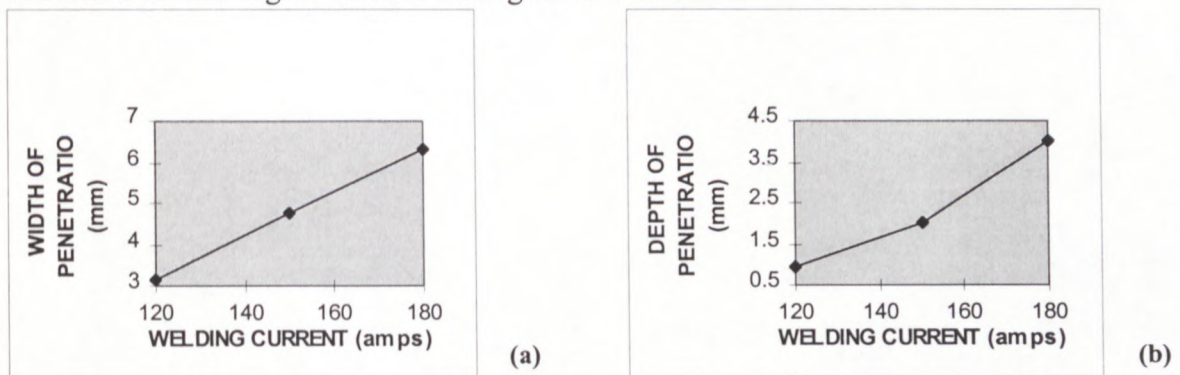


**Figure 7.2.4** Graphical representation of (a) penetration width versus welding current and (b) penetration depth versus welding current.













<i>Welding Current</i>	<i>Heat Affected Zone</i>	<i>Penetration</i>
<i>120 Amps</i>		
<i>180 Amps</i>		
<i>200 Amps</i>		
<i>260 Amps</i>		
<i>280 Amps</i>		

Figure 7.2.2 Heat affected zones with corresponding penetration

These graphs are used to extract two functions that can be used to predict depth and width of penetration in relation to welding current. It should be noted that the welding voltage and speed mentioned (see *Table 7.1*) should remain constant for any values of the welding current. Two functions are proposed

$$\text{Width of penetration} = aI^{b/I}, \quad (7.2.1)$$

$$\text{Depth of penetration} = ab^{(I)}, \quad (7.2.2)$$

where  $a$  and  $b$  are constants and  $I$  is given as the welding current. A forecast of the TIG welding current versus corresponding depth and width of penetration can be evaluated using these functions. *Table 7.2* gives these results.

Current (Amps)	Width of Penetration (mm)	Depth of Penetration (mm)
122	3.2772	0.9818
128	3.5927	1.1385
134	3.9103	1.3202
140	4.2290	1.5308
146	4.5479	1.7751
152	4.8662	2.0583
158	5.1833	2.3867
164	5.4986	2.7676
170	5.8118	3.2092
176	6.1223	3.7212

**Table 7.2** Prediction depth and width of penetration versus current

Two functions were also obtained from graphs in **Fig. 7.2.5 (a)** and **(b)** showing the maximum temperature at the end of welding versus depth  $h$  and width  $b$  of penetration. These functions are

$$\text{Temperature} = c + d [\ln (h)] \text{ and} \quad (7.2.3)$$

$$\text{Temperature} = c + d [\ln (b)], \quad (7.2.4)$$

where  $c$  and  $d$  are parameters. *Table 7.3 (a)* and *(b)* shows the correlation between width  $b$  and temperature, and depth  $h$  and temperature.

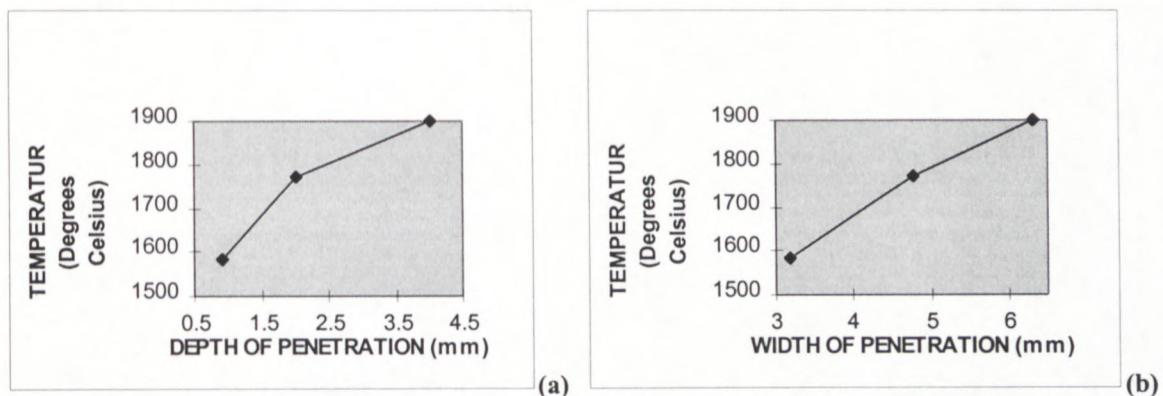


**Figure 7.2.5** Graphical representation of the final temperature achieved at the end of welding versus (a) depth and (b) width of penetration.



Width of penetration (mm)	Temperature ( $^{\circ}\text{C}$ )	Width of penetration (mm)	Temperature ( $^{\circ}\text{C}$ )
3	1558.4	4.65	1759.02
3.15	1580.7	4.8	1773.6
3.3	1602.04	4.95	1778.6
3.45	1622.4	5.1	1801.3
3.6	1641.9	5.25	1814.6
3.75	1660.6	5.4	1827.5
3.9	1678.5	5.55	1840.02
4.05	1695.8	5.7	1852.2
4.2	1712.4	5.85	1864.1
5.35	1728.5	6	1875.7
4.5	1744.02		

**Table 7.3 (a)** Correlation between depth of penetration and temperature

Depth of penetration (mm)	Temperature ( $^{\circ}\text{C}$ )	Depth of penetration (mm)	Temperature ( $^{\circ}\text{C}$ )
0.8	1559.7	3.66	1884.9
1.06	1619.9	3.92	1899.6
1.32	1666.8	4.18	1913.4
1.58	1705.3	4.44	1926.3
1.84	1737.8		
2.1	1766.12		
2.36	1791.1		
2.62	1813.4		
2.88	1833.7		
3.14	1852.2		
3.4	1869.2		

**Table 7.3 (b)** Correlation between width of penetration and temperature

## 7.2.2 Welding Speed

Welding speed is an important welding parameters that governs the production rate and material microstructure, i.e. phase composition of weldment, which determines the quality of welds. When welding speed is too low, the weld joint can cause cracking, excessive melt through and a large weld pool around the welding arc. The disadvantages of these is formation of undesirable metallurgical phases and too large HAZ. High speed, on the other hand, decrease the wetting action, i.e. formation of an inadequate weld pool, and increase the possibility of weak penetration. Plates of 13mm made of **Material 1** are used to study the shape and size of HAZ regions produced by various welding speeds. **Fig. 7.2.6** shows the motion and shapes of HAZ

for three arcs across the 13mm plates as well as the final HAZ upon completion of the welds. The diagrams in **Fig. 7.2.6** show that greater weld pool is produced for slower welding speed. The result of this action causes a larger HAZ.

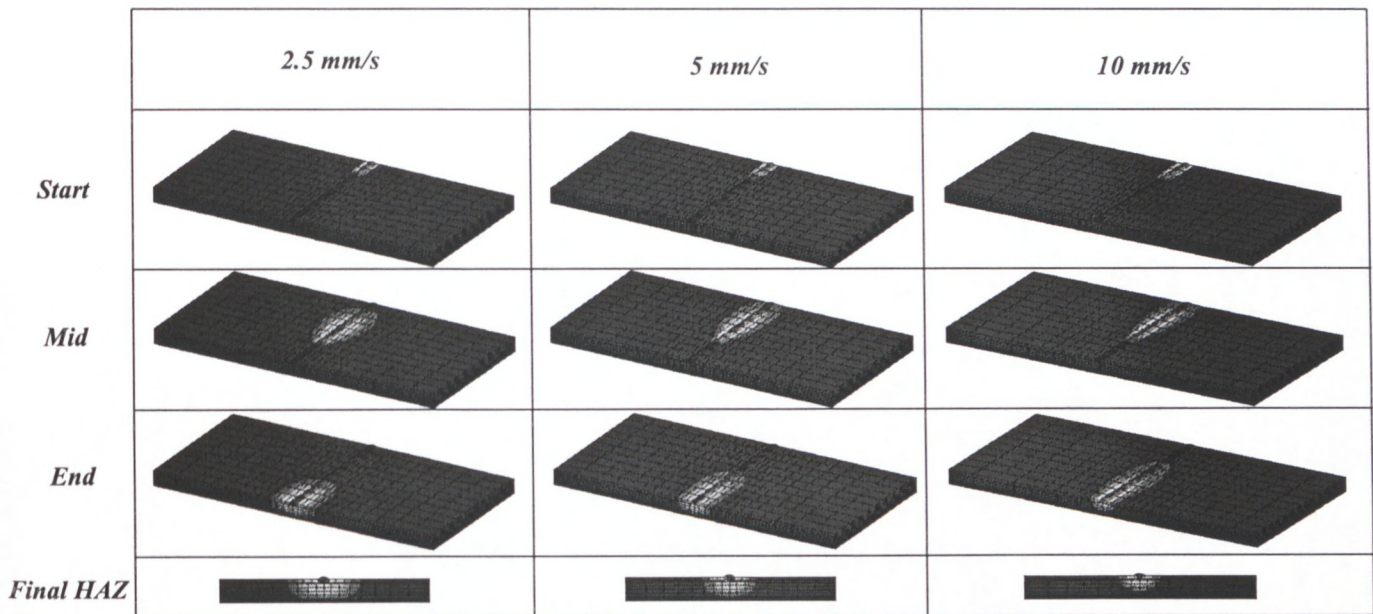
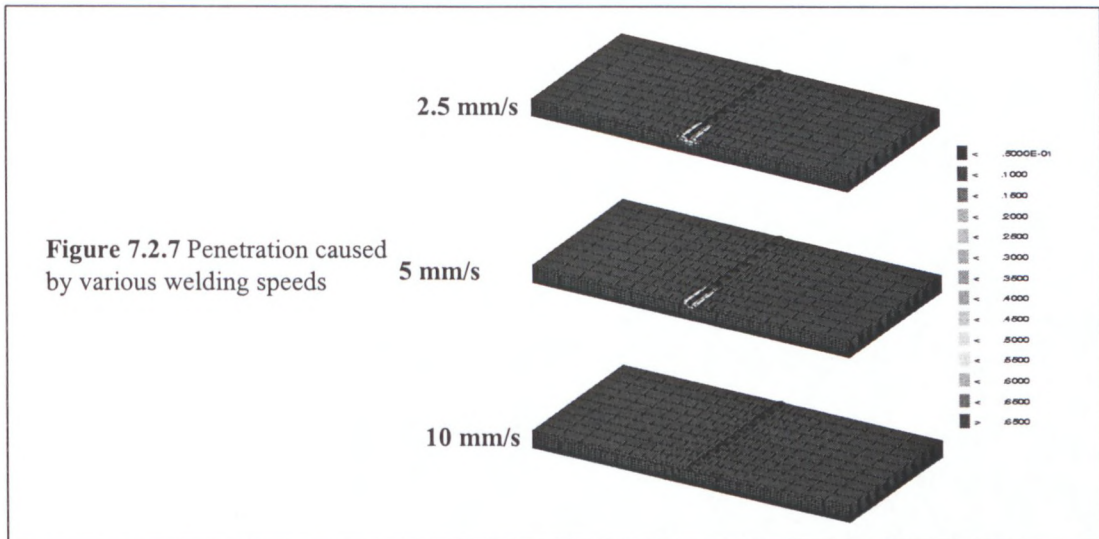


**Figure 7.2.6** Heat affected zones produced by various welding speeds



**Fig. 7.2.7** shows the arc penetration generated with three welding speeds. For **Material 1**, the welding speed of 2.5mm/s caused the most penetration, while the speed of 10mm/s had no penetration.



The **Material 2** is also used to study welding speed influence on depth and width of arc penetrations. Welding operating parameters for these simulations can be found in **Table 7.4**.

The maximum final temperature achieved at the end of welding versus corresponding welding speed is shown in **Fig. 7.2.8**.

<i>RUN</i>	<i>WELDING CURRENT</i>	<i>WELDING VOLTAGE</i>	<i>WELDING SPEED</i>
1	150 Amps	24 Volts	2.5mm/s
2	150 Amps	24 Volts	5mm/s
3	150 Amps	24 Volts	7.5mm/s

**Table 7.4** Welding operating parameters used in sensitivity analysis of welding speed for Material 2

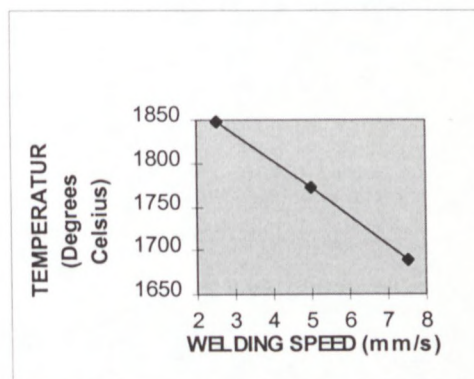


**Figure 7.2.8** Temperature achieved upon completion of welding versus welding speed.

From the graph in **Fig. 7.2.8**, the relation between the final maximum temperature and corresponding welding speed can be written in the form

$$\text{Temperature} = e + f^s, \quad (7.2.5)$$

where  $e$  and  $f$  are function parameters and  $s$  is a welding speed. The correlation between welding speed and temperature, evaluated following Eq.(7.2.5), can be seen in **Table 7.5**. Combining these data with results in **Table 7.3 (a)** and **(b)**, the depth and width of penetration can be evaluated in respect of welding speed.



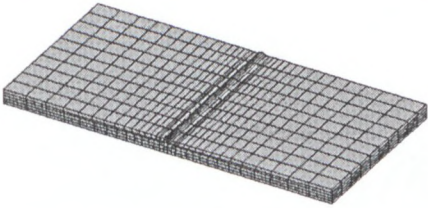
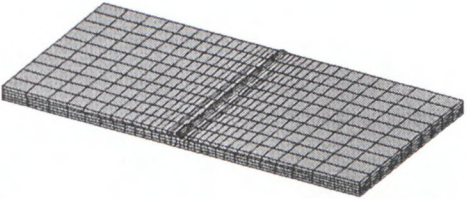


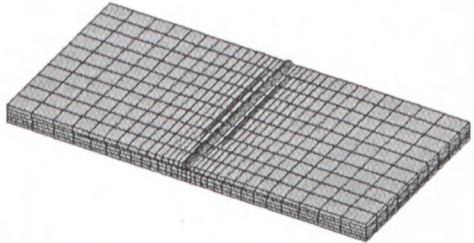
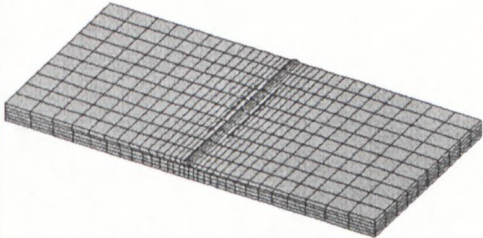
WELDING SPEED (mm/s)	TEMPERATURE (°C)
2.35	1853.53
2.8	1839.23
3.25	1824.93
3.7	1810.62
4.15	1796.32
4.6	1782.02
5.05	1767.72
5.5	1753.42
5.95	1739.12
6.4	1724.82
6.85	1710.52
7.3	1696.22

**Table 7.5** Prediction of welding speed versus temperature

### 7.2.3 Pre-heating of parent material

Pre-heating of parent plates generally helps in achieving smoother temperature distribution during welding and reduces formation of undesirable metallurgical phases, e.g. martensite. **Fig. 7.2.9** shows the final HAZ in two plates of **Material 1**. One of them is welded at environmental temperature 22°C and the other at a pre-heating temperature 90 C°. The figure shows also the difference in the amount of penetration and martensite fraction formed due to pre-heating of one plate only upon completion of the welds. The heat input determined by 120 amps and 24 volts and welding speed of 5mm/s remains constant for both simulations. **Fig. 7.2.9** shows a decrease of martensite fraction in pre-heated plate where temperature distribution is smoother.



	Weld performed at room temperature (22°C)	Weld performed at pre-heat temperature (90°C)
HAZ Regions upon completion of welds		
Initial Material Percentage		
Penetration (Austenite Regions)		
Martensetic Regions		

**Figure 7.2.9** HAZ, martensitic fraction, penetration, and initial material fractions achieved due to welding plates with and without pre-heating

### 7.3 The effects of welding parameters on residual stress and deformation.

#### 7.3.1 Thermal Stresses During Welding

The bead and plates are heated locally by the welding heat source and temperature field is not uniform and changes as welding is progressing. Shrinkage and expansion are producing complex transient stress in the bead and surrounding regions. Stresses produced by welding of thick plates are significant and can be split into the parallel and transverse components regarding the welding direction. They are called longitudinal and transversal stresses, respectively.

#### 7.3.2 Stress Distribution in a Welded Plate

**Fig. 7.3.1** shows stress contours at the end of TIG welding, when the front of welding bath reaches the plate side *O-O*. Welding is performed on 8mm plates made of **Material 2**. The scheme of plate clamping is also shown in this figure.

Welding operating parameters are: Current = 150A; Voltage = 22V, speed of arc is 5mm/s (Run 2 on page 30). Plastic deformations occur along the bead and neighboring zones mostly imbedded in HAZ. Elastic deformations occur outside of these regions.

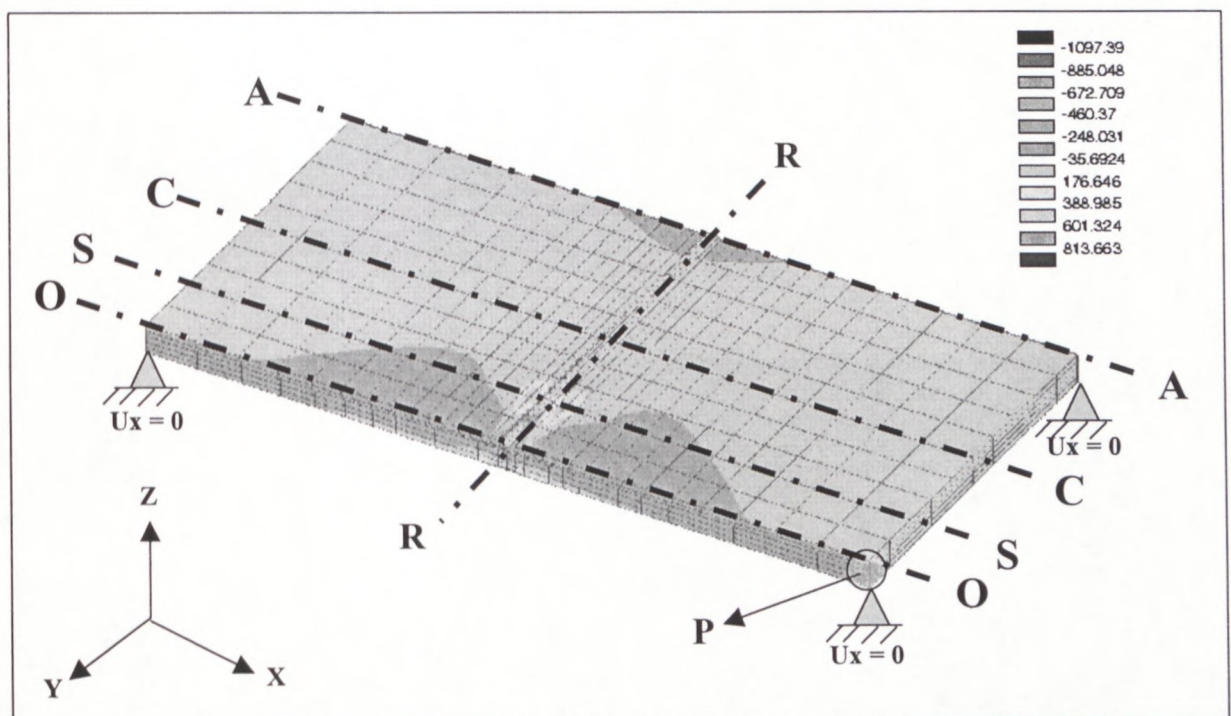


**Figure 7.3.1** Stress contours in X-X plane caused by the welding process.



**Figs. 7.3.2 (a)-(d)** show the changes of the temperature field at the end of welding when the weld-pool reaches the front side of a weld joint. The temperature field is represented by temperature on the top surface of weld-joint along several transversal sections. All temperature curves are steep and narrow.

**Figs. 7.3.3 (a)-(d)** illustrates stresses occurring during welding in transversal sections of the bead and the parent plates.

TEMPERATURE ( $^{\circ}\text{C}$ )

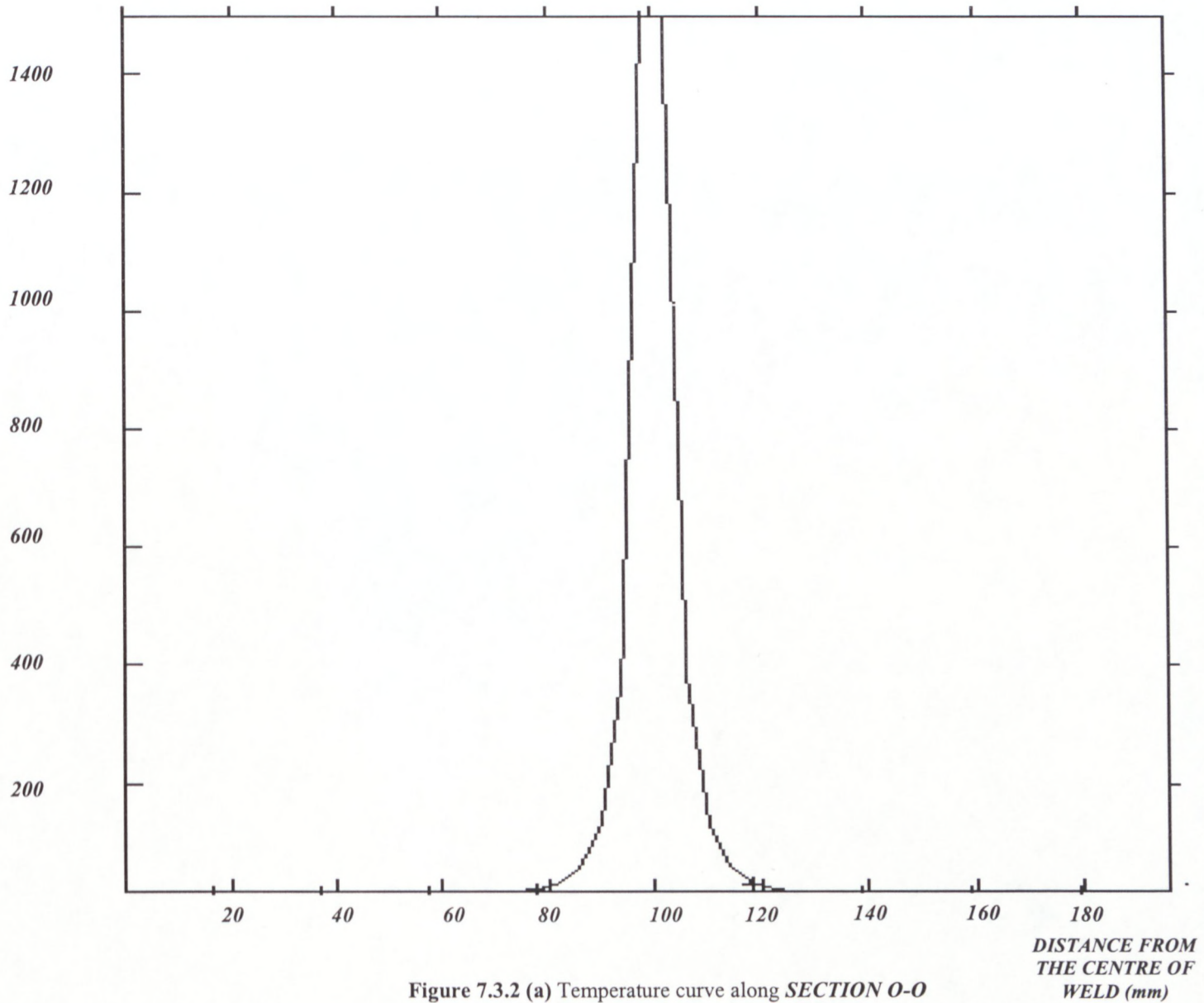


Figure 7.3.2 (a) Temperature curve along SECTION O-O

TEMPERATURE ( $^{\circ}\text{C}$ )

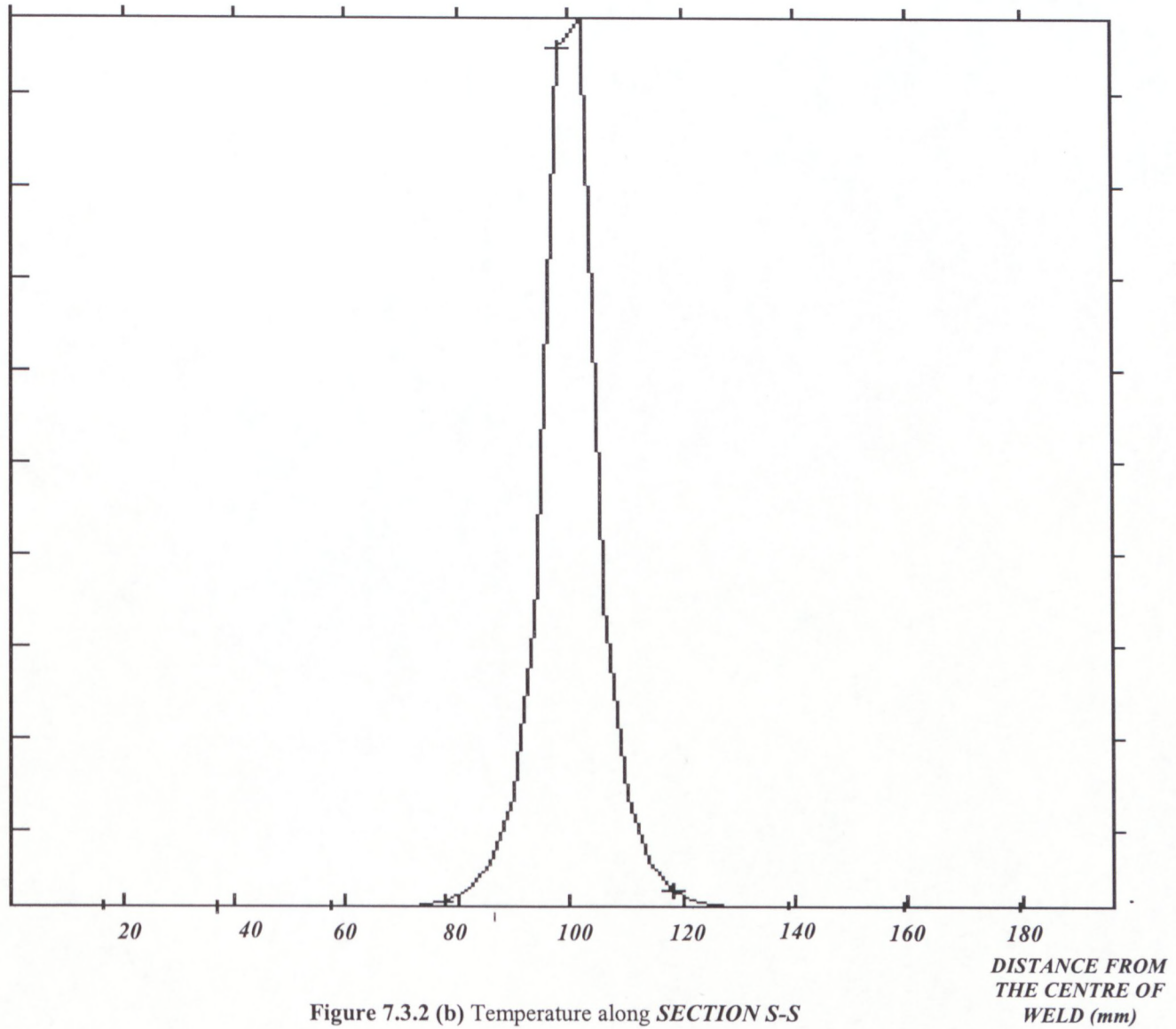


Figure 7.3.2 (b) Temperature along *SECTION S-S*



TEMPERATURE ( $^{\circ}\text{C}$ )

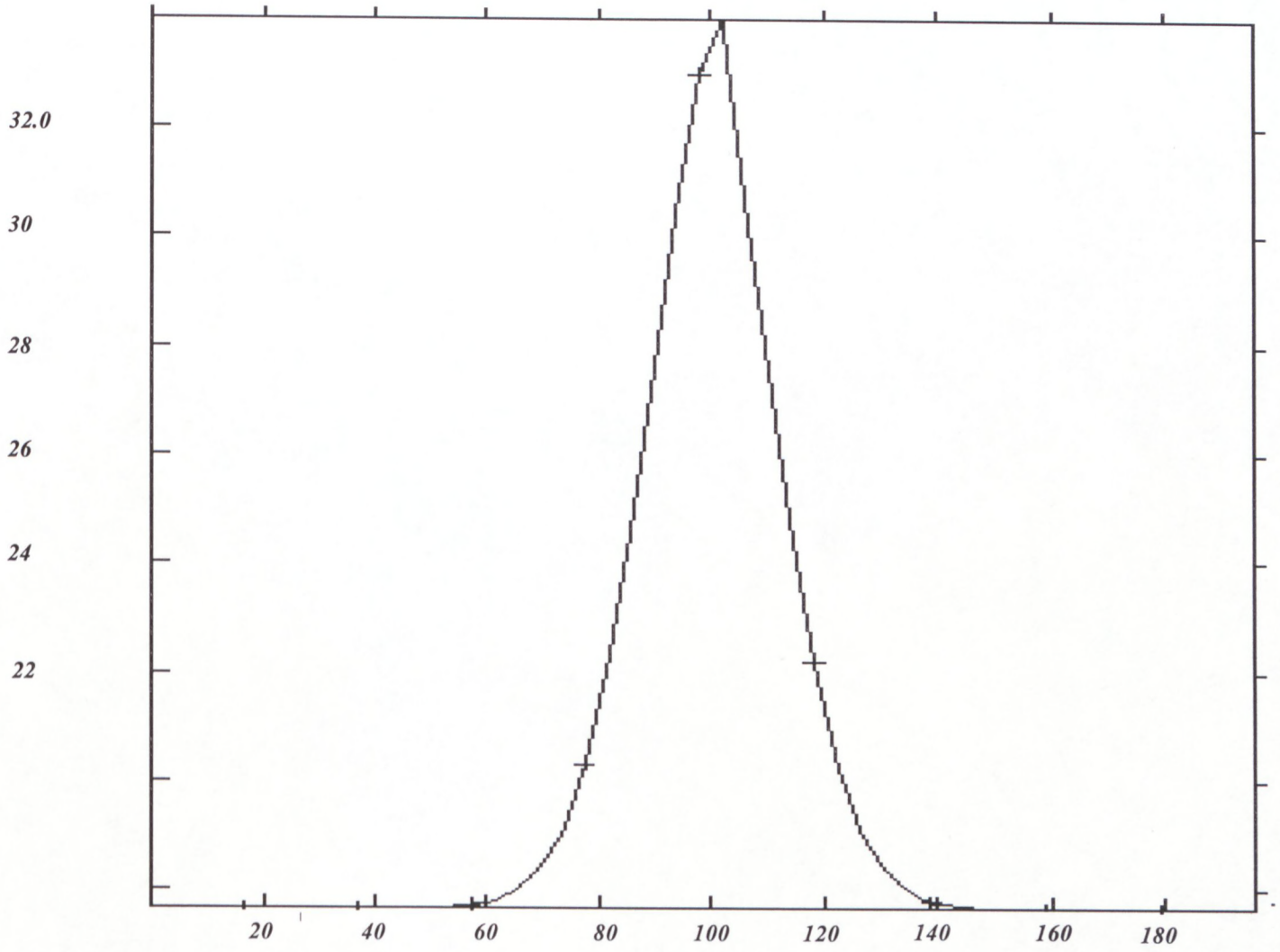


Figure 7.3.2 (c) Temperature along SECTION C-C

DISTANCE FROM THE CENTRE OF WELD (mm)

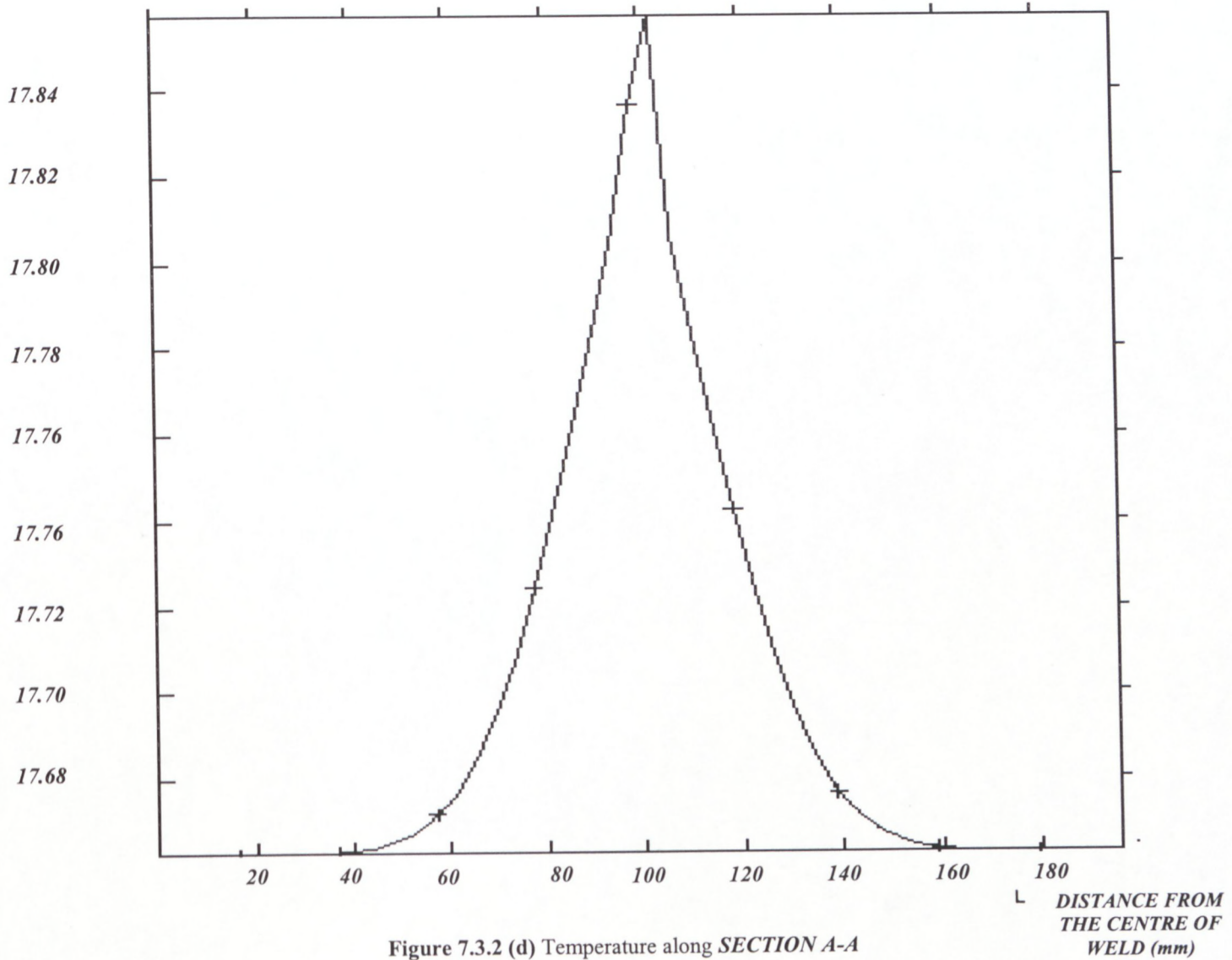
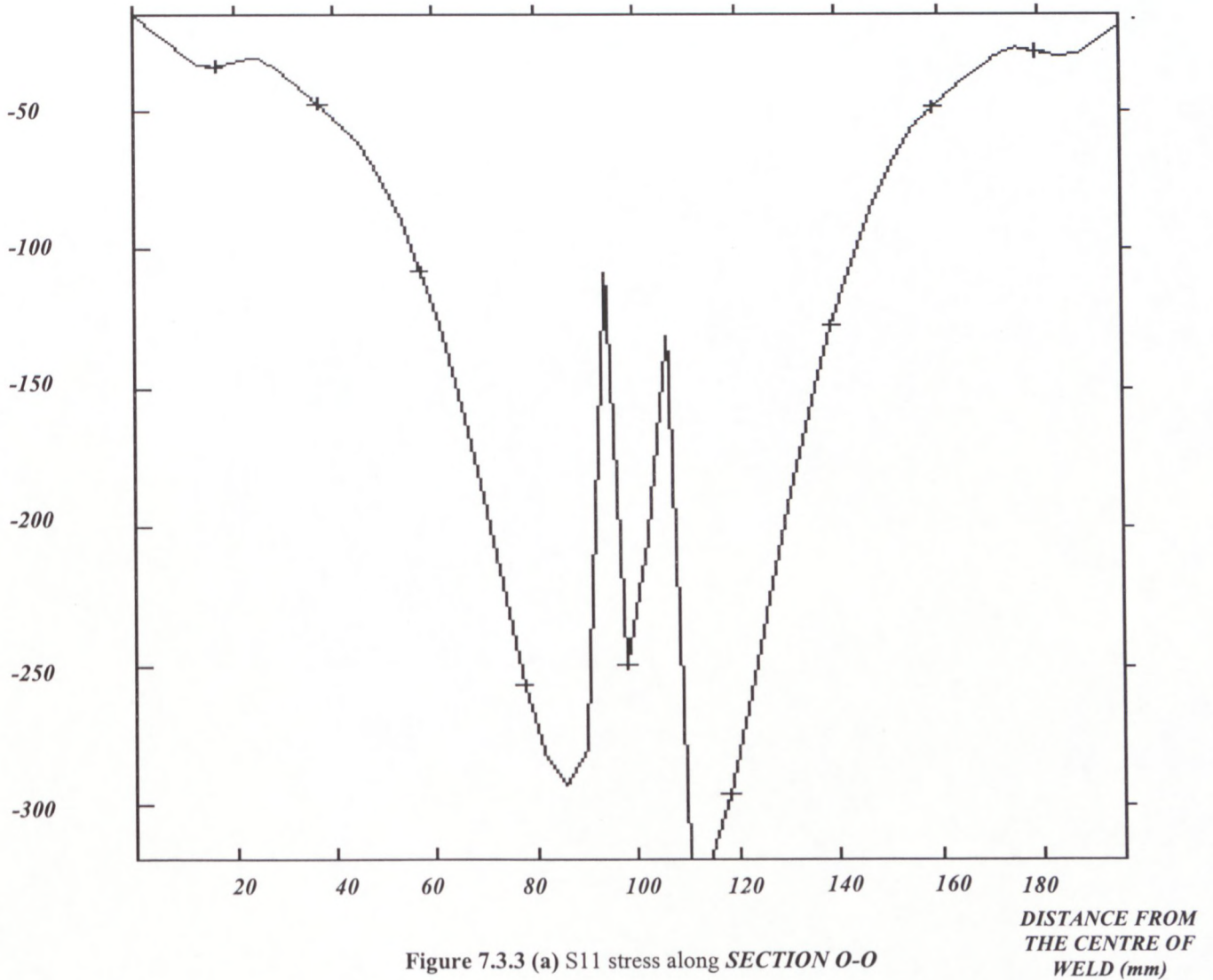
TEMPERATURE ( $^{\circ}\text{C}$ )

Figure 7.3.2 (d) Temperature along SECTION A-A



Due to clamping, shown **Fig. 7.3.1**, the greatest residual stresses occur in parent plates and the bead in the X-direction. **Figs. 7.3.3 (a)-(d)** show stresses along transversal sections. In the **Section O-O**, the material is expanding and only compressive stresses are produced. In the **Section S-S**, the region with tension stress appears in the central part of a weld-joint and is surrounded by regions with compressive stresses. In the **Section C-C** the material is in a state of tension. This is due to the fact that interaction of HAZ, sticking to the front side of a joint, with a cooler part of a joint is generating the tension around area with compressive stresses.

STRESS (MPa)



STRESS (MPa)

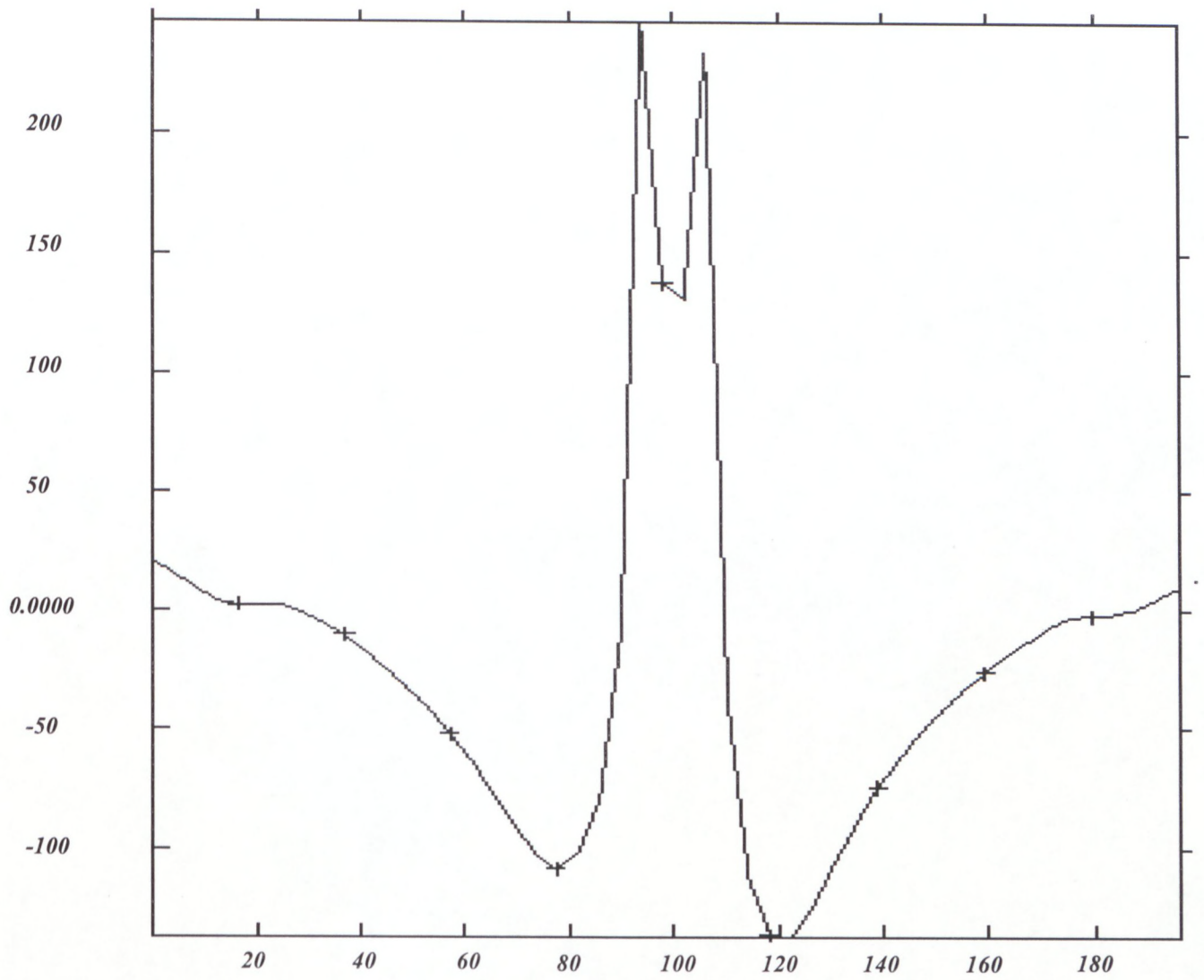
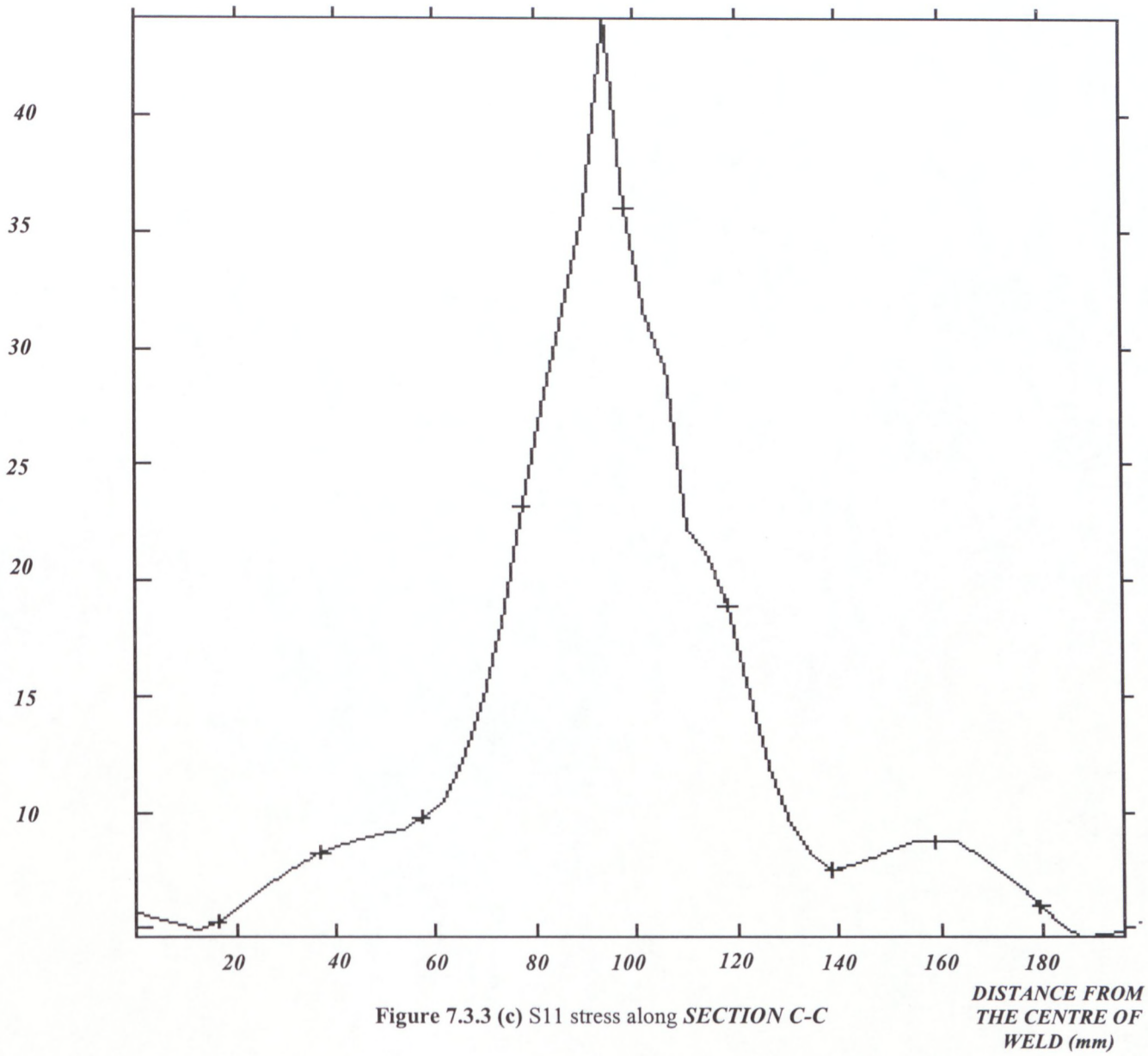
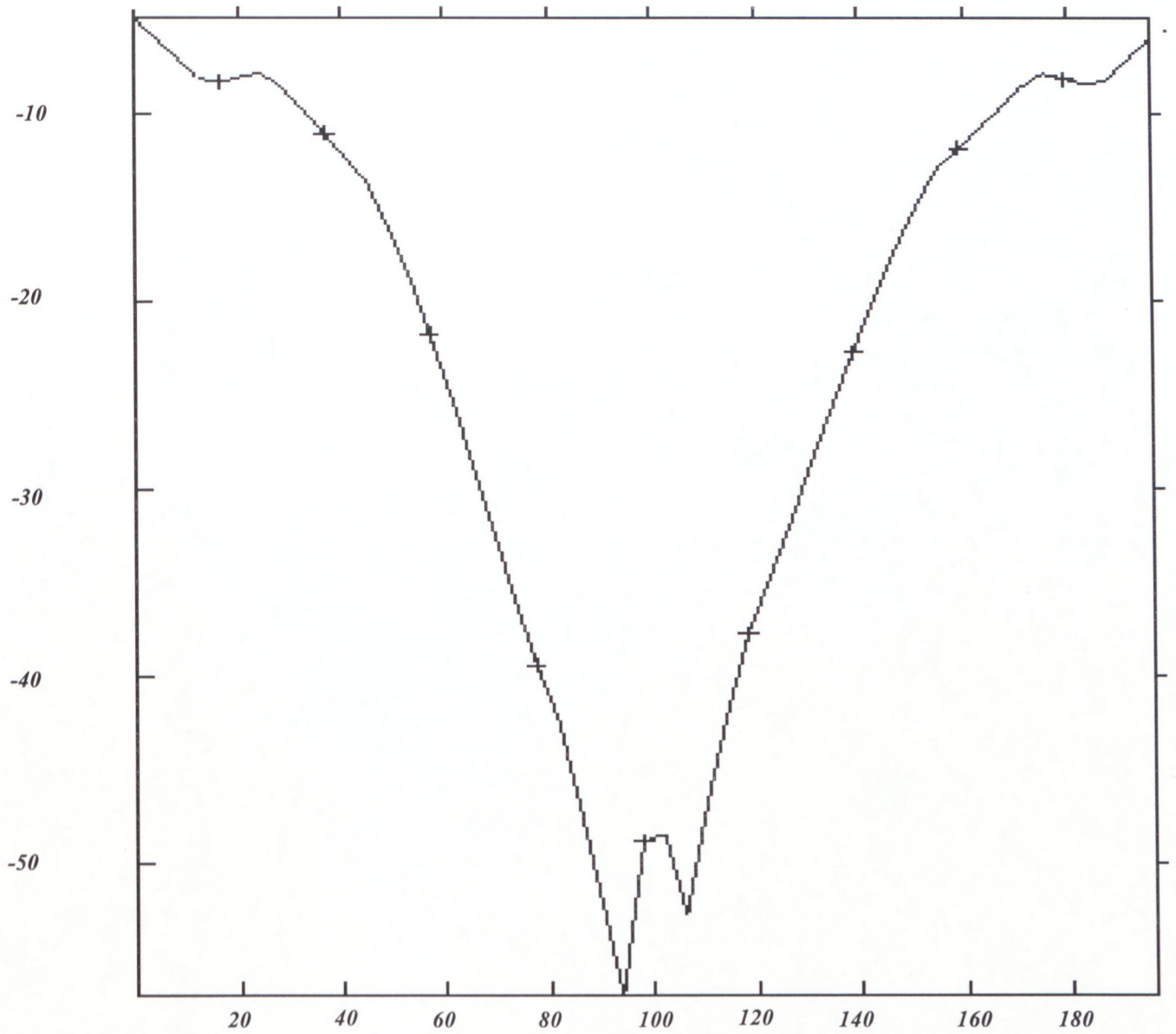


Figure 7.3.3 (b) S11 stress along SECTION S-S

DISTANCE FROM  
THE CENTRE OF  
WELD (mm)



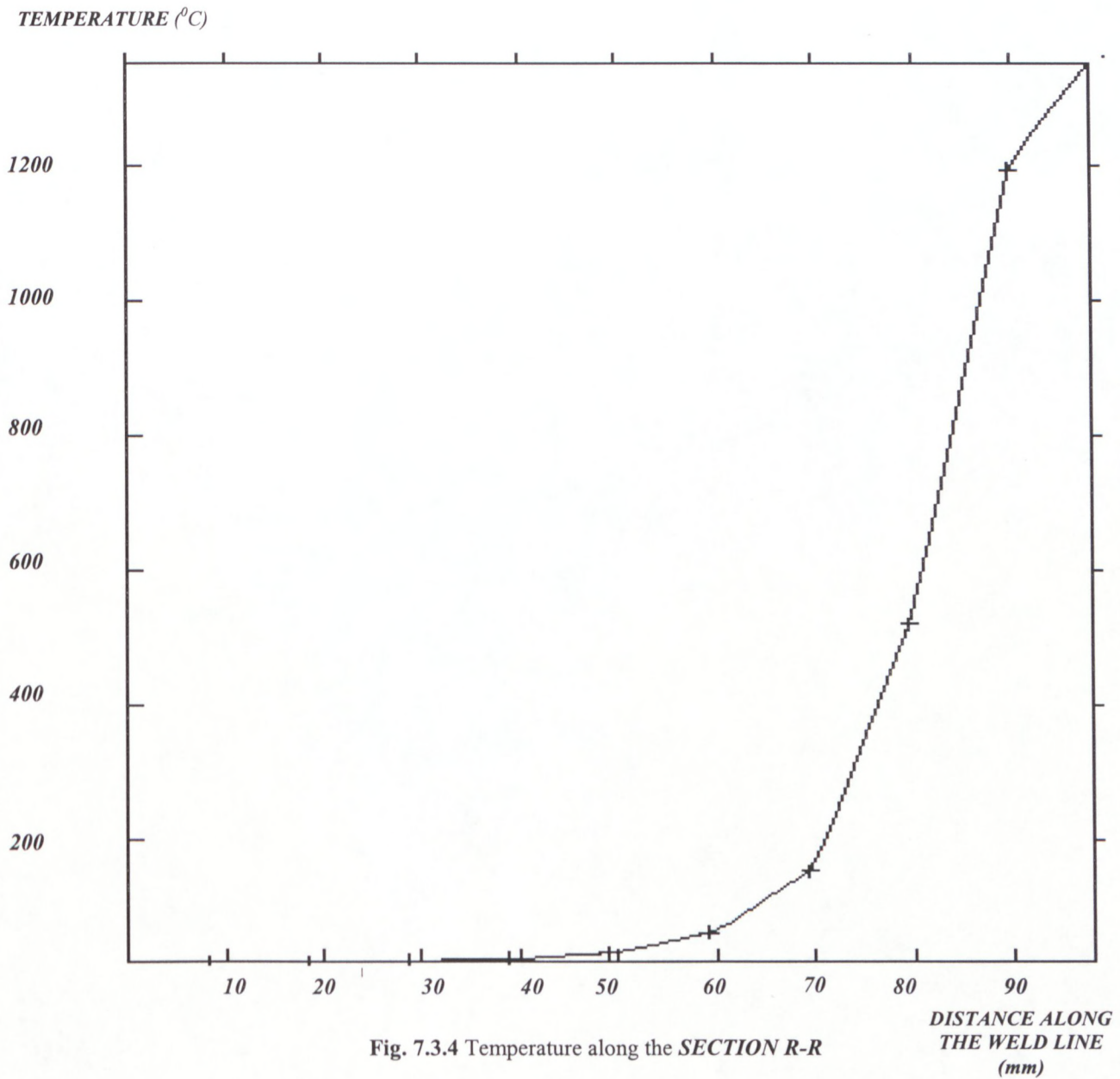
*STRESS (MPa)*Figure 7.3.3 (c) S11 stress along *SECTION C-C**DISTANCE FROM  
THE CENTRE OF  
WELD (mm)*

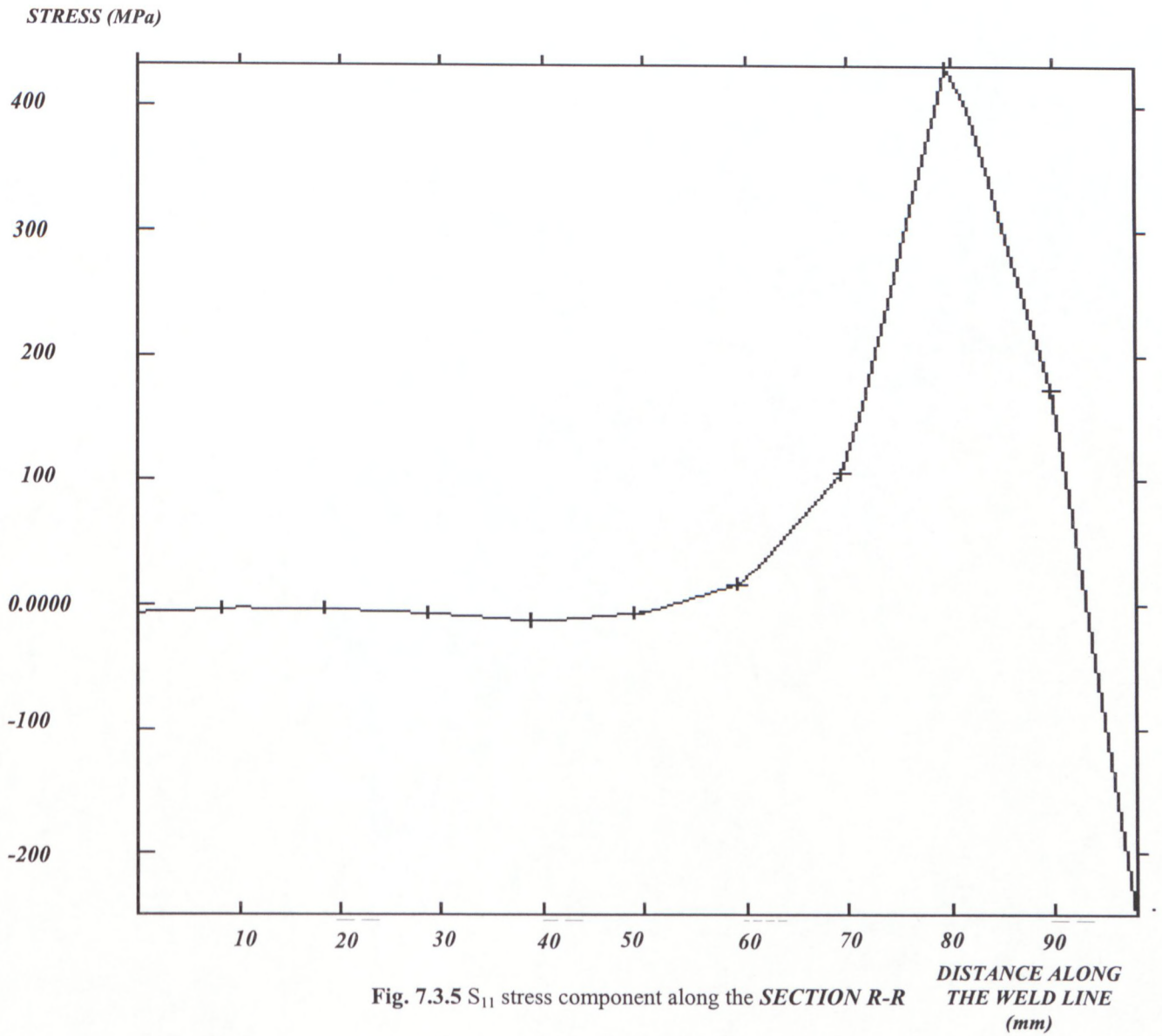
*STRESS (MPa)*Figure 7.3.3 (d) S11 stress along *SECTION A-A**DISTANCE FROM  
THE CENTRE OF  
WELD (mm)*



Temperature along the bead in the *Section R-R* is shown in **Fig. 7.3.4**.

The stress along the *Section R-R* parallel to the weld line is shown in **Fig. 7.3.5**. The longitudinal stresses along the weld line are compressive and close to zero in a cool region and tensile in HAZ.

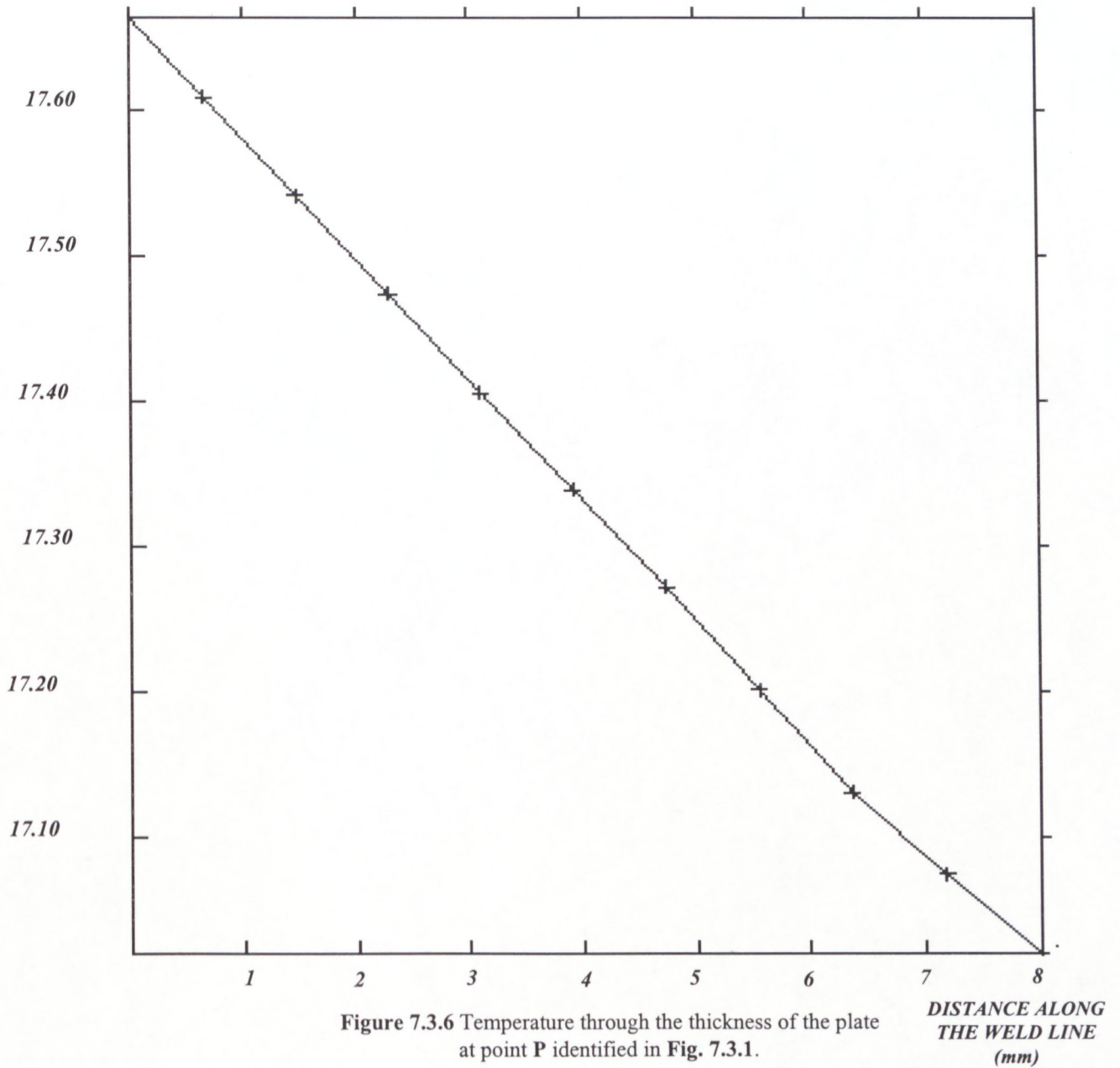


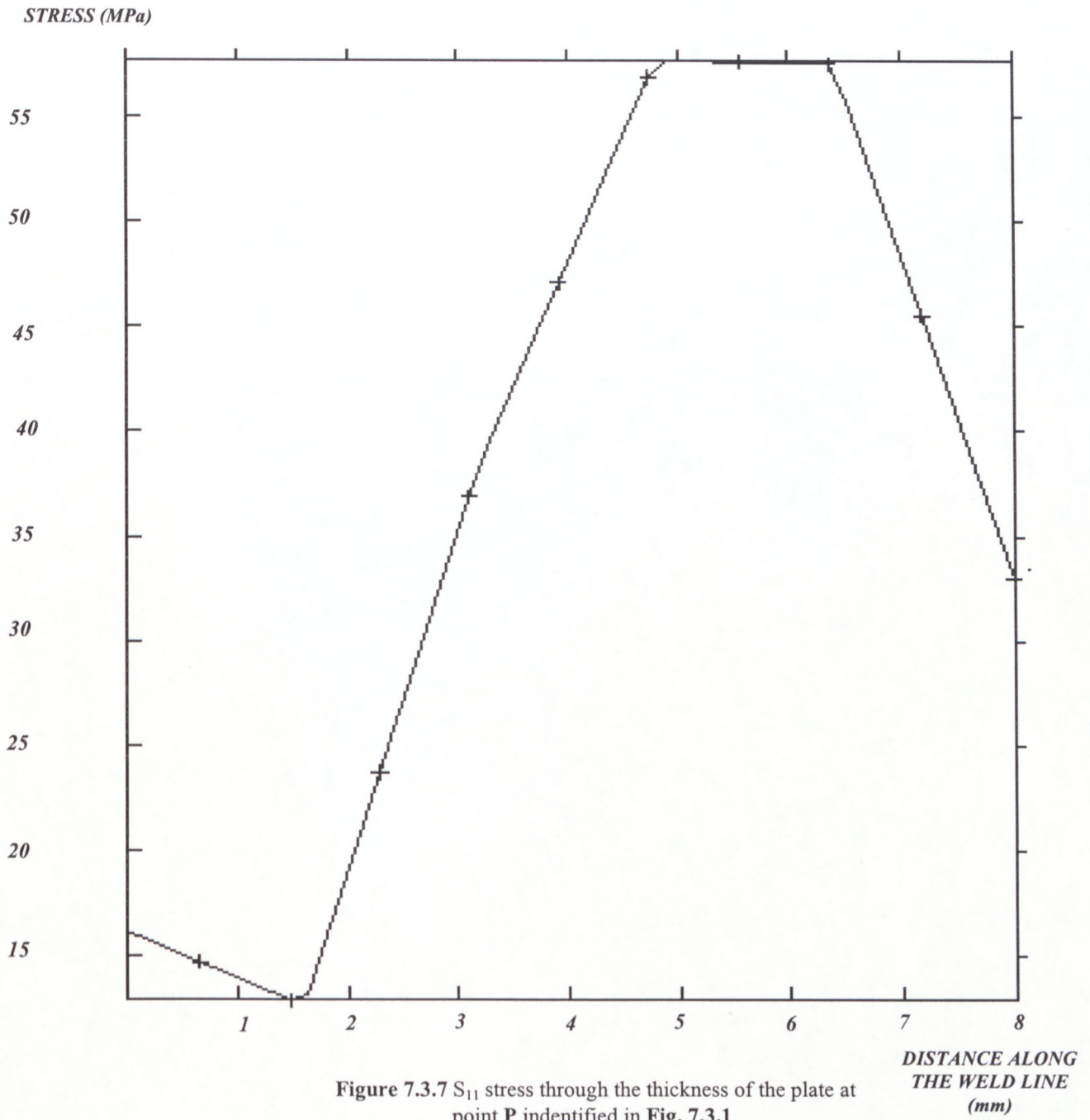




**Fig. 7.3.6** shows the temperature and **Fig. 7.3.7** illustrates stress distributions through the thickness of welded parent plate at point **P** identified in **Fig. 7.3.1**. The stress in this section of the plate is predominantly tensile because of the free end of the plate where a material point can move in the X-direction, while the bottom surface of the plate is fixed.

TEMPERATURE ( $^{\circ}\text{C}$ )







### 7.3.3 Thermal distortion caused by TIG welding

Distortions in welded components are produced by

- transverse shrinkage or expansion in the perpendicular direction regarding the weld line,
- longitudinal shrinkage or expansion parallel to the welding line,
- rotations around the weld line.

These dimensional changes can be seen in **Fig. 7.3.6**.

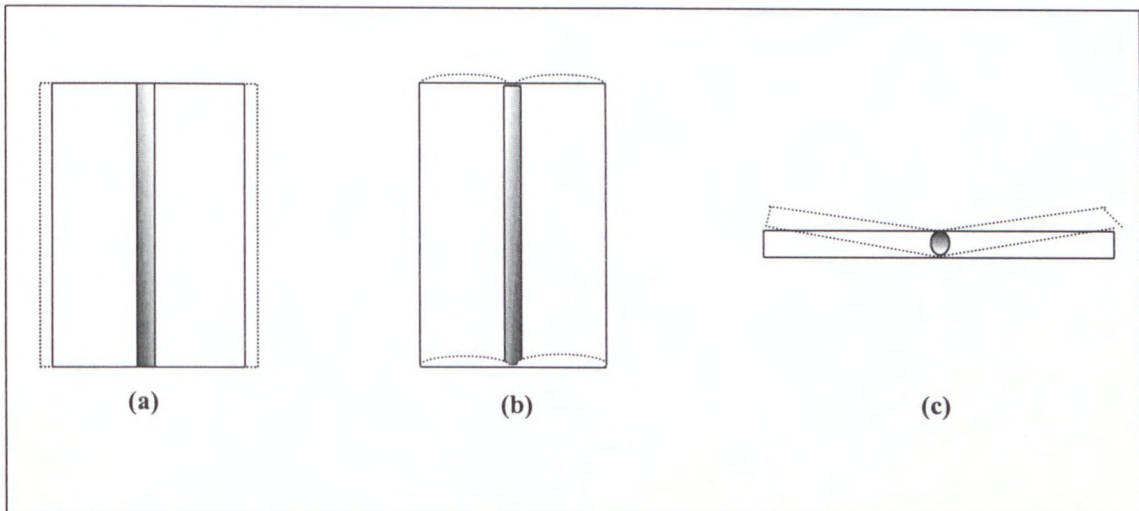


**Figure 7.3.6** Welding distortions: (a) transverse shrinkage (b) longitudinal shrinkage, (c) angular change in a butt weld. *Source: Welding Research Council*

In manufacturing these dimensional changes (**Fig. 7.3.6**) are more complex and usually occur simultaneously. The distortion can be seen in **Fig. 7.3.7** and **7.3.8**. It shows various views of deformation and displacement contours at the end of welding. **Fig. 7.3.9** shows the residual distortion after cooling of a joint. Deformations shown in these figures are amplified fifty times.

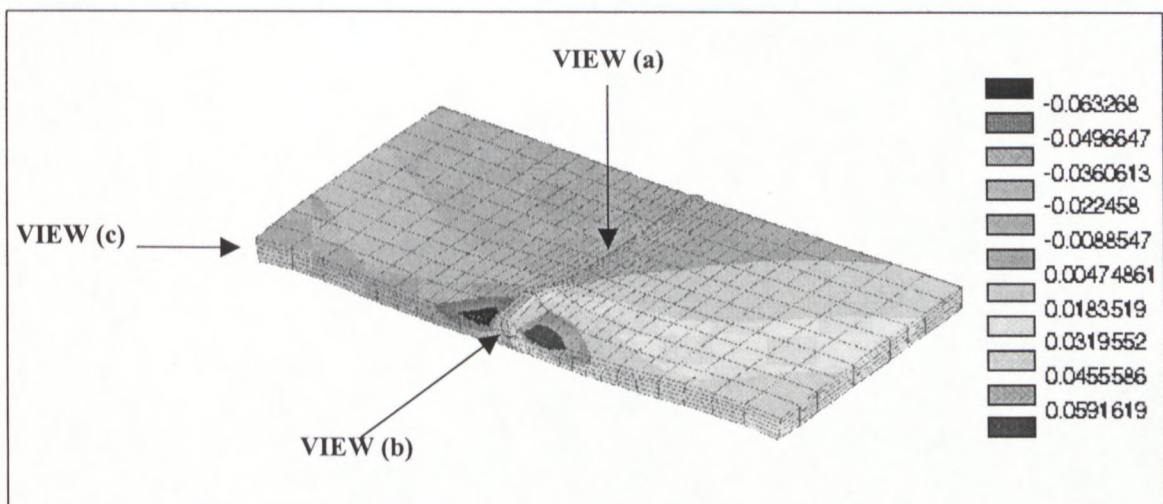


**Figure 7.3.7** Displacement and distortion in the X-X direction

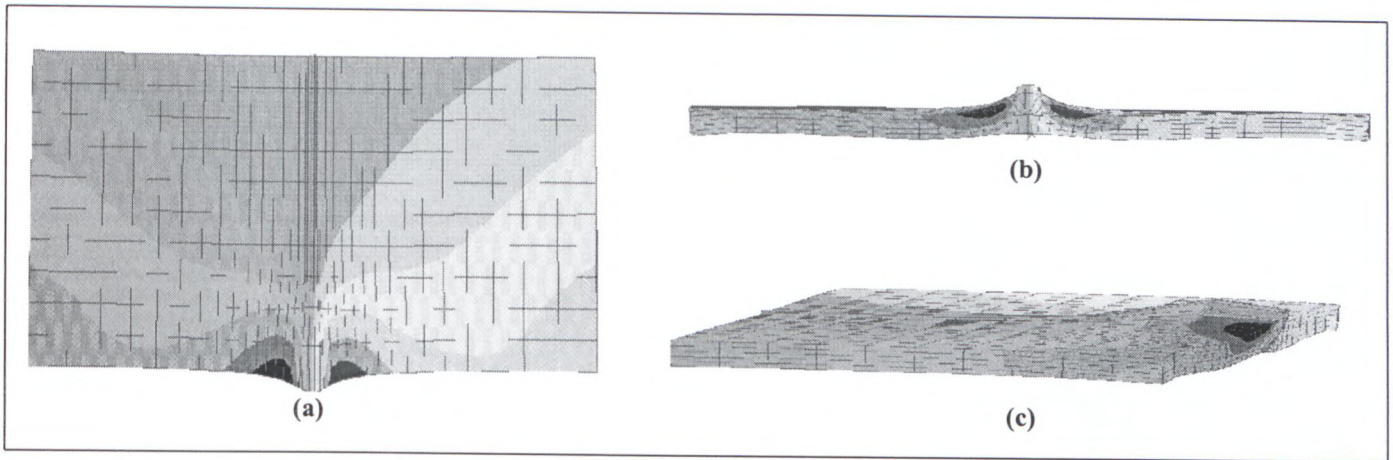


**Figure 7.3.8** Various views of deformation in the X-X direction and longitudinal, transverse and angular components of distortion

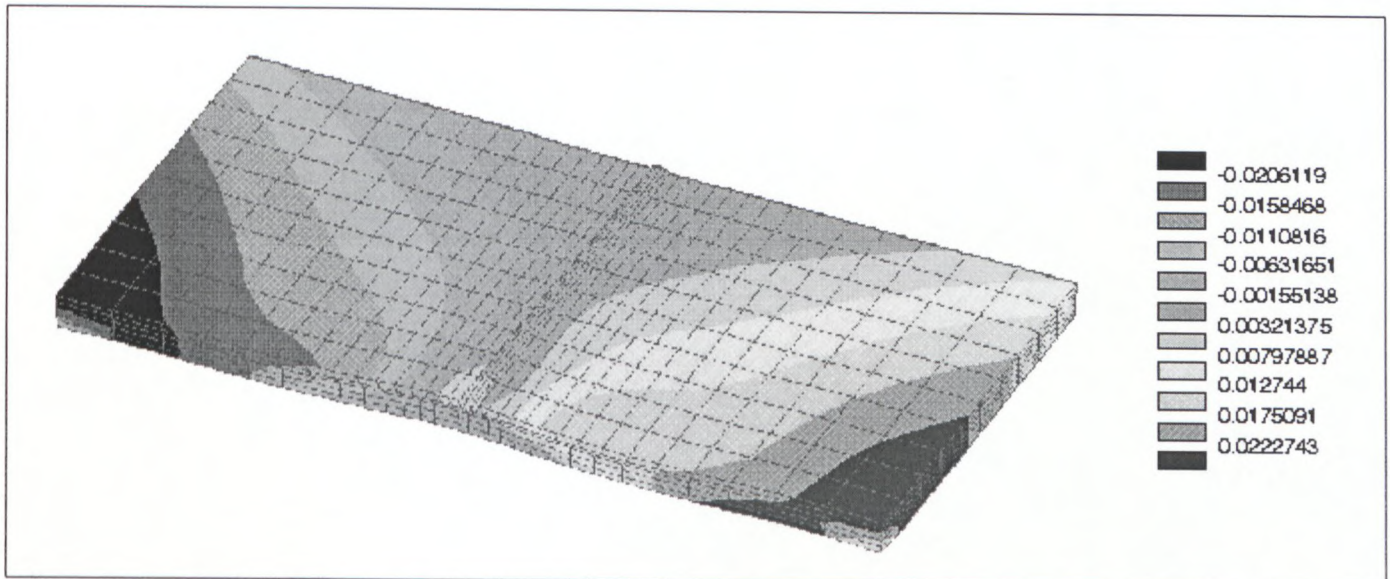


**Figure 7.3.9** Residual displacement and distortion in the X-X direction

**Figs. 7.3.10 (a), (b), and (c)** show the displacements in the X-X, Y-Y and Z-Z planes corresponding to *sections A-A, C-C* and *O-O* of **Fig. 7.3.1**. Along the *Section A-A*, the warpage of the plate is observed. This warpage amplifies near the arc due to high temperature of this area.

Results presented here well correspond with those described in [21].



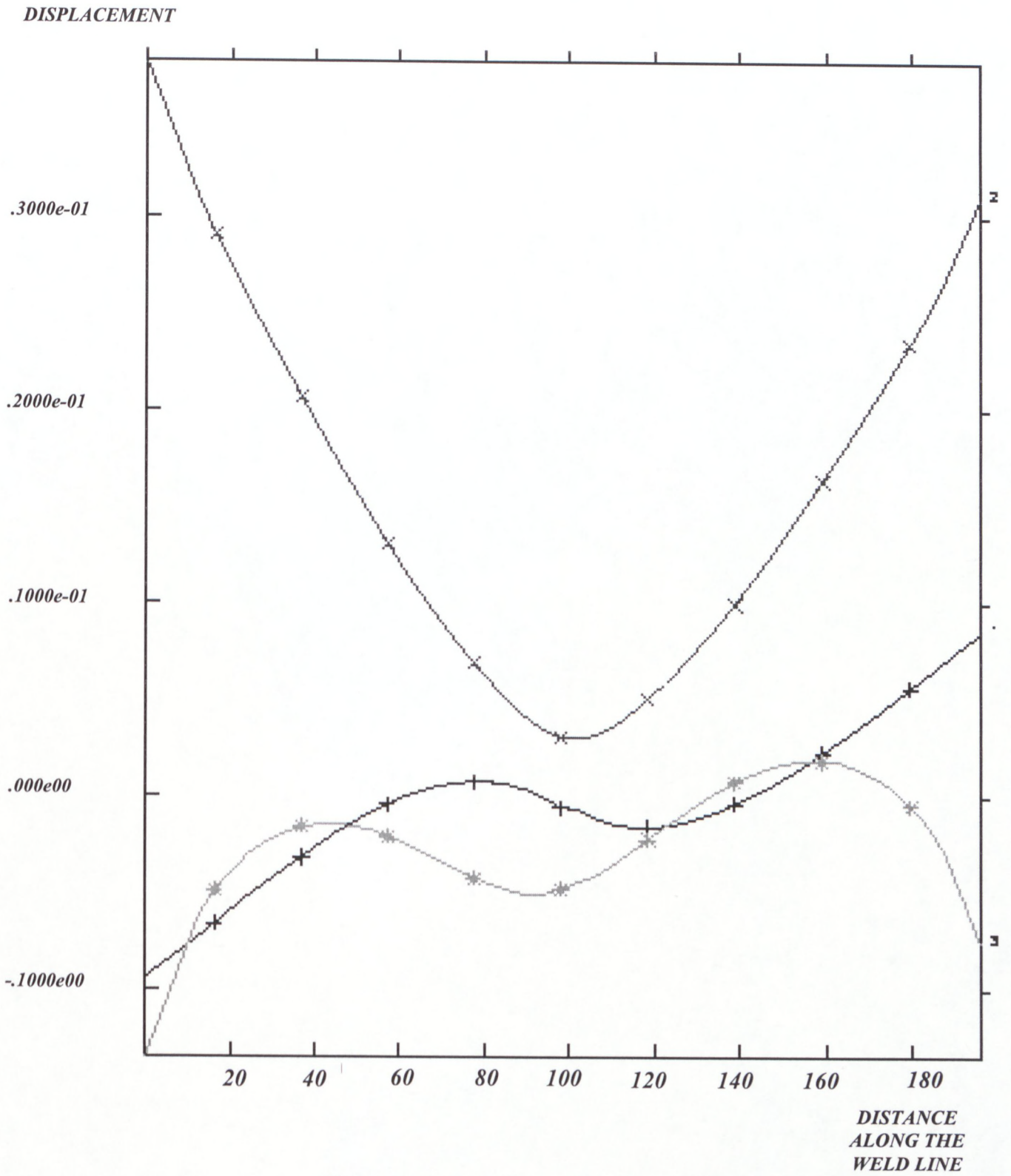


Figure 7.3.12 (a) Displacements along SECTION A-A

DISPLACEMENT

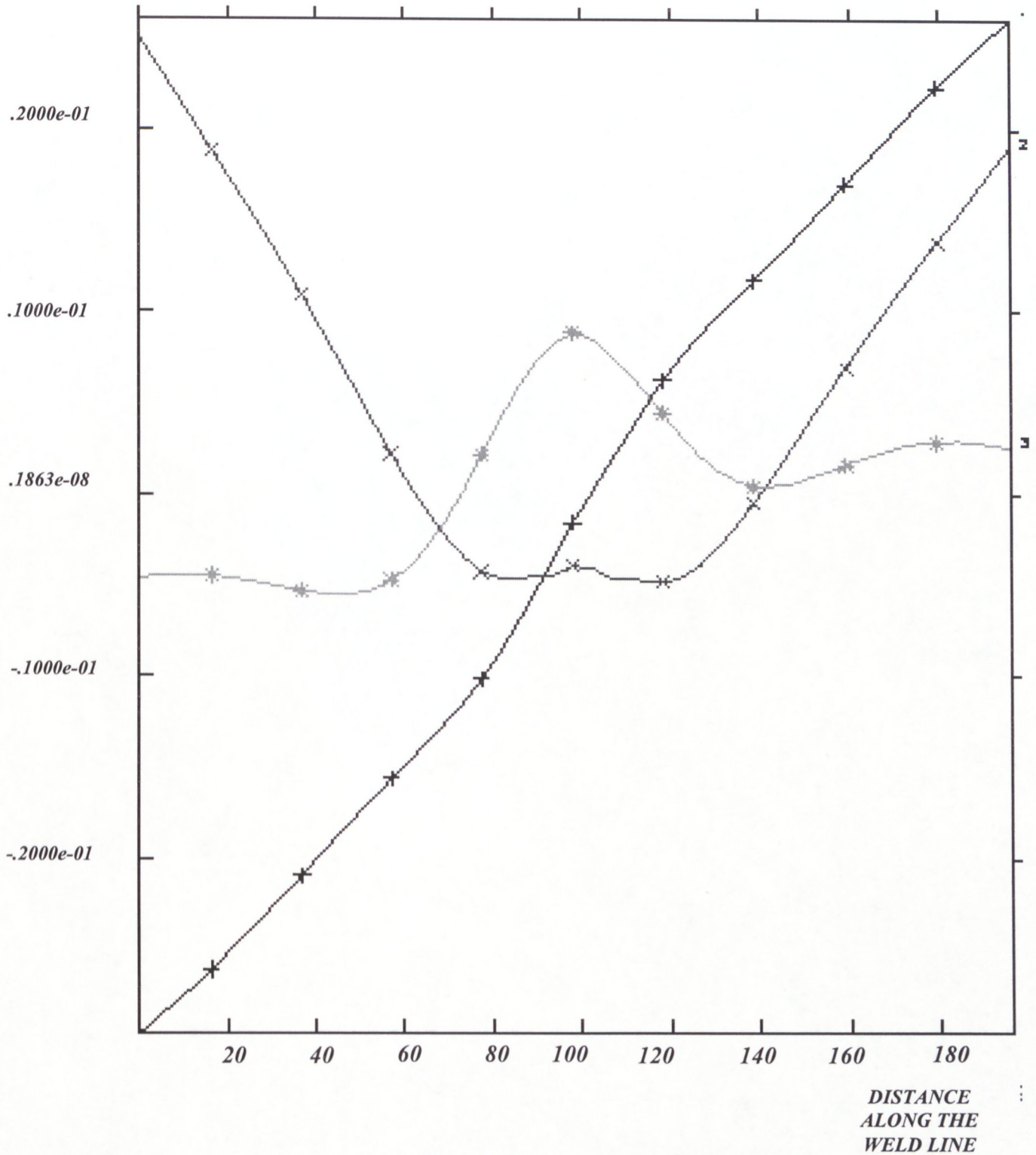


Figure 7.3.12 (b) Displacement along SECTION C-C



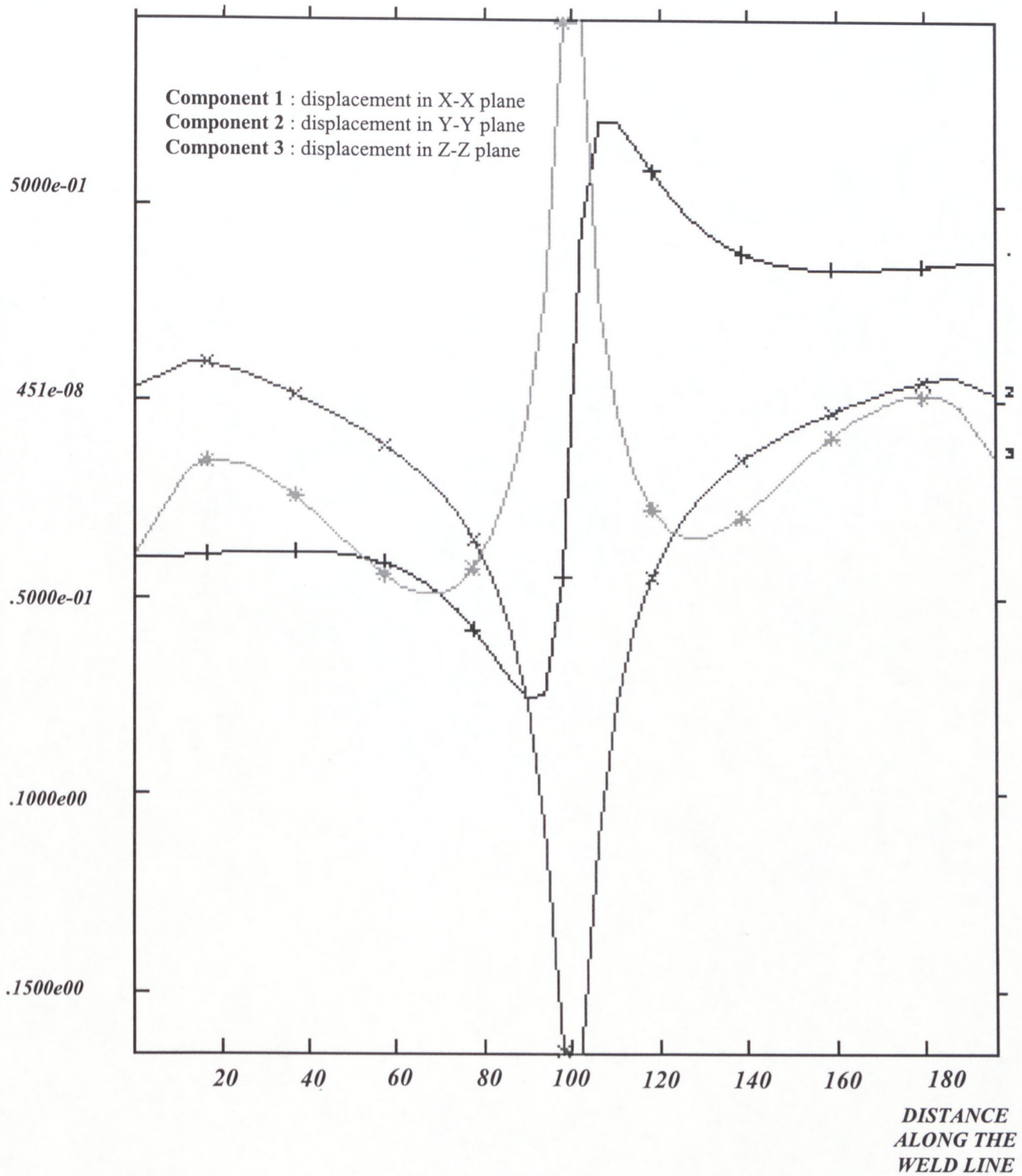
**DISPLACEMENT**

Figure 7.3.12 (c) Displacement along SECTION O-O

### 7.3.4 Influence of heat input on residual stress

An increase of welding current results in the increase of temperature as well as a change in the shape and size of resulting HAZ. Results of thermo-metallurgical simulation of TIG welding obtained for the input data listed in *Table 7.1* are used to perform mechanical analyses to study the influence of welding current variation on the resulting stress distribution. The final HAZ and the compressive stress maps in the X-X direction for various current values are shown in *Fig. 7.3.11*. Stresses are evaluated at the end of welding. It should be noted that the increase in temperature causes an increase of stress.

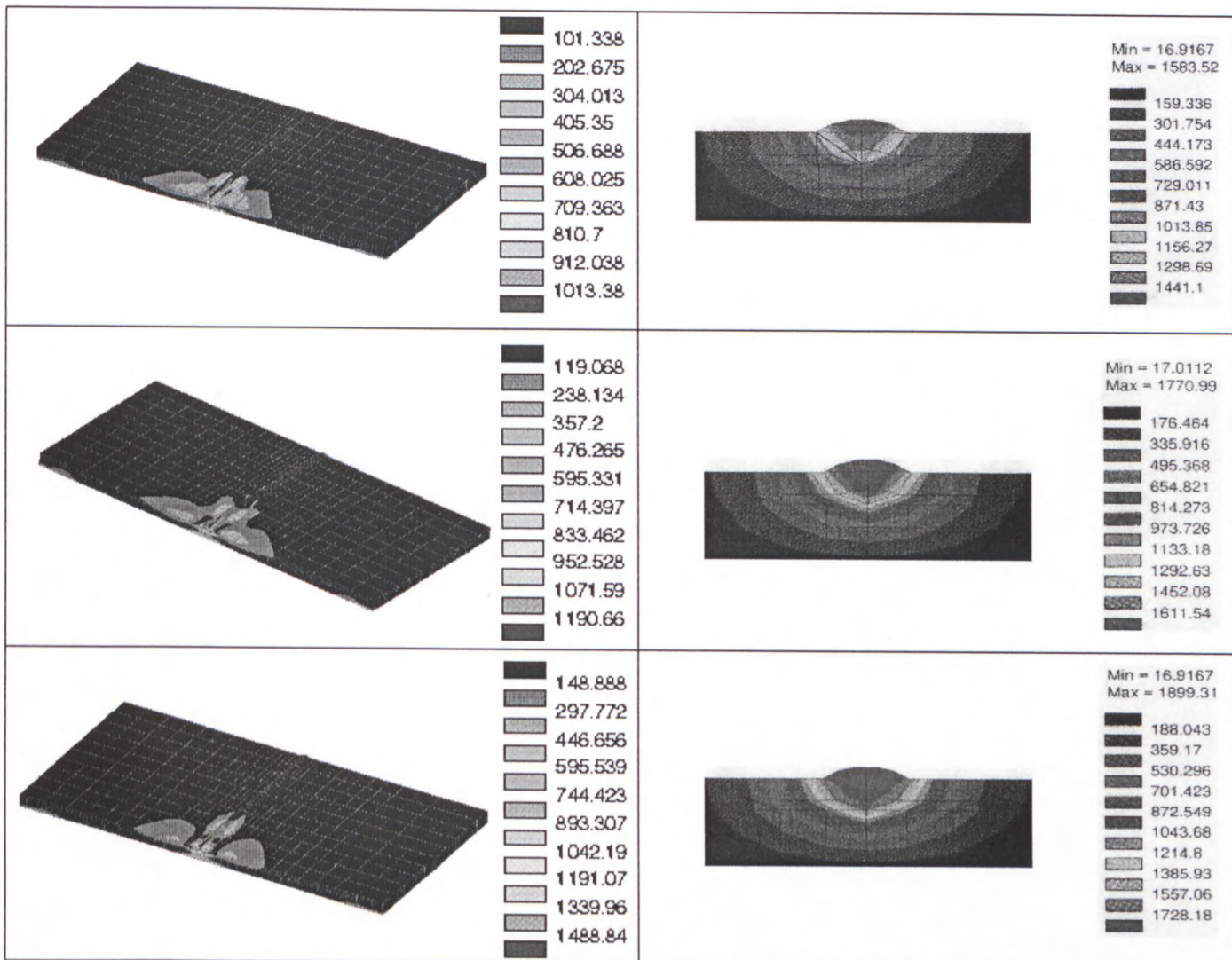


Figure 7.3.11 Influence of welding current on stress



The following function is obtained from the graph in **Fig. 7.3.11**

$$\text{Absolute compressive stress} = \frac{1}{(g + h^I)}, \quad (7.2.6)$$

where  $g$  and  $h$  are parameters and  $I$  is the welding current. The correlation between the maximum value of compressive stress and welding current is given in **Table 7.6**.

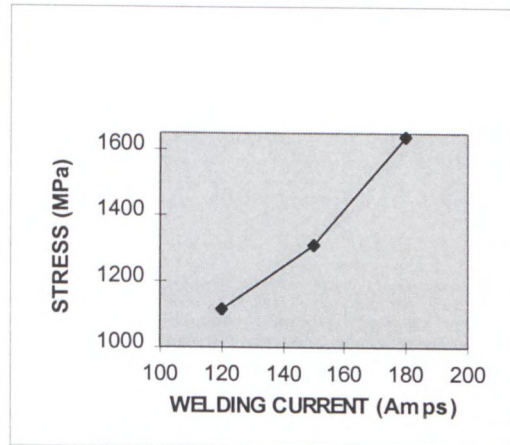


**Figure 7.3.12** Maximum values of compressive stresses from Fig. 7.3.13 versus welding current

WELDING CURRENT (Amps)	ABSOLUTE STRESS (MPa)
102	1013.93
109	1049.5
116	1087.65
123	1128.68
130	1172.93
137	1220.79
144	1272.72
151	1329.26
158	1391.06
165	1458.9

**Table 7.6** Correlation of welding current versus absolute stress values

### 7.3.5 Influence of welding speed on residual stress

Temperature and phase fractions obtained for welding operational data listed in **Table 7.4** are used in sensitivity analysis of residual stress component  $S_{11}$  subject variations of welding speeds. The results of these analyses are shown in **Fig. 7.3.11** from where it can be noted that the increase of the welding speed reduces the amount of residual stresses. This supported by the observation that an increase of the welding speed reduces temperature in HAZ. However, it should be noted that an increase of the welding speed reduces also the penetration of welding arc.

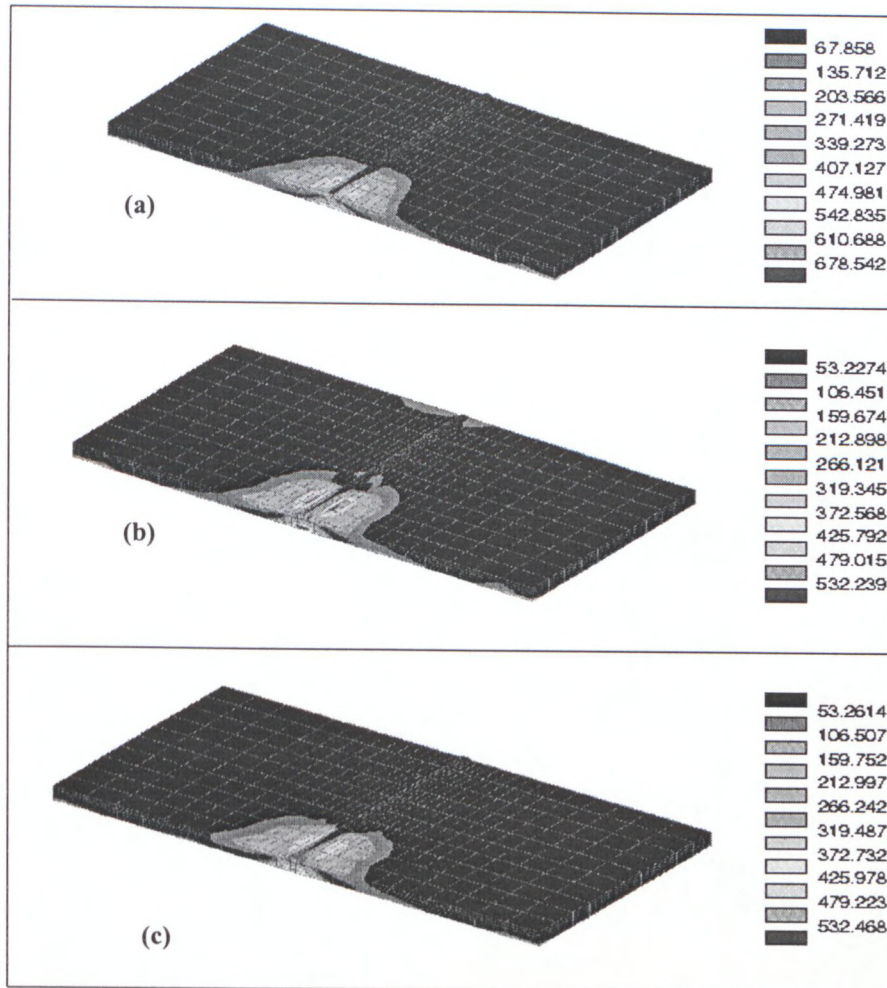
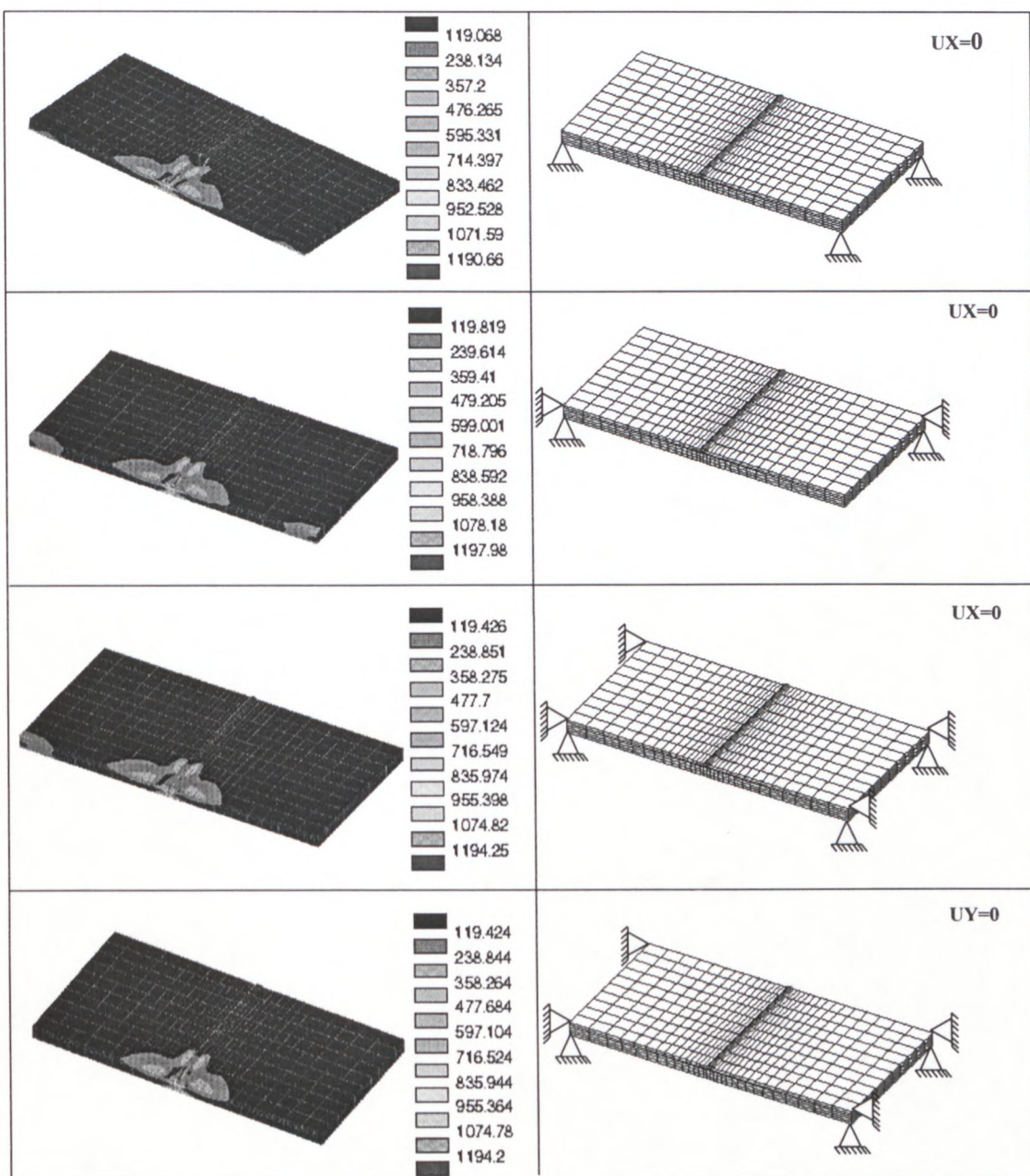


Figure 7.3.13 Stress contours for various welding speeds (a) 2.5mm/s, (b) 5mm/s, (c) 7.5mm/s.



### 7.3.6 Influence of clamping on residual stresses

An influence of clamping schemes on residual stress formation is considered in this section. From **Fig. 7.3.14** it can be noted that the pattern of stress contours is not significantly influenced by a clamping scheme but maxima of stresses are different and their location varies from scheme to scheme.



**Figure 7.3.14** Stress contours for various clamping schemes



## CHAPTER 8

### EXPERIMENTAL VERIFICATION OF NUMERICAL RESULTS

---

#### 8.1 Introduction

The main purpose of welding experiments is the verification of numerical results obtained by utilization of the thermo-mechano-metallurgical theory of welding implemented in SYSTUS/SYSWELD 2. Various welding experiments were performed and compared with the numerical results. However, results for two of these experiments are shown: one for the verification of arc penetration, and the other for verification of residual stresses. Both of them validates a software for setting up a control system for TIG welding of the **Material 2**.

#### 8.2 Welding experiments

Welding experiments have been performed at the *Welding Research Laboratory* at Peninsula Technikon. This laboratory is equipped with the state of the art welding equipment. A test rig built for welding and cutting experiments can be seen in **Fig. 8.1**. The rig consists of the *BDH400* combination of three welding machines: *Mig/Mag, TIG*, and *MMA* and a straight line moving TIG torch holder. *BDH400* machine is fully automated and can be used in a manual or automatic capacity. The TIG torch holder was built to ensure that a constant welding or cutting speed is maintained during experiments.

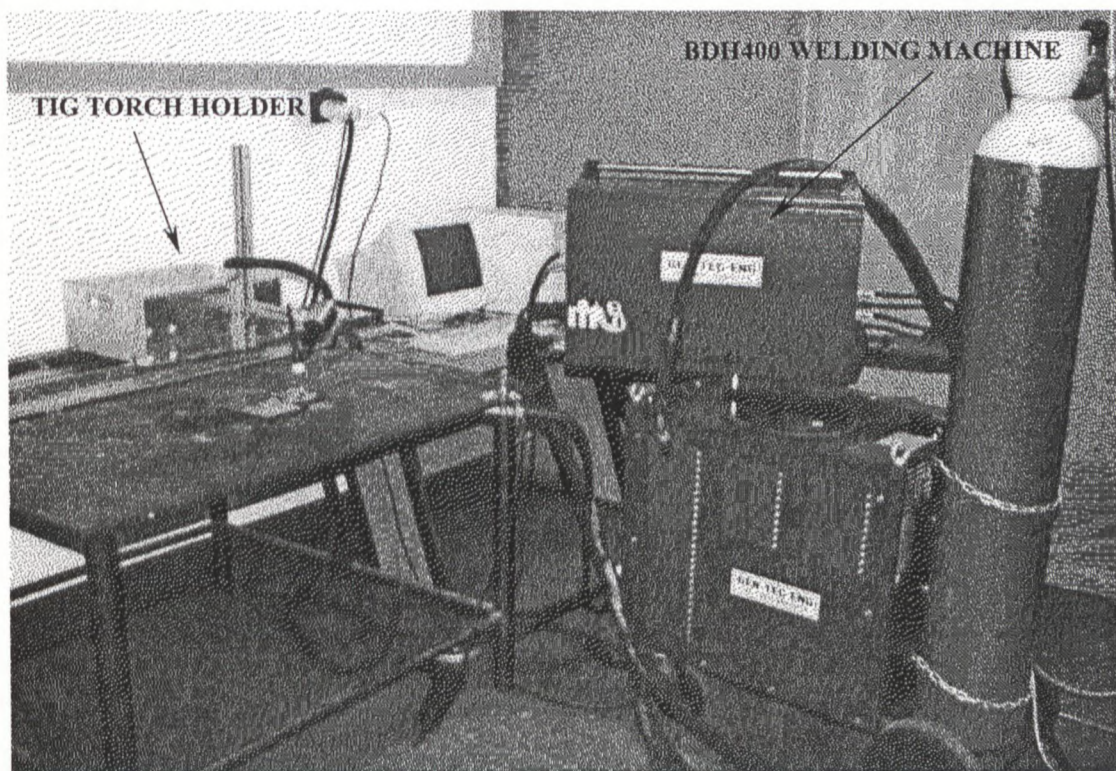


Figure 8.1 Test rig used for welding experiments



### 8.2.1 Experiments for welding penetration

Two welding experiments were performed to verify the depth  $h$  and width  $b$  of penetration in *Tables 7.2, 7.3 (a) and (b), and 7.5* obtained for various welding speeds and currents.

The steel used for our experiments is marked by ROQ-TUF-690, which is the South African equivalent of the **Material 2**. This steel is used for pipelines and offshore structures. It is very stiff material and is often difficult to weld. A 2.5mm mild steel rod was used as a filler metal for welding of two plates of dimensions: 100 x 100 x 8mm. Plates, before welding, have been grinded to ensure that surfaces and adjacent areas to the welding line are clean and smooth. The tungsten tip of the TIG torch is adjusted to the height of 9mm from the base plates and the filler metal is fed manually during welding. Argon is used as the shielding gas. The welding parameters for both experiments are listed in *Table 8.1*.

**Figs. 8.2 (a) and (b)** show the TIG torch as it moves along the welding line.

<i>WELDING CURRENT</i>	<i>WELDING VOLTAGE</i>	<i>WELDING SPEED</i>
150 Amperes	12.9≈13.1 Volts	2.4mm/s

**Table 8.1** Welding operational parameters used in welding experiments

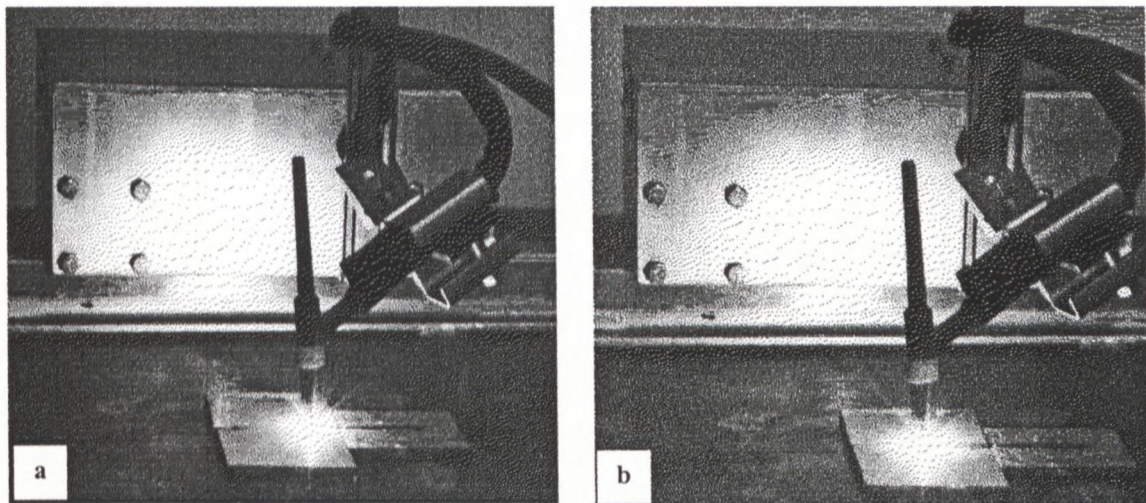


**Fig. 8.2** The TIG torch moving along the welding line. (a) TIG torch somewhat at the beginning of welding (b) TIG torch in the middle of welding.

The final HAZ and penetrations of the arc evaluated in experiments are shown in **Fig. 8.3 (a) and (b)**. Values of the depth  $h$  and width  $b$  of penetration evaluated by SYSWELD 2 and measured after real welding experiments are given in *Table 8.2*.

EXPERIMENT 1		EXPERIMENT 2		NUMERICAL RESULT (TABLE 7.2)	
width ( $b$ )	depth ( $h$ )	width ( $b$ )	depth ( $h$ )	width ( $b$ )	depth ( $h$ )
5.89mm	2.15mm	5.45mm	2.2mm	4.8662mm	2.0583mm

**Table 8.2** Comparison of experimental and numerical results



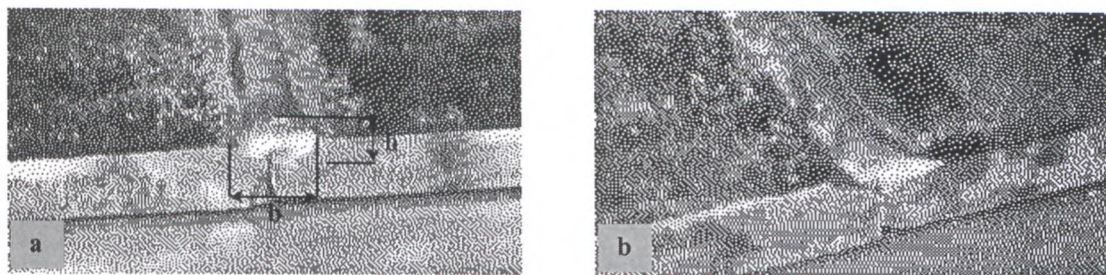


Figure 8.3 Penetration and HAZ for (a) experiment 1 and (b) experiment 2

The experimental and the numerical results compare well, although there is some difference in the width of penetration. The percentage error for the width of penetration is between 10 to 17%, while the percentage error for the depth of penetration is only 4.4 to 6.4%. In addition, for a welding speed 2.4mm/s, the width and depth of penetration is 5.7mm and 3.14mm and can be compared with results in *Tables 7.3 (a), (b) and 7.5*. These results show that the numerical results in *Table 7.2, 7.3 (a) and (b) and 7.5* can be used to set up a control or optimization system for TIG welding for **Material 2**. This system can be used to predict depth  $h$  and width  $b$  of penetration for any welding current and welding speed performed on 8mm plates made of **Material 2**.

### 8.2.1 Measurement of residual stresses.

A stress measurement has been performed to verify experimentally residual stress evaluated by SYSWELD 2 in a welded plate made of the Material 2. The results of this test are compared with data for **run 2** in *Table 7.1*. The welding operating parameters for this experiment correspond to *Table 8.1*. After welding, a rectangular ( $45^\circ$ ) rosette of strain gauges has been pasted on the surface of a plate close to the welding line. This is illustrated in Fig 8.4. Initial stress readings were obtained by connecting the strain gauge to a TQ Electronics Digital Strain Bridge.

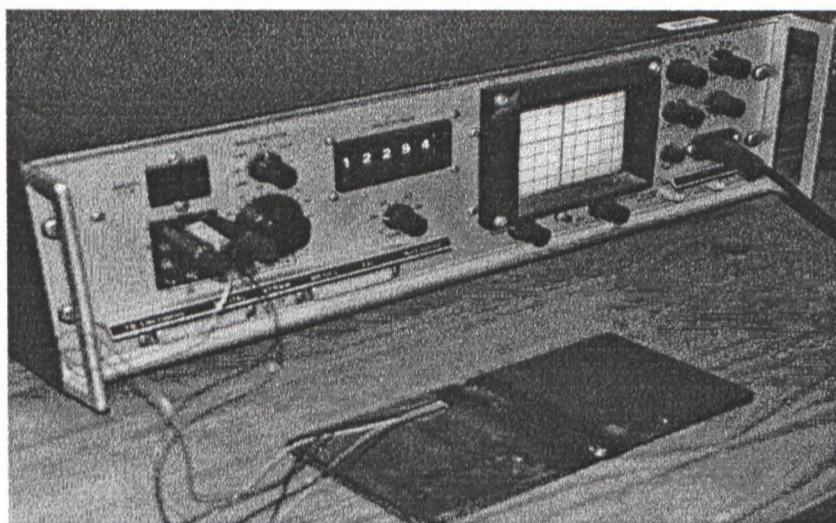


Figure 8.4 Photo showing the position of the strain gauge on the plate as well as the strain-measuring device

The strain is relieved by drilling a hole of 1mm-diameter and a depth of 1mm at point **G** shown in **Fig. 8.5**. The strain readings for 1mm depth were done by connecting



strain gauges to the strain-measuring device. The latter strain values, have been subtracted from the initial strain values. The resulting values are used in equations for the rectangular rosette to calculate the principal stresses, strains and angles. The Mohr's stress circle is employed to measure normal stresses in depth of 1mm.

The stress measured in point **G** of **Fig.8.5** is about 50MPa and the corresponding value extracted from **Fig. 8.6** is 56.53 MPa.

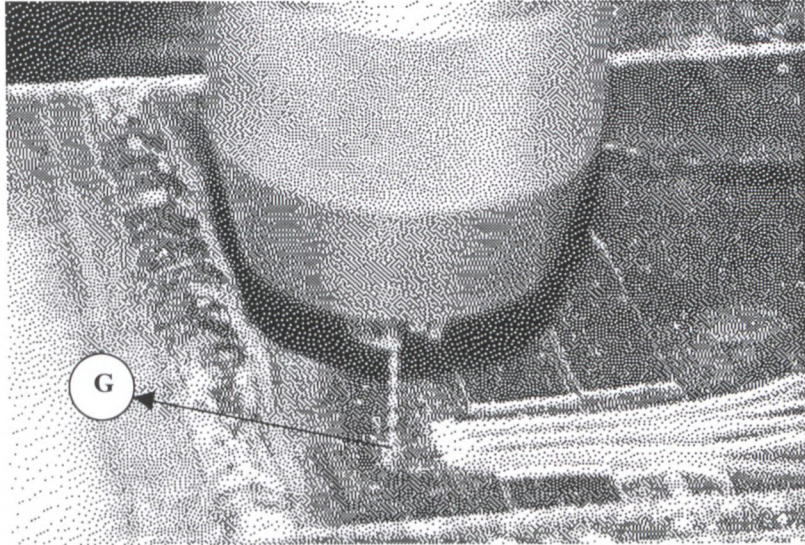


**Figure 8.5** Photo showing the Hole Drilling Technique.

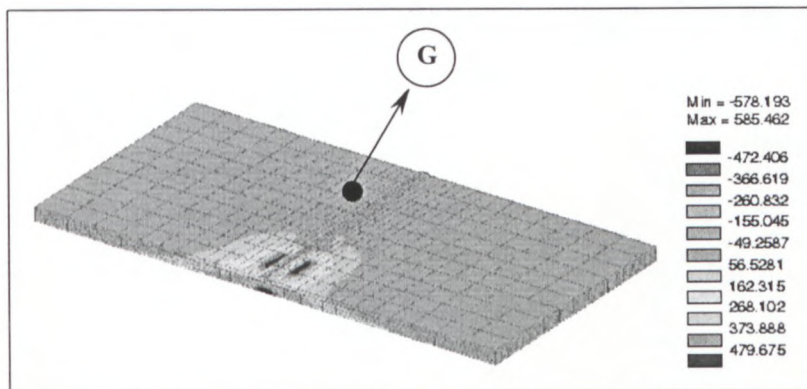


**Fig.8.6** Residual stress component  $S_{xx}$  evaluated for TIG welding for data run 2 in *Table 7.1*

Strain readings from the measuring device as well as calculations performed for this welding experiment can be found in **APPENDIX C**.

The measured stress and stress evaluated from SYSWELD 2 are in good agreement.



## CHAPTER 9

### CONCLUSIONS

---

The aim of this thesis is to conduct parametric sensitivity analysis for TIG welding. The objectives of this optimization are to determine the electric arc penetration and residual stresses in a weldment. Welding operating parameters: current, voltage, and speed of arc are variables in this analysis.

TIG welding is modeled as the thermo-mechano-metallurgical (TMM) problem with solid phase transformations and transformation induced plasticity. Boundary conditions reflect thermal interactions between weld-joint and environment: conduction, convection and radiation, as well as clamping schemes possible for welded plates.

The welding benchmark is formulated for square butt welding of two square plates of dimensions 100mm x 100mm x 8mm (or 13mm, or 20mm). The electric arc is modeled by the moving heat source of the bell-shape surface.

The TMM problem has been solved by finite element method using SYSTUS/SYSWELD 2 program. The data-input deck is listed in APPENDIX A where one of data is the CCT diagram. Data for two steels called here Material 1 and Material 2 are utilized. The width and depth of arc penetration, shape and size of HAZ, temperature field, material microstructure determined by solid phase fractions, residual stresses and deformation for three values of welding current and three values of speed have been evaluated by SYSWELD 2.

The following functions are roughly identified on the basis of results of FEM simulations:

- current versus width of arc penetration,
- current versus depth of arc penetration,
- temperature versus width of arc penetration,
- temperature versus depth of arc penetration,
- welding speed versus temperature,
- welding current versus stress.

These functions can be used for evaluation of the arc penetration, temperature, and stress for other values of welding operating parameters i.e. variables of identified functions. These results are shown in *Tables 7.2, 7.3 (a),(b), 7.5, and 7.6*. The identified functions can be used in development of TIG on-line system that can control residual stresses in a weld-joint subject to variations of welding operating parameters.

Heat in- and out- fluxes are incorporated into the software package using FORTRAN codes.

Numerical results for residual stresses and the arc penetration have been verified by welding experiments performed at the *Welding and Cutting Laboratory* of the Peninsula Technikon in Belville with the use of modern welding unit BDH400.



The hole drilling technique has been utilized for measurement of residual stresses. The stress measurement and numerical evaluations are in good coincidence.

## CHAPTER 10

### NOTES

---

For two thirds of the time that the study was in progress, an IBM RISC 6000 computer was used for the collection of the simulated results. Due to the size of the analyses, it was a very time consuming task. A thermal analysis could take up to one and half days, while a mechanical analysis could take up to seven or eight months. These analyses required constant monitoring. This however changed with acquisition of the latest Hewlett Packard workstation, which had a 30 times faster processing time than that of the IBM machine. The results could be gathered faster and in greater quantities. This increased the standard of the results as well as the time spent on collecting the simulated data.

In future, this type of analyses will be made even easier to acquire, with the introduction of better software for TMM simulation and faster computers. These parametric sensitivity analyses could be of great importance to the welding industry.



## APPENDICES

## APPENDIX A

## Input files used in SYSWELD

## A.1 Thermo-metallurgical input file

```

SEARCH DATA 60
MODE BATCH
DEFINITION
  Simulation of Tig welding process
OPTION THERMAL METALLURGY SPATIAL
RESTART GEOMETRY
MATERIAL PROPERTIES
;bead
  e 651 to 730 / KX=KY=KZ=-1,C=-2,RHO=7.8*-6 material 1
;two plates
  e 731 to 2230 / KX=KY=KZ=-1,C=-2,RHO=7.8*-6 material 1
CONSTRAINTS
; CONVECTION FROM THE TOP SURFACE
  E 1 to 50 201 to 350 501 to 650 / KT 1.*-3
LOADS
1 120 AMPS-8mm plate
; ROOM TEMPERATURE
  E 1 TO 50 201 to 350 501 to 650 / TT 22
; RADIATION BOUNDARY CONDITION
  E 1 TO 50 201 to 350 501 to 650 / QR 300 VARI -4
; CONTACT THERMAL CONDUCTANCE
  E 51 TO 200 351 to 500 / QR 100 VARI -5
; HEAT FLUX AS A BOUNDARY CONDITION
  E 651 to 730 / QR 1 VARI -6
TABLES
  1 /1 0 0.0527 200 0.0508 400 0.0434 600 0.0353 601
    0.0353 730 0.0315 800 0.0295 801 0.0295 1000 0.0290
    1470 0.033 1520 0.033 2400 0.3
  2 /1 0 456.4 200 485.1 400 516.28 600 579.48
    601 658.7 730 691.4 800 720.0 801 669.871800
    1000 669.871800 1470 600.384600 1520 600.384600 2400 600.384600
4 / FORTRAN
  FUNCTION F(W)
  DIMENSION W(5)
C *** RADIATION LOSSES ***
C
  T=(5)
  N=10**14

```

```

S=5.6696
S=S/N
E=0.9
ST=234256
H=T**4
H=H-ST
H=H*E
FR=H*S
F=-FR
RETURN
END

```

5 / FORTRAN

```

FUNCTION F(W)
DIMENSION W(5)

```

C \*\*\* THERMAL CONTACT CONDUCTANCE \*\*\*  
C

```

TH=W(5)
CC=0.026
F1=TH-17
F=CC*F1
F=-F
RETURN
END

```

6 / FORTRAN

```

FUNCTION F(W)
DIMENSION W(5)

```

C \*\*\* MODEL OF THE ARC \*\*\*  
C

```

S=W(4)
X=W(1)
X=X-0
Z=W(3)
Z=Z-9.035533906
Y=W(2)
vt=5.0
rm=2.5
yy=vt*s
YY=y+yy
p1=9.1880572050
p2=-0.007041909
p3=x*x
p4=yy*yy
p5=z*z

```

C \*\*\* px=r \*\*\*

```

px=p3+p4
px=px+p5

```

C \*\*\* p3=r<sup>2</sup> \*\*\*

```

p3=sqrt(px)

```

C \*\*\* p4=distribution radius \*\*\*

```

p4=p3-rm

```

C \*\*\* px=distribution radius squared \*\*\*



```

    px=p4**2
C *** px=negative px times parameter
    px=p2*px
C *** p3=exponential decay function ***
    p3=exp(px)
C *** q=power times the exponential decay away from the weld
centre ***
    q=p1*p3
C *** f=heat flux ***
    F=q
    continue
    RETURN
    END
RETURN
RENUMBER ITERATION 1
RETURN
MODE INTERACTIVE
TRANSIENT NON-LINEAR JOURNAL
BEHAVIOUR METALLURGY 3 FILE metal.dat
ALGORITHM BFGS ITERATION=800
PRECISION ABSOLUTE DISPLACEMENT 0.001 FORCE 0.001
METHOD DIRECT NONSYMMETRIC
INITIAL CONDITIONS
  e/ P 0 0 1
  n / TT 22
TIME INITIAL 0.0
  0.5 STEP 1 /STORE 1
RETURN
SAVE DATA TRAN 204
END

```

## A.2 Fortran code for radiation flux

```

    FORTRAN
    FUNCTION F(W)
    DIMENSION W(5)
C *** RADIATION LOSSES ***
C
    T=(5)
    N=10**14
    S=5.6696
    S=S/N
    E=0.9
    ST=234256
    H=T**4
    H=H-ST
    H=H*E
    FR=H*S
    F=-FR
    RETURN
    END

```

### A.3 Fortran code for thermal contact conductance flux

```

FORTRAN
FUNCTION F(W)
DIMENSION W(5)
C *** THERMAL CONTACT CONDUCTANCE ***
C
TH=W(5)
CC=0.026
F1=TH-17
F=CC*F1
F=-F
RETURN
END

```

### A.4 Fortran code for the model of the Tig welding arc

```

FORTRAN
FUNCTION F(W)
DIMENSION W(5)
C *** MODEL OF THE ARC ***
C
S=W(4)
X=W(1)
X=X-0
Z=W(3)
Z=Z-9.035533906
Y=W(2)
vt=5.0
rm=2.5
yy=vt*s
YY=y+yy
p1=9.1880572050
p2=-0.007041909
p3=x*x
p4=yy*yy
p5=z*z
C *** px=r ***
px=p3+p4
px=px+p5
C *** p3=r^2 ***
p3=sqrt(px)
C *** p4=distribution radius ***
p4=p3-rm
C *** px=distribution radius squared ***
px=p4**2

```



```

C *** px=negative px times parameter
      px=p2*px
C *** p3=exponential decay function ***
      p3=exp(px)
C *** q=power times the exponential decay away from the weld
centre ***
      q=p1*p3
C *** f=heat flux ***
      F=q
      continue
      RETURN
      END

```

### A.5 Metallurgy input file used in SYSWELD (Material 1)

```

MATERIAL 1 PHASE 4
REACTION
1 4          K TABLE 1  KP TABLE 2  F TABLE 3  FP TABLE 3
4 2          COOLING K TABLE 4  KP TABLE 5
4 3          COOLING K TABLE 6  KP TABLE 7  F TABLE 8  FP TABLE 8
TABLE
1/1 725 0 840 1.333 910 3.333 960 10 1000 20
2/1 710 0 725 0.833 840 0
3/1 -5 1 0 0 5 1
4/1 520 0 530 10 540 9.75 550 9.61 560 9.44 570 9.02
• 580 8.67 590 8.14 600 7.59 610 7.02 620 6.25 630 5.36
• 640 4.65 650 3.89 660 2.38 670 1.89 680 1.23 690 0.77
• 700 0.4 710 0
5/1 530 0 540 0.25 550 0.39 560 0.56 570 0.98
• 580 1.33 590 1.86 600 2.41 610 2.98 620 3.75 630 4.64
• 640 5.35 650 6.11 660 7.17 670 8.11 680 8.77 690 9.23
• 700 9.6 710 10 720 0
6/1 400 0.011 401 0
7/1 400 0.0
8/1 -10000 10000 10000 -10000
END

```

### A.6 Metallurgy input file used in SYSWELD (Material 2)

```

MATERIAL 1 PHASE 3
REACTION
3 1 cooling K table 10 KP table 11 F table 12 FP table 12
3 2 cooling MS 400 KM 0.011
TABLE
10/1 399 0 400 1 523 0
11/1 399 0 400 0 523 1 524 0
12/1 (-1000 0.05) (-100 .05) (-13.51 .04) (-11.3 .04) (-1.9 .035)
(-1.3 .03)
* (-0.15 .025) (-.01 .025)
END

```

## APPENDIX B

### Thermal and mechanical material properties for Material 1 & 2

#### B.1 Thermal properties for Material 1

TEMPERATURE ( $^{\circ}\text{C}$ )	0	50	700	900	1100	1300	1500	1800
CONDUCTIVITY ( $\text{J}/\text{mm}\cdot\text{s}\cdot^{\circ}\text{C}$ )	0.046	0.046	0.033	0.029	0.029	0.035	0.055	0.100

TEMPERATURE ( $^{\circ}\text{C}$ )	0	400	600	1500
SPECIFIC HEAT ( $\text{J}/\text{Kg}\cdot^{\circ}\text{C}$ )	470	600	700	700

TEMPERATURE ( $^{\circ}\text{C}$ )	0	700	900	1500
DENSITY ( $\text{Kg}/\text{mm}^3$ )	7.8E-6	7.6E-6	7.6E-6	7.3E-6

#### Metallurgical properties of Material 1

Four metallurgical phases are considered for Material 1:

- ⇒ Initial material ,
- ⇒ Bainite,
- ⇒ Martensite,
- ⇒ Austenite.

The initial phase of the material will be Austinite.

#### B.2 Mechanical properties for Material 1

Poisson's ratio = 0.3

TEMPERATURE ( $^{\circ}\text{C}$ )	Young's Modulus (MPa)	TEMPERATURE ( $^{\circ}\text{C}$ )	Young's Modulus (MPa)
20	207000	900	39000
200	200000	1000	25000
300	192000	1100	16500
400	180000	1200	10500
500	163000	1300	6250
600	132000	1400	2000



650	105000	1450	1500
700	82000	1500	500
800	53000		

Thermal strain for initial material, bainite and martensite

TEMPERATURE ( $^{\circ}\text{C}$ )	Thermal Strain ( $10^{-5}$ )	TEMPERATURE ( $^{\circ}\text{C}$ )	Thermal Strain ( $10^{-5}$ )
0	-22.96	400	531.84
50	34.44	450	611.99
100	95.94	500	693.54
150	161.54	550	776.19
200	230.64	600	860
250	303.04	650	963.74
300	377.84	1250	2094.2
350	454.09	1450	2471.02

Thermal strain for Austenite

TEMPERATURE ( $^{\circ}\text{C}$ )	Thermal Strain ( $10^{-5}$ )	TEMPERATUR E ( $^{\circ}\text{C}$ )	Thermal Strain ( $10^{-5}$ )
0	-630	700	680
50	-560	750	788
100	-480	800	890
150	-392	850	992
200	-300	900	1099.34
250	-210	950	1221.54
300	-118	1000	1344.04
350	-25	1050	1465.94
400	72	1100	1588.54
450	172	1150	1711.24
500	272	1200	1833.4
550	375	1250	1950
600	472	1450	2416
650	578		

Yield stresses for the plate material

Initial material

TEMPERATURE ( $^{\circ}\text{C}$ )	YIELD STRESS (MPa)
20	425
200	419
300	410

400	380
500	330
600	240
700	110
800	80
900	62.5
1000	45
1100	33
1200	21
1300	12.5

## Bainite

TEMPERATURE (°C)	YIELD STRESS (MPa)
20	445
200	435
300	420
400	390
500	342
600	250
650	182
700	118
800	80
900	62.5
1000	45
1100	33
1200	21
1300	12.5

## Martensite

TEMPERATURE (°C)	YIELD STRESS (MPa)
20	750
200	655
300	625
400	595
500	533
600	417
650	315
700	210
750	140
800	90
900	62.5
1000	45



1100	33
1200	21
1300	12.5

## Austenite

TEMPERATURE (°C)	YIELD STRESS (MPa)
200	220
300	200
400	180
500	147.5
600	120
700	98
800	75
900	62.5
1000	45
1100	33
1200	21
1300	12.5
1400	4
1450	1.5
1500	1

Strain Hardening for  $\alpha$ -phases of the initial material, bainite and martensite

T=20°C		T=200°C	
$\epsilon_p$	H( $\epsilon_p$ )	$\epsilon_p$	H( $\epsilon_p$ )
0	0	0	0
0.01	5	0.01	2
0.02	20	0.02	49
0.03	71	0.03	91
0.04	99	0.04	121
0.05	127	0.05	153
0.07	177	0.07	195
0.1	228	0.1	239
0.15	281	0.15	287
1	1182	1	1103

T=500°C		T=600°C		T=700°C	
$\epsilon_p$	H( $\epsilon_p$ )	$\epsilon_p$	H( $\epsilon_p$ )	$\epsilon_p$	H( $\epsilon_p$ )
0	0	0	0	0	0
0.01	33	0.01	12	0.01	6
0.02	85	0.02	26	0.02	13
0.03	107	0.03	38	0.03	19
0.04	125	0.04	48	0.04	24
0.05	140	0.05	56	0.05	28

T=500°C		T=600°C		T=700°C	
$\epsilon_p$	H( $\epsilon_p$ )	$\epsilon_p$	H( $\epsilon_p$ )	$\epsilon_p$	H( $\epsilon_p$ )
0.07	161	0.07	70	0.07	35
0.1	183	0.1	82	0.1	41
0.15	195	0.15	86	0.15	43
1	399	1	166	1	83

Strain Hardening for  $\gamma$ -phases of austenite

T=200°C		T=500°C		T=600°C		T=700°C		T=800°C		T=900°C		T=1000°C	
$\epsilon_p$	H( $\epsilon_p$ )	$\epsilon_p$	H( $\epsilon_p$ )	$\epsilon_p$	H( $\epsilon_p$ )	$\epsilon_p$	H( $\epsilon_p$ )	$\epsilon_p$	H( $\epsilon_p$ )	$\epsilon_p$	H( $\epsilon_p$ )	$\epsilon_p$	H( $\epsilon_p$ )
0	0	0	0	0	0	0	0	0	0	0	0	0	0
0.05	145	0.05	145	0.05	140	0.05	120	0.05	95	0.05	55	0.05	20
1	2900	1	2900	1	2800	1	2400	1	1900	1	1100	1	400

T=1100°C		T=1250°C	
$\epsilon_p$	H( $\epsilon_p$ )	$\epsilon_p$	H( $\epsilon_p$ )
0	0	0	0
0.05	5	0.05	2.5
1	100	1	50

**B.3 Thermal properties for Material 2**Density = 7.86E-6 kg/mm<sup>3</sup>

TEMP (°C)	0	200	400	600	601	730
SPECIFIC HEAT *10 <sup>-3</sup> (kJ/m <sup>3</sup> K)	3.56	3.78	4.02	4.52	5.13	5.39
TEMP (°C)	800	801	1000	1470	1520	2400
SPECIFIC HEAT *10 <sup>-3</sup> (kJ/m <sup>3</sup> K)	5.61	5.22	5.14	4.68	4.68	4.68

TEMP (°C)	0	200	400	600	601	730
CONDUCTIVITY *10 <sup>-2</sup> (W/mK)	5.27	5.08	4.34	3.53	3.53	3.15
TEMP (°C)	800	801	1000	1470	1520	2400
CONDUCTIVITY *10 <sup>-2</sup> (W/mK)	2.95	2.95	2.90	3.3	3.3	3.0



### Metallurgical properties of **Material 2**

Four metallurgical phases are considered for **Material 2**:

⇒ Austenite ,

⇒ Bainite,

⇒ Martensite,

The initial phase of the material will be Austenite.

TEMP (°C)	0	100	200	300	400	500	600
THERMAL EXPANSION (W/mK)	11.7	12.5	13.0	13.6	14.1	14.5	14.9
TEMP (°C)	700	800	900	1000	1200	1450	
THERMAL EXPANSION (W/mK)	15.06	12.76	13.14	13.5	14.21	15.18	

### B.4 Mechanical properties for **Material 2**

TEMP (°C)	0	100	200	300	400	500
POISSON'S RATIO	0.283	0.287	0.29	0.294	0.298	0.305
TEMP (°C)	600	700	800	950	1100	1450
POISSON'S RATIO	0.314	0.324	0.334	0.349	0.48	0.48

TEMP (°C)	0	100	200	300	400	500	600
YOUNG'S MODULUS (N/mm <sup>2</sup> )	213	207	199	192	184	175	164
TEMP (°C)	700	800	900	1000	1200	1450	
YOUNG'S MODULUS (N/mm <sup>2</sup> )	139	113	88	63.3	20	20	





## APPENDIX C

### Equations used in stress-strain experimental measurements

Principal strains

$$\varepsilon_{p,q} = \frac{\varepsilon_1 + \varepsilon_3}{2} \pm \frac{1}{\sqrt{2}} \sqrt{(\varepsilon_1 + \varepsilon_2)^2 + (\varepsilon_2 + \varepsilon_3)^2}$$

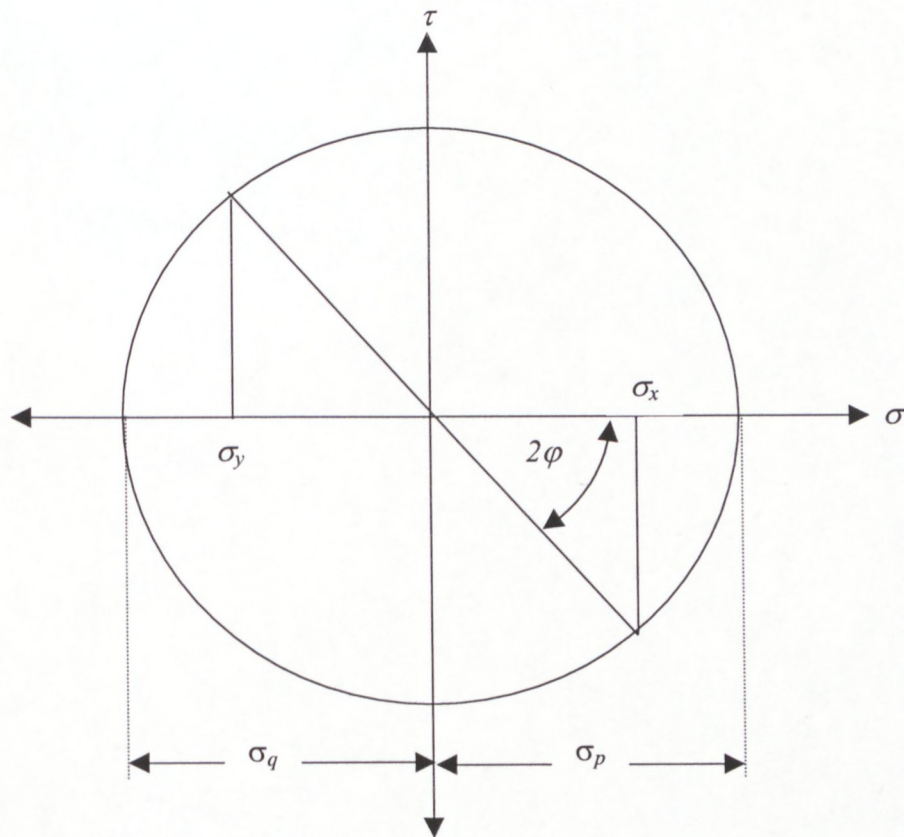
Principal stresses

$$\sigma_{p,q} = \frac{E}{2} \left( \frac{\varepsilon_1 + \varepsilon_3}{1 - \nu} \pm \frac{\sqrt{2}}{1 + \nu} \sqrt{(\varepsilon_1 + \varepsilon_2)^2 + (\varepsilon_2 + \varepsilon_3)^2} \right)$$

Principal angles

$$\varphi_{p,q} = \frac{1}{2} \tan^{-1} \left( \frac{(\varepsilon_2 - \varepsilon_3) - (\varepsilon_2 - \varepsilon_1)}{(\varepsilon_1 - \varepsilon_3)} \right)$$

Mohr's stress circle



***First Measurement***

Gauge 1. 12258E-6  
Gauge 2. 17296E-6  
Gauge 3. 13769E-6

***Second Measurement***

Gauge 1. 12239E-6  
Gauge 2. 13178E-6  
Gauge 3. 13767E-6



**BIBLIOGRAPHY**

- 
- [1] Anderson, B.A.B., Thermal stresses in a submerged-arc welded joint considering phase transformations, *J. Eng. and Tech., Trans. ASME*, Vol. 100, pp 356-362, 1978.
  - [2] Bathe, *Finite Element Procedures*, Prentice Hall, Englewood Cliffs, New Jersey 07632, (1996).
  - [3] Bergheau, J. M., Leblond, J. B., Coupling between heat flow, metallurgy and stress-strain computations in steels. The approach developed in the computer code SYSWELD for welding and quenching. Vth Engineering Foundation Conference on Modeling of Casting, Welding and Advanced Solidification Processes. 17 - 21 September 1990 - DAVOS (Suisse). FRAMASOFT+CSI, SYSWELD, User's Manual
  - [4] Denis, S., Gautier, E. Simon, A., Modelling of the mathematical behaviour of steels during phase transformations, in Beck, G. et al (eds), *Proc. ICRS 2*, Elsevier Applied Science, London, New York, pp 393-398, 1989.
  - [5] Easterling, K., *Introduction to Physical Metallurgy of Welding*, Butterworths, Monographs in Materials.
  - [6] Estrin, Y., A versatile unified constitutive model based on dislocation density evolution, in Freed, A.D. and Walker, K.P., (eds), *High Temperature Constitutive Modelling, The theory and application*, ASME, pp 65, 1991.
  - [7] Freidman, E., Analysis of weld puddle distortion, *Welding Journal Research Suppl.*, pp 161-166, 1978.
  - [8] Goldak, J.A., Chakravarti, A. and Bibby, M.J., A new finite element model for welding heat sources, *Trans. AIME.*, Vol. 15B, pp 299-305, 1984.
  - [9] Greenwood, G.W., and Johnson, R.H., The deformation of metals under small stresses during phase transformation, *Proc. Roy. Soc. A* 238, pp 403-422, 1965.
  - [10] Habraken, A.M. and Bourdouxhe, M., Coupled thermo-mechanical-metallurgical analysis during the cooling process of steel pieces, *Eur. J. Mech., A/Solids*, 11, no. 3, pp 381-402, 1992.
  - [11] Hearn, E. J., *Mechanics of Materials 1, An introduction to the Mechanics of elastic and plastic deformation of solids and structural materials.*, Third Edition, Butterworth Heinemann, pp 370-382., 1997.

- [12] Hibbit, H.D., Marcal, P.V., Goldak, J.A. and Watt, D.F., Coupling transient heat transfer-microstructure weld computations, *Acta Metal.*, Vol. 36, pp3037-3047, 1988.
- [13] Holman, J.P., *Heat Transfer*, S. I. Metric Addition, Mcgraw-Hill Book Company, 1986
- [14] Leblond, J.B., Mottet, G. and Devaux, J..C., A Theoretical and numerical approach to the plastic behaviour of steels during phase transformations of general relations-I derivations of general relations. *Journal of the Mechanics and Solids* Vol. 34, pp 395-409, 1986.
- [15] Leblond, J.B., Mottet, G. and Devaux, J..C., A Theoretical and numerical approach to the plastic behavior of steels during phase transformations II. Study for classical plasticity for ideal plastic phases. *J. Mech. Phys. Solids*, Vol. 34, no. 4, pp. 411-432, 1986.
- [16] Leblond, J.B., Devaux, J., Devaux, J.C., Mathematical modelling of transformation plasticity in steels I. : Case of ideal plastic phases. *Int. Journal. Of Plasticity*, Vol. 5, pp. 551-572, 1989.
- [17] Leblond, J.B., Mathematical modelling of transformation plasticity in steels II. : Coupling with strain hardening phenomena. *Int. Journal of plasticity*, Vol. 5, pp. 573-591, 1989.
- [18] Leung, C.K., Pick, R.J., Finite element analysis of multi-pass welds, *WRC Bulletin* 356, pp 11-33, 1990.
- [19] Magee, C. L., Transformation kinetics, Microplasticity and Aging of Martensite in Fe-31 Ni, PhD Thesis, Pittsburg (USA), 1966.
- [20] Masubuchi, K., *Analysis of welded structures*, Pergamon Press, New York, 1980.
- [21] *New Metals Handbook-The, Volume 6, Welding, Brazing, and Soldering*, American Society for Metals, Metals Park, Ohio 44073, 1983.
- [22] Okerblom, N.O., *The calculations of deformations of welded metal structures*, London, Her Majesty's Stationery Office, 1958.
- [23] Oliver, G.J., *Modelling of welding using various Constitutive Models of Steel*, Thesis submitted towards the Degree of MSc., Department of Applied Mathematics, U.C.T., 1994.



- [24] Philander, O., Oliver, G.J., Ronda, J., Mathematical Modeling of Welding: A study on the sensitivity of welding variables and their effects on residual stress, strain and deformation., 2nd South African Conference on Applied Mechanics, 13-15 January 1998, pp-781-790.
- [25] Philander, O., Oliver, G.J., Ronda, J., Mathematical Modeling of Welding: A study on the sensitivity of welding variables and their effects on residual stress, strain and deformation., 32<sup>nd</sup> Solid Mechanics Conference, Zakopane, September 1-5, 1998.
- [26] Philander, O. and Oliver, G.J., A study on the sensitivity of welding variables and their effects on the shape and size of heat affected zones., Research Probe, Peninsula Technikon, Volume 3., No 6, November 1997, pp 7-10.
- [27] Ronda, J., Mahrenholtz, O., Hamann, R., Thermomechanical simulation of underwater welding process., Arcive of Applied Mechanics, 62, pp 15-27, 1992.
- [28] Ronda, J. and Oliver, G.J., Comparison of applicability of various thermo-viscoplastic constitutive models in modeling of welding., Computer methods in applied mechanics and engineering. 153 (1998), pp 195-221.
- [29] Ronda, J. and Oliver, G.J., Consistant thermo-mechano-metallurgical model of welding, 1'st South African Conference on Applied Mechannics, 1996, pp 61-68.
- [30] Ronda, J. Estrin, Y. and Oliver, G.J., Modelling of Welding. A comparison of a thermo-mechano-metallurgical constitutive model with a thermo-viscoplastic material model., Journal of Materials Processing Technology 60, Elsevier, pp 629-636, 1996.
- [31] Ronda, J., Oliver, G.J., Meinert, N., Simulation of welding with phase transformation, Proc. Eighth Int. Conf. on Num. Meth. in Thermal Problems, in Lewis, R.W., (ed.), Pinnerigde Press, Swansea, pp 151-163, 1993.
- [32] Ronda, J. and Oliver, G.J., Work done in collaboration with Prof. O. Mahrenholtz.
- [33] Rosenthal, D., The Theory of moving sources of heat and its application to metal treatments, Trans. ASME, Vol. 68, pp. 849-865, 1946.
- [34] Rybicki, E.F., Stonisifer, R.B., Computation of residual stresses due to multi-pass welds in piping systems, Trans. ASME, J. Press. V. Tech., Vol. 101, pp 149-154, 1975.
- [35] Kou, S., Welding Metallurgy, A Wiley-Interscience Publication, John Wiley & Sons.

- [36] Ueda, Y. and Yamakawa, T., Analysis of thermal elastic-plastic stress and strain during welding by finite element method, Trans. Japan Welding Soc. Vol. 2, pp 90-100, 1971.
- [37] Vinokurov, V.A., Welding Stress and Distortion, The British Library Board, 1977.
- [38] SYSWELD, User's Manual, Framasoft + CSI.
- [39] SYSWELD, 3D welding simulation example, Framasoft + CSI.





CAPE PENINSULA  
UNIVERSITY OF TECHNOLOGY

